

Dissertation
submitted to the
Combined Faculties of the Natural Sciences and
Mathematics
of the Ruperto-Carola-University of Heidelberg, Germany
for the degree of
Doctor of Natural Sciences

Put forward by
Simon Murmann
Born in Lörrach
Oral examination: 25.11.2015

Few-particle quantum magnetism with ultracold atoms

Referees:

Prof. Dr. Selim Jochim

Prof. Dr. Markus Oberthaler

Abstract

This thesis reports on the deterministic preparation of magnetically ordered states in systems of few fermionic atoms. We follow the concept of quantum simulation and use ^6Li atoms in two different hyperfine states to mimic the behavior of electrons in a solid-state system. In a first experiment, we simulate the two-site Hubbard model by using two atoms in an isolated double-well potential. We prepare the two-particle ground state of this model with a fidelity exceeding 90%. By introducing strong repulsive interactions, we are able to realize a pure spin model and describe the energy spectrum with a two-site Heisenberg Hamiltonian. In a second experiment, we realize Heisenberg spin chains of up to four atoms in a single strongly-elongated trapping potential. Here, the atoms self-align along the potential axis due to strong repulsive interactions. We introduce two novel measurement techniques to identify the state of the spin chains and thereby confirm that we can deterministically prepare antiferromagnetic ground-state systems. This constitutes the first observation of quantum magnetism with fermionic atoms that exceeds nearest-neighbor correlations. Both the double-well system and the spin chains can be seen as building blocks of larger ground-state spin systems. Their deterministic preparation therefore opens up a new bottom-up approach to the experimental realization of quantum many-body systems with ultracold atoms.

Zusammenfassung

Diese Arbeit beschreibt die deterministische Präparation von magnetisch geordneten Zuständen in Systemen, die aus wenigen fermionischen Atomen bestehen. Aufbauend auf der Idee der Quantensimulation verwenden wir dabei ^6Li -Atome in zwei unterschiedlichen Hyperfeinzuständen, um das Verhalten von Elektronen in einem Festkörper zu imitieren. In einem ersten Experiment simulieren wir mit zwei Atomen in einem isolierten Doppelmuldenpotenzial das Hubbard-Modell mit zwei Gitterplätzen. Wir präparieren den Zweiteilchen-Grundzustand dieses Modelles mit einer Wahrscheinlichkeit von über 90%. Durch das Einführen starker repulsiver Wechselwirkungen ist es uns möglich ein reines Spinmodell zu realisieren, dessen Energiespektrum wir durch einen Heisenberg-Hamilton-Operator für zwei Teilchen beschreiben. In einem zweiten Experiment realisieren wir Heisenberg-Spinketten, die aus bis zu vier Atomen in einem stark gestreckten Fallenpotenzial bestehen. Aufgrund einer starken Abstoßung ordnen sich die Atome hierbei selbst entlang der Potenzialachse an. Wir führen zwei neue Messtechniken ein um den Zustand der Spinketten zu bestimmen und bestätigen, dass wir deterministisch antiferromagnetische Grundzustandssysteme präparieren können. Dies ist die erste Beobachtung von Quantenmagnetismus mit fermionischen Atomen, die Korrelationen zwischen nächsten Nachbarn überschreitet. Sowohl das Doppelmuldensystem als auch die Spinkette können als Bausteine für größere Grundzustandssysteme gesehen werden. Mit ihrer deterministischen Präparation eröffnen wir somit einen neuen Ansatz zur experimentellen Realisierung von Quanten-Vielteilchensystemen mit ultrakalten Atomen.

Contents

1. Introduction	1
2. Strongly interacting few-fermion systems in one dimension	7
2.1. Ultracold Fermi Gases	7
2.1.1. Two-component Fermi systems	9
2.2. Interactions in Fermi gases	11
2.2.1. Scattering in ultracold atomic gases	12
2.2.2. Scattering resonances	15
2.2.3. Feshbach resonances	16
2.2.4. Scattering in one-dimensional systems	17
2.3. Interacting 1D systems	20
2.3.1. Hamiltonian of two interacting atoms	21
2.3.2. Ground-state energy of two atoms in a harmonic trap	22
2.3.3. Ground-state energy of more than two atoms	26
2.4. Fermionization of ultracold atoms	28
2.4.1. Fermionization of identical bosons	29
2.4.2. Fermionization of spin-1/2 fermions	30
3. Quantum magnetism with ultracold atoms	33
3.1. Superexchange interactions	34
3.1.1. The two-site Hubbard model	34
3.1.2. Superexchange in the Hubbard model	36
3.2. The Heisenberg model	38
3.2.1. Emergence of spin models	38
3.2.2. The Heisenberg Hamiltonian	40
3.2.3. Antiferromagnetism	42
3.3. Assembling many-body spin systems	43
3.3.1. Combination of two spin singlets	44
3.3.2. Combining antiferromagnetic spin systems	45
3.4. Realization of Heisenberg spin chains	46
3.4.1. Realization of the Hubbard model	47
3.4.2. Heisenberg spin chains in the fermionization limit	49

4. Experimental setup	53
4.1. The experimental sequence	53
4.2. Experimental setup and initial cooling stages	55
4.2.1. The vacuum chamber	55
4.2.2. Zeeman slower	57
4.2.3. Magneto-optical trap (MOT)	57
4.2.4. Evaporative cooling in an optical dipole trap (ODT)	58
4.2.5. The Feshbach coils	60
4.3. Optical dipole traps for the realization of quantum magnetism	61
4.3.1. The microtrap: Realization of quasi-1D systems	61
4.3.2. Two microtraps: Realization of a double-well potential	64
4.4. Deterministic preparation of few-atom systems	68
4.4.1. Preparation scheme	69
4.4.2. Experimental realization of the deterministic preparation	69
4.4.3. Deterministic preparation of a spin-1/2 system	72
4.5. State detection in one and two wells	73
4.5.1. Atom-number counting	74
4.5.2. Additional state manipulation	75
5. Two fermions in a double well	77
5.1. The two-site Hubbard model	78
5.1.1. Hamiltonian of the two-site Hubbard model	79
5.1.2. Eigenstates of the two-site Hubbard model	79
5.1.3. Realization of the two-site Hubbard model	81
5.2. Calibration of the Hubbard parameters	82
5.2.1. Tunneling measurements	82
5.2.2. Calibration of the tunneling matrix element	83
5.2.3. Calibration of the potential tilt	84
5.2.4. Calibration of the on-site interaction energy	85
5.2.5. Validity of the Calibrations	86
5.3. Preparation of eigenstates in the double well	87
5.4. Occupation statistics in the double-well	88
5.4.1. Measurement of occupation statistics	89
5.4.2. Ground-state systems	90
5.4.3. Excited-state systems	91
5.4.4. Particle-hole symmetry	92
5.5. Second-order tunneling in the two-site Hubbard model	92
5.5.1. Second-order tunneling in a double well	93
5.5.2. Trap-modulation spectroscopy	95
5.5.3. Results of the trap-modulation spectroscopy	98

5.6. Singlet-triplet oscillations	98
5.6.1. Theory of singlet-triplet oscillations	98
5.6.2. Measurement of singlet-triplet oscillations	99
6. Heisenberg spin chains of few atoms	101
6.1. Spin chains of ultracold atoms in the fermionization regime	102
6.1.1. The spin-chain picture	102
6.1.2. Eigenstates and energies of three fermionized atoms	105
6.2. Preparation of antiferromagnetic Heisenberg spin chains	108
6.3. Probing the spin distribution	110
6.3.1. Tunneling measurements	110
6.3.2. Tunneling model	111
6.3.3. Comparison of measurement and theory	116
6.4. Probing the spatial wave function of the spin chains	117
6.5. Tunneling into ferromagnetic spin states	119
7. Conclusion and Outlook	123
A. Appendix	127
A.1. Basic definitions of a two-component spin model	127
A.1.1. Spin operators for single spins	127
A.1.2. Spin operators for multi-spin systems	128
A.2. Properties of ${}^6\text{Li}$	129
A.3. Calibration of the on-site interaction energy	131
A.4. The optical microtrap	132
A.5. Trap parameters	133
A.6. Correction of spin-down tunneling	134
A.7. Correction of occupation-number measurements	135
Bibliography	136

1. Introduction

The theory of magnetism is of fundamental importance in condensed-matter physics. It describes the interplay between magnetic fields and the magnetic moments of the microscopic particles in a solid state system. Within this theory, magnetic interactions change the energy of spatially separated particles dependent on the relative orientation of their magnetic moments. Even without an external magnetic field, such interactions can lead to phases with broken symmetry and long-range order of the magnetic moments. Most prominently, ferromagnetic and antiferromagnetic interactions describe the tendency of neighboring moments to align in parallel or antiparallel configurations, respectively.

Magnetic interactions seem intuitive when considering two interacting magnetic dipoles. However, the strength of dipole-dipole interactions between the atoms and electrons that form a solid-state system are much too weak in order to explain the properties of most magnetic materials [Isi25, Ash76]. Instead, the emergence of magnetic interactions in solids is fundamentally connected to the quantum-mechanical nature of electrons [Aue94]. Therefore, it could only be understood after fundamental concepts, such as the Pauli principle and the quantization of angular momenta, had been established.

The first model which offered a conclusive explanation of magnetic interactions in a solid was developed by Werner Heisenberg in 1928 [Hei28]. It extended the method that Walter Heitler and Fritz London had established one year earlier in an attempt to understand the binding energy between two hydrogen atoms [Hei27]. As Heitler and London realized, a so-called covalent bond can arise from the exchange of two electrons localized at the individual atoms, reducing the energy of the system by the superexchange energy J . However, this exchange process only occurs when the spatial wave function of the two electrons is symmetric with respect to their exchange. Due to the antisymmetry of the total wave function of the fermionic electrons, this necessarily leads to a completely antisymmetric two-particle spin wave function, which can only be realized for an antiparallel alignment of the two spins. As noticed by Heisenberg, this concept can be transferred to solid-state systems, where antiferromagnetic interactions arise from the exchange of electrons in a spin-singlet configuration localized at neighboring atoms [Hei28, Aue94].

The connection between individual spin singlets and the antiferromagnetic

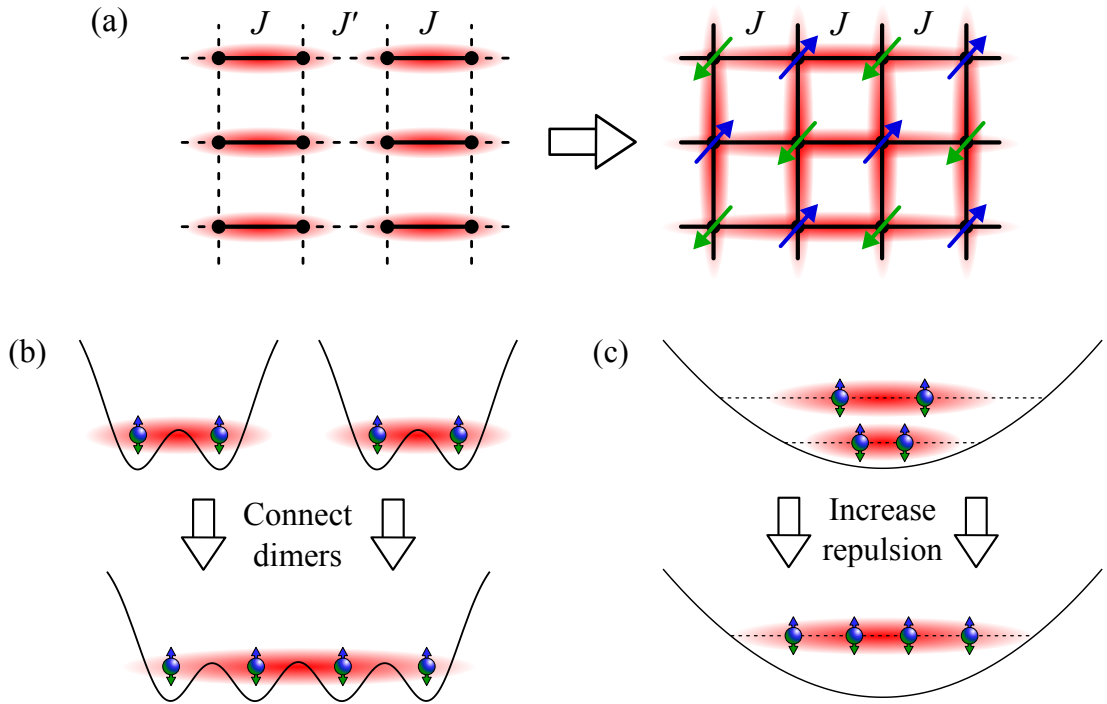


Figure 1.1.: Assembling ground-state spin systems from separated spin singlets. (a) Dimerized two-dimensional lattice with alternating strong bonds (solid lines) and weak bonds (dashed lines). Antiferromagnetic correlations are symbolized by red clouds. For a vanishing coupling strength along the weak bonds, the ground state of the system consists of one spin singlet on each of the strong bonds. When the dimers are connected, the spin singlets delocalize and a phase transition to the antiferromagnetic ground state with long-range order occurs. Figure adapted from Ref. [Sac08]. (b) Two individually prepared spin-singlets in double-well potentials are combined to create the antiferromagnetic ground state of a four-well system. (c) Creation of an antiferromagnetic spin chain in an one-dimensional harmonically-trapped system. For no interactions, each of the two lowest trap levels is occupied by one spin singlet. For finite interactions, the single-particle trap levels are not eigenstates of the system anymore and the spin singlets delocalize. In the limit of infinitely strong repulsion, the atoms form a Heisenberg spin chain with an antiferromagnetic ground state.

ground state of a homogeneous system is most apparent in a dimerized lattice. Such a lattice consists of one-dimensional spin chains with alternating strong and weak covalent bonds and additional weak bonds between these spin chains in the case of two and three-dimensional lattices [Fig. 1.1(a)]. In this lattice, a spin-

singlet on a strong (weak) bond reduces the energy of the system by J (J'). For the limiting case of a vanishing coupling strength on weak bonds ($J' = 0$), the lattice consists of separated dimers. When the spin pairs on each of these dimers are in a singlet configuration, the system is in its ground state. This ground state is nondegenerate and separated from the first excited state by the superexchange energy J . The other limit of the dimerized lattice is the homogeneous case with an equal coupling strength between all nearest-neighbor sites ($J = J'$). In this case, the spin singlets can not be attributed to individual bonds in the lattice anymore and are instead delocalized over the lattice. While for the one-dimensional dimerized lattice an adiabatic connection exists between the ground states at $J' = 0$ and $J' = J$ [Mat01, Sac08, Lub11], the ground state of the two-dimensional Heisenberg model undergoes a quantum phase transition into a state with long-range alternating spin order [Mat01, Sac08].

Since the Heisenberg model is a pure spin model it only explains the origin of magnetism in an insulator with exactly one unpaired electron per atom. In 1963, John Hubbard extended this picture by defining the most basic model that connects insulating and metallic phases of solid-state systems [Hub63]. Within this model, the physics of interacting electrons in a lattice of ion cores is reduced to only two fundamental processes: the hopping of electrons from one lattice site to a neighboring one and the Coulomb interaction of two electrons occupying the same lattice site. For weak interactions, the model describes a metallic system, where electrons move freely through the lattice. This motion is only restricted by the antisymmetry of the fermionic wave function, which prohibits two electrons with a symmetric spin wave function to occupy the same site. As a consequence, each site can be occupied by maximally two electrons, one spin-up and one spin-down electron in a spin-singlet correlation. As for the magnetic interactions in the Heisenberg model, on-site interactions in the Hubbard model are hence limited to spin singlets. For strong enough on-site interactions, the ground state of the half-filled Hubbard model, which has on average one electron per site, undergoes a phase transition into an insulating state. In this so-called Mott insulator, each lattice site is occupied by exactly one electron and the system can be described by an effective Heisenberg model [Aue94].

Despite the conceptual simplicity of these models, their application to many-body systems is still an ongoing topic of research with many open questions. Especially, antiferromagnetic correlations between electrons are of particular interest due to the observation of high-temperature superconductivity in antiferromagnetic materials [Bed86, Nor11]. Yet, even after nearly 30 years of theoretical efforts, it is still not known if the Hubbard model suffices to explain these observations [And87, Ess10]. Except for special cases, like the half-filled one-dimensional Heisenberg and Hubbard models [Gia04], the analytical solution of these problems

is often prevented by the complicated interplay of interactions, quantum fluctuations, and the geometry of the underlying lattice [Ess10]. Additionally, numerical simulations of fermionic quantum many-body systems are typically limited to only few particles by the exponential growth of their complexity with the system size.

This deficiency of classical computers in simulating quantum many-body models has inspired the idea of experimentally simulating these models with systems that inherently possess quantum-mechanical properties, but are easier to control than electrons in a solid [Fey82]. Ultracold-atom experiments were established as a prime candidate for this task by the successful cooling of both bosonic [And95, Dav95] and fermionic [DeM99] neutral atoms into the regime of quantum degeneracy. The simulation of solid-state models in such experiments was further encouraged by the possibility of trapping ultracold atoms in the standing-wave intensity pattern of crossed laser beams [Jak98, Dua03, Jak05, Blo08a, Ess10]. In this approach, the atoms mimic the electrons of a solid-state system, while the laser light provides a periodic potential, called optical lattice, that resembles the lattice of ion cores.

Using ultracold bosonic atoms in optical lattices, low-energy phases of the Hubbard model were successfully realized and used to simulate the quantum phase transition into the Mott insulating state [Gre02, Stö04, Spi07, Bak09]. In contrast to the case of electrons in a solid-state system, the superexchange interactions in a bosonic Mott-insulator are ferromagnetic and favor the parallel alignment of neighboring spins. A single-component Mott-insulator of bosonic atoms can therefore be seen as the ground state of the bosonic Heisenberg model. Recently, the dynamics of spin excitations above this ferromagnetic ground state was explored by selectively changing the internal state of individual atoms [Fuk13a, Fuk13b]. Additionally, exchange couplings in a two-component Bose gas were investigated in an array of isolated double wells [Tro08].

Although Mott-insulating states could also be realized with two-component Fermi gases [Jör08, Sch08], the simulation of the antiferromagnetic Heisenberg model in this system has proven to be a great challenge [McK11]. This is mostly due to the minuscule energy scale of superexchange processes, which typically correspond to temperatures below 1 nK, and the limited efficiency of evaporative cooling schemes in fermionic quantum gases [McK11]. In recent experiments, optimized lattice potentials [Har15] and the redistribution of entropy in the optical lattice [Gre13] allowed to approach the antiferromagnetic state and observe short-range spin correlations in various lattice geometries [Gre13, Har15, Mes15]. However, long-range antiferromagnetic spin order of fermionic atoms in the Mott-insulating state with a correlation length exceeding the interparticle distance has not been observed yet.

In this thesis, we describe two experiments, which are first steps in a novel

bottom-up approach to the simulation of ground-state Hubbard and Heisenberg models of finite size. In contrast to more prevalent top-down experiments, where atomic gases are cooled in a bulk system and then loaded into an optical lattice, this approach follows the idea of assembling a quantum many-body system from individual components [Kau14, Mur15a, Les15]. In our case, these individual components are isolated atom pairs in spin-singlet configurations. We prepare these spin singlets with a fidelity exceeding 95 % in the ground state of a single optical microtrap [Ser11b]. Their spin symmetry is of major importance for our approach, since for equal numbers of spin-up and spin-down particles also the ground states of both the Hubbard and the Heisenberg model have a total spin of $S = 0$ [Lie89, Lie62]. Following the ideas presented in Fig. 1.1(a), these individually prepared spin singlets can be adiabatically combined in order to create the ground state of larger Heisenberg and Hubbard systems [Mat01, Sac08, Lub11].

In a first experiment [Mur15a], we start with a spin singlet in a single optical microtrap and slowly ramp on a second microtrap in order to adiabatically reach the two-particle ground state in a double-well potential. With only two atoms and one tunnel junction, this double-well system can be seen as the fundamental building block of the Hubbard model. We demonstrate independent control over the interaction strength between the atoms and the potential shape and find excellent agreement with the predictions of a two-site Hubbard model. In the future, we plan to create a series of such double-well systems and adiabatically combine them in order to reach low-entropy phases in a homogeneous lattice [Fig. 1.1(b)] [Lub11]. In a second experiment [Mur15b], we use two-component ground-state systems of up to four atoms in the potential of a single microtrap to realize Heisenberg spin chains. In this experiment, different spin singlets are initially prepared on different trap levels and subsequently coupled by introducing repulsive interparticle interactions [Fig. 1.1(c)]. The resulting Heisenberg spin chains are stabilized by the strong repulsive interactions and the one-dimensional geometry of the microtrap, without the need for an external periodic potential. This work constitutes the first observation of quantum magnetism with ultracold fermionic atoms that exceeds nearest-neighbor correlations.

Outline

The thesis is structured in the following way. In Ch. 2, we discuss the physics of two-component Fermi gases in one dimension. We specifically introduce the energy spectrum of one-dimensional systems of few interacting atoms, which are realized in the experiments presented later in this thesis. Afterwards, we introduce the Heisenberg Hamiltonian in Ch. 3. We show how it emerges from superexchange interactions between nearly separated particles and discuss its realization

in quantum-gas experiments. In Ch. 4, we explain the experimental setup and how we can use it to deterministically prepare and detect samples of few fermionic atoms. We will specifically focus on the setup for the generation of arrays of partially overlapping microtraps that allowed us to prepare an isolated double-well potential. In following two chapters, we present the two main experimental studies of this thesis. First, in Ch. 5, the simulation of the two-site Hubbard model with two atoms in a double-well potential. Second, in Ch. 6, the realization of Heisenberg spin chains of up to four atoms in a single optical microtrap.

2. Strongly interacting few-fermion systems in one dimension

The experiments described in this thesis are performed on strongly-interacting quasi-one-dimensional systems of ultracold fermionic atoms. In this chapter we will explain the meaning and significance of the expressions in the last sentence. The purpose of this chapter is to compile the theoretical and experimental background that is necessary for the understanding of the following chapters.

We will start in Sect. 2.1 with an introduction on quantum-degenerate Fermi gases and specifically concentrate on spin-1/2 systems. We will see that the spin state of two spin-1/2 particles can either belong to a singlet, or a triplet depending on the symmetry of the spin wave function. This symmetry strongly influences the scattering properties of ultracold fermionic atoms. Specifically, two ${}^6\text{Li}$ atoms with low enough kinetic energy can only interact when they are in a spin-singlet state, while two atoms in a spin-triplet state are noninteracting. We will repeat the main steps leading to this important result and then describe how these interactions can be tuned using magnetic Feshbach resonances in Sect. 2.2. We will also discuss how the scattering properties of ultracold atoms change in the so-called quasi-1D regime, which is reached when the atomic motion is confined to only one spatial dimension. In Sect. 2.3, the energy spectrum and wave function of few-fermion systems in the quasi-1D regime will be discussed. Finally, in Sect. 2.4, we will introduce the Tonks-Girardeau gas and the concept of fermionization, which is a powerful method for the description of strongly interacting 1D systems of bosons or multicomponent fermions. This last section will be of special importance for the realization of Heisenberg spin chains in our experiment, which is the topic of Ch. 6.

2.1. Ultracold Fermi Gases

When the wave functions of identical particles overlap, the properties of the system are influenced by the exchange symmetry of the particles. In this case, two types of particles, bosons and fermions, have to be distinguished. Identical bosons have a completely symmetric wave function under the exchange of any two particles.

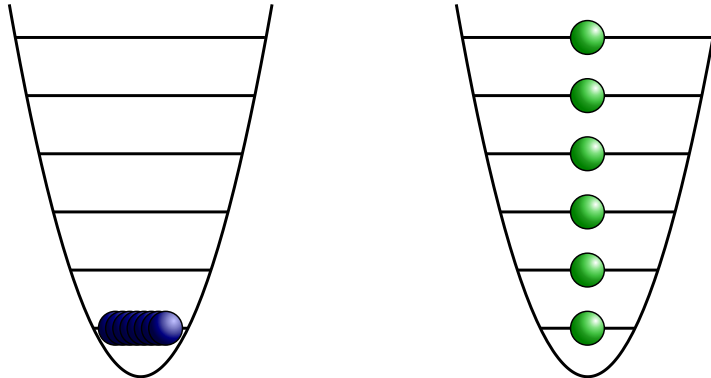


Figure 2.1.: Ground state distribution of identical noninteracting bosons (a) and fermions (b) in a harmonic trap. While identical bosons all condense into the single-particle ground state of the trap, identical fermions populate the lowest trap levels with one particle each.

This so-called Bose-Einstein statistics allows arbitrary numbers of bosons in each quantum state, which leads to the condensation of bosons in the systems ground state for low enough temperatures [Fig. 2.1(a)]. In contrary, the wave function Ψ^F of identical fermions has to be completely antisymmetric under the exchange of two particles. This can formally be written as

$$P_{ij}\Psi^F = -\Psi^F, \quad (2.1)$$

where the permutation operator P_{ij} interchanges any two particles i and j . As a direct consequence of this so-called Fermi-Dirac statistics, the wave function of two identical fermions that occupy the same single-particle state vanishes. The fact that two identical fermions can therefore never occupy the same state is called the Pauli exclusion principle. Following this principle, the many-particle ground state of N trapped fermions is realized when the N lowest trap levels are occupied with one fermions each [Fig. 2.1(b)].

The many-particle wave function Ψ^F of N fermions on N distinct single-particle trap levels $\psi_1 \dots \psi_N$ can then be constructed from product states of these single-particle trap levels by using the Slater determinant

$$\Psi^F(1, 2, \dots, N) = \frac{1}{\sqrt{N!}} \begin{vmatrix} \psi_1(1) & \psi_2(1) & \cdots & \psi_N(1) \\ \psi_1(2) & \psi_2(2) & \cdots & \psi_N(2) \\ \vdots & \vdots & \ddots & \vdots \\ \psi_1(N) & \psi_2(N) & \cdots & \psi_N(N) \end{vmatrix}. \quad (2.2)$$

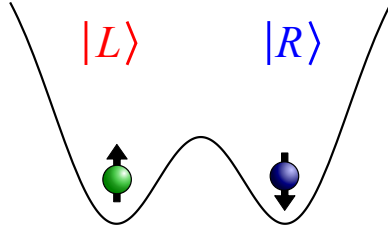


Figure 2.2.: Two spin-1/2 particles in a double well. Each particle is in a superposition of the spin states $|\uparrow\rangle$ and $|\downarrow\rangle$ and the spatial states $|L\rangle$ and $|R\rangle$. The total wave function of two fermionic atoms has to be antisymmetric, leading to six different eigenstates (Tab. 2.1) [Foo11].

The Slater determinant can also be rewritten as

$$\Psi^F = \mathcal{A} \prod_{\nu=1}^N \psi_{\nu}(\nu), \quad (2.3)$$

where the antisymmetrizing operator is given by

$$\mathcal{A} = \frac{1}{\sqrt{N!}} \sum_P (-1)^P P. \quad (2.4)$$

Here, the sum is over all $N!$ permutations of the particles and $(-1)^P$ is $+1$ (-1) for even (odd) permutations [Fli05, Sak85].

2.1.1. Two-component Fermi systems

Spin-1/2 particles are of special interest in physics, since both leptons and quarks belong to this category. Like all particles of half-integer spin, these elementary particles are fermions and they can only be in one of two spin states, which are distinguished by the secondary spin quantum number ($m_S = \pm 1/2$). In our experiment, we realize an (iso-)spin-1/2 system by restricting fermionic ${}^6\text{Li}$ atoms to exactly two hyperfine states.

As a minimum example of such a system, we discuss the case of two spin-1/2 particles which can each be in one of two orbitals (Fig. 2.2). We call the two possible spin states *up* ($|\uparrow\rangle$) and *down* ($|\downarrow\rangle$) and the two spatial states *left* ($|L\rangle$) and *right* ($|R\rangle$). In Ch. 5, we discuss the realization of this textbook example in our experiment with two fermionic atoms in an isolated double-well potential.

We assume that no coupling between spin and spatial degrees of freedom exists and therefore both single-particle and two-particle wave functions can be separated

$\Phi^{(A)}$	$\chi^{(S)}$
	$ \downarrow\downarrow\rangle$
$\frac{1}{\sqrt{2}} (LR\rangle - RL\rangle)$	$\frac{1}{\sqrt{2}} (\downarrow\uparrow\rangle + \uparrow\downarrow\rangle)$
	$ \uparrow\uparrow\rangle$
$\Phi^{(S)}$	$\chi^{(A)}$
$ LL\rangle$	
$\frac{1}{\sqrt{2}} (LR\rangle + RL\rangle)$	$\frac{1}{\sqrt{2}} (\downarrow\uparrow\rangle - \uparrow\downarrow\rangle)$
$ RR\rangle$	

Table 2.1.: Spin and spatial wave functions of two noninteracting fermionic particles in a double well. The particles are either in a spatial singlet and a spin triplet (upper part), or in a spatial triplet and a spin singlet (lower part) [Foo11].

in a spin part and a spatial part. A two-particle spin wave function can now be expressed within the basis of all possible product states

$$\{ |\downarrow\downarrow\rangle, |\downarrow\uparrow\rangle, |\uparrow\downarrow\rangle, |\uparrow\uparrow\rangle \}, \quad (2.5)$$

while the same is true for the spatial wave function

$$\{ |LL\rangle, |LR\rangle, |RL\rangle, |RR\rangle \}. \quad (2.6)$$

Here, the first (second) entry in each ket characterizes the first (second) particle. Using the relation of Eq. 2.1, we know that the combined two-particle wave functions have to be antisymmetric under the exchange of the particles. This can be realized in two different ways. Either the spin wave function χ is antisymmetric (A) and the spatial wave function Φ is symmetric (S), or vice versa. As shown in Tab. 2.1, a symmetric wave function of space or spin can be realized in three different ways, while the realization of an antisymmetric wave function is always unique. A system with a symmetric spin (spatial) wave function is therefore part of a spin (spatial) triplet, while two atoms with an antisymmetric spin (spatial) wave function form a spin (spatial) singlet.

For more than two spin-1/2 particles the situation gets significantly more difficult, since now the spin wave function on its own can not have a completely

antisymmetric exchange symmetry anymore¹. But, as we will see many times throughout this thesis, it is often still possible to characterize the properties of many-body spin-1/2 systems by the amount of spin-singlet or spin-triplet correlations they contain. Important examples for this are the antiferromagnetic ground state of the Heisenberg model, which contains the maximum amount of spin-singlet correlations (see Ch. 3 and Ch. 6) [Sac08], and fermionic atoms in the regime of ultracold temperatures, which only interact when spin-singlet correlations are present (see Sect. 2.2). However, the spin-singlet correlations in a many-body system are in general not confined to two specific particles anymore. Instead they are delocalized over many particles and can therefore be seen as an collective property of the system².

2.2. Interactions in Fermi gases

In the investigation of many-body systems, the modeling of interparticle interactions is typically one of the central problems. In this section, we collect the basic concepts of interactions in ultracold quantum gases of fermionic atoms. Despite the complicated internal structure of atoms, the description of interactions between them can be greatly simplified (Sect. 2.2.1). For low enough temperatures, interactions reduce to only two-body scattering between atoms in a spin-singlet configuration and can be characterized by a single parameter, the s-wave scattering length a_{3D} . We will see that a_{3D} can be tuned in ultracold-atom experiments by using a magnetic Feshbach resonance (Sect. 2.2.3) [Chi10]. Magnetic Feshbach resonances will be essential for the generation of strongly-interacting atomic samples in Ch. 5 and Ch. 6. For atoms that are confined in a potential that restricts their movement to one or two spatial dimensions, the scattering properties change. Interactions between atoms in a quasi-1D confinement will be the topic of Sect. 2.2.4.

While the discussion in this section focuses on the phenomenological description of the respective concepts, detailed review articles on interactions in ultracold gases and Feshbach resonances are available [Blo08b, Ket08, Chi10].

¹This is due to the fact that in any spin-1/2 system of more than two particles at least two spins have to be identical.

²A prominent example for this principle is a cooper pair in BCS theory. Although a cooper pair is usually in a spin-singlet state it cannot be attributed to only two spin-1/2 particles but has to be understood as a collective effect.

2.2.1. Scattering in ultracold atomic gases

One of the main reasons, why interactions in ultracold gases of neutral atoms can generally be treated in a greatly simplified way is that these systems are typically very dilute. This can be seen by comparing the mean interparticle distance, which is typically $\leq 1 \mu\text{m}$, to the characteristic length scale of the Van-der-Waals potential between two particles, which has typical values of $r_0 \approx 50 a_0 \approx 3 \text{ nm}$ [Ket08], where a_0 is the Bohr radius. For these conditions, the probability of finding three or more atoms close to each other can be neglected and the interactions reduce to two-body scattering. The Schrödinger equation of such a two-particle scattering process can be written in relative coordinates as

$$\left(\frac{-\hbar^2 \nabla^2}{2\mu} + V_{\text{int}}(\mathbf{r}) \right) \Psi(\mathbf{r}) = E\Psi(\mathbf{r}), \quad (2.7)$$

where \mathbf{r} is the relative coordinate of the two particles, μ is the reduced mass and $V_{\text{int}}(\mathbf{r})$ is the scattering potential, which is assumed to be zero for large interparticle distances \mathbf{r} .

Partial wave expansion

For a central scattering potential $V_{\text{int}}(\mathbf{r}) = V_{\text{int}}(r)$, the scattering wave function can be expanded in partial waves $R_l(r)Y_{lm}(\theta, \phi)$. Here, Y_{lm} are spherical harmonics with an angular momentum quantum number l and a magnetic quantum number m and $R_l(r)$ is a radial wave function. Due to the central scattering potential, the problem is axially symmetric to the direction of the incoming wave and therefore the scattering wave function is independent of the azimuthal angle ϕ [Ket08]. For each radial wave function $R_l(r)$, we can now define a separate scattering channel that belongs to a specific l and write the adjusted Schrödinger equation as

$$\left(-\frac{\hbar^2}{2\mu} \left(\frac{\partial^2}{\partial r^2} + \frac{2}{r} \frac{\partial}{\partial r} \right) + V_{\text{eff}}(r) \right) R_l(r) = ER_l(r). \quad (2.8)$$

Here, $V_{\text{eff}}(r)$ is an effective scattering potential

$$V_{\text{eff}}(r) = \frac{l(l+1)}{2\mu r^2} + V_{\text{int}}(r), \quad (2.9)$$

which differs from the interaction potential in Eq. 2.7 for scattering channels with $l > 0$ [Flh05]. The first term in V_{eff} results in a centrifugal barrier, as shown in Fig. 2.3.

The partial wave expansion greatly simplifies the description of scattering pro-

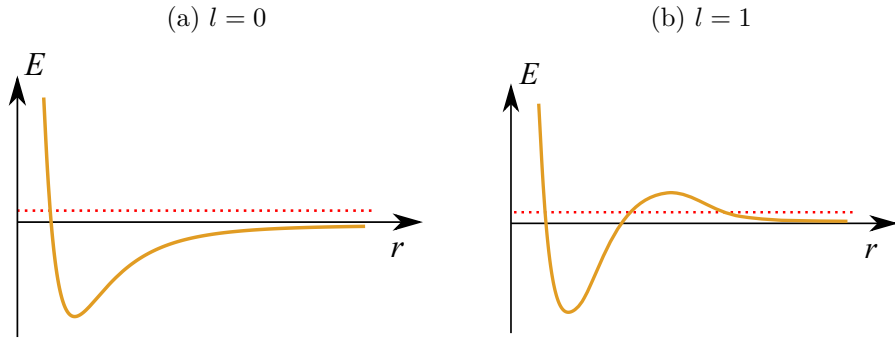


Figure 2.3.: Effective scattering potential for s-wave scattering (a) and p-wave scattering (b). If the energy of the scattering particle (red dotted line) is low enough, the centrifugal barrier blocks all scattering channels except for s-wave scattering with $l = 0$.

cesses in ultracold gases. Most of all, because scattering processes in different scattering channels (according to different l) can now be treated separately. Additionally, the exchange symmetry of the scattering wave function $\Psi_l(\mathbf{r}) = R_l(r)Y_{lm}(\theta, \phi)$ of a specific scattering channel is given by $\Psi_l(-r) = (-1)^l\Psi_l(\mathbf{r})$. This is of particular interest for scattering processes between identical quantum particles, where the exchange symmetry of the wave function is restricted (Sect. 2.1). For the case of two spin-1/2 fermions, where the possible wave function symmetries are shown in Tab. 2.1, only the following scattering channels are allowed:

$$\begin{aligned} l = 0, 2, 4, \dots & \quad \text{for two atoms in a spin-singlet configuration,} \\ l = 1, 3, 5, \dots & \quad \text{for two atoms in a spin-triplet configuration.} \end{aligned} \tag{2.10}$$

The situation simplifies even further, because of the centrifugal barrier in the effective scattering potential. For typical temperatures in ultracold atom experiments of $T \lesssim 1\mu K$, the energy $E = k_B T$ of the colliding particles is lower than the centrifugal barrier of even the p-wave channel ($l = 1$). Therefore, the s-wave scattering channel ($l = 0$) is the only remaining possibility for particles to interact³. In combination with the restrictions in Eq. 2.10, we can conclude that cold fermionic atoms can only interact if they are in a spin-singlet configuration. Importantly, this results in the fact that a sample of identical fermions, in which atoms can only form spin triplets, will become noninteracting at low enough temperatures.

³Unless scattering of higher partial waves is not resonantly enhanced.

The s-wave scattering length

To characterize the strength of interactions during a scattering process, we consider an asymptotic solution for the scattering wave function $\Psi(\mathbf{r})$ outside of the range of the scattering potential. Assuming an incoming plane wave and an outgoing spherical wave $\Psi(\mathbf{r})$, results in a asymptotic scattering wave function of

$$\Psi(\mathbf{r}) = e^{i\mathbf{k}\cdot\mathbf{r}} + f(k, \theta) e^{ik'r}. \quad (2.11)$$

Here, \mathbf{k} is the wave vector of the incoming wave and $f(k, \theta)$ is the scattering amplitude that expresses the probability amplitude of scattering as a function of $k = |\mathbf{k}| = \sqrt{2\mu E/\hbar^2}$ and the scattering angle θ . We assume a fully elastic scattering process so that $k = k'$ has to be satisfied. Performing a partial wave expansion, the scattering amplitude $f(k, \theta)$ can be separated into the amplitudes of the individual scattering channels.

For low-energy scattering, $f(k, \theta)$ can be reduced to its ($l = 0$) component f_s , which is independent of the scattering angle θ and can be written as

$$f_s = \frac{1}{k \cot \delta_s - ik}, \quad (2.12)$$

where δ_s is the s-wave scattering phase. The physical meaning of δ_s can be directly motivated from the asymptotic form of the scattering wave function (Eq. 2.11). Since the amplitudes of the incoming and outgoing waves are fixed, the only effect the potential can have in an elastic scattering process is adding a phase shift to the outgoing wave. The whole influence of the potential is therefore reduced to one number.

In the low-momentum limit ($k \ll 1/r_0$, where r_0 is the characteristic length of the scattering potential), the scattering phase can be replaced by the 3D s-wave scattering length, which is defined as

$$a_{3D} = - \lim_{k \ll 1/r_0} \frac{\tan \delta_s}{k}. \quad (2.13)$$

While the absolute value of a_{3D} characterizes the strength of the s-wave interactions ($k|a_{3D}| \ll 1$ for weak interactions and $k|a_{3D}| \gg 1$ for strong interactions) its sign indicates whether the interactions are attractive ($a_{3D} < 0$) or repulsive ($a_{3D} > 0$).

The scattering potential

The low-momentum condition $k \ll 1/r_0$ used in the last section implies that the de Broglie wavelength of the particles and therefore the spatial extent of their

wave function is much larger than the characteristic length of the scattering potential⁴. In this limit, the atoms do not probe the internal structure of the scattering potential, which can instead be replaced by a simpler pseudo-potential. This pseudo-potential has to reproduce the correct s-wave scattering length a_{3D} [Ket08]. Typically, a regularized delta-potential $\delta_{\text{res}}(\mathbf{r}) \dots = \delta(\mathbf{r}) \frac{\partial}{\partial r}(r \dots)$ is used leading to an effective scattering potential given by

$$V_{\text{int}}(\mathbf{r}) = g_{3D} \delta_{\text{reg}}(\mathbf{r}). \quad (2.14)$$

Here, g_{3D} is defined as

$$g_{3D} = \frac{2\pi\hbar^2 a_{3D}}{m} \quad (2.15)$$

and called the potential strength or coupling constant.

2.2.2. Scattering resonances

While for most applications the scattering potential is replaced by the pseudo-potential (Eq. 2.14), its exact form is still necessary to determine the value of the scattering length a_{3D} . Specifically, both the absolute value and sign of a_{3D} depend on the energy of the highest bound state in the scattering potential. This can be understood by assuming a coupling to this bound state during the scattering process. If the bound state closely below the continuum energy of the scattering particles, it adds a positive phase shift of $0 \leq \delta_s(\text{mod } \pi) \leq \pi/2$ to the outgoing wave. According to Eq. 2.13, this results in a positive scattering length and therefore in repulsive interactions. The binding energy of the weakly-bound state can then be expressed as a function of the scattering length as [Ket08]

$$E_B = \frac{\hbar^2}{m a_{3D}^2}. \quad (2.16)$$

Equivalently, a virtual state closely above the continuum energy leads to a negative phase shift of $-\pi/2 \leq \delta_s(\text{mod } \pi) \leq 0$ and consequently to a negative scattering length and attractive interactions.

Whenever the potential is just deep enough to have a bound state on resonance with the continuum energy, the phase shift (modulo π) reaches $\delta_s = \pi/2$ and the s-wave scattering length diverges. Since the exact shape of the scattering potential in an atomic collision is normally not known, the position of scattering resonances and hence the value of a_{3D} in an atomic collision is hard to predict from ab initio

⁴For ultracold atoms, the de Broglie wavelength is on the order of $\sim 1\mu\text{m}$, while the scattering potential has a characteristic length of approximately 3nm [Ket08].

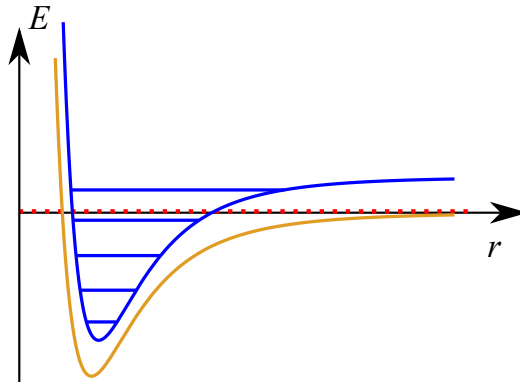


Figure 2.4.: Two-channel model for atomic scattering in the low-energy limit. If the continuum energy (red dotted line) of two atoms in an open scattering channel (yellow) is on resonance with the bound state of a closed scattering channel (blue) a Feshbach resonance can occur.

calculations. Instead, the scattering potential is usually replaced by the simplified pseudo-potential of Eq. 2.14 and a_{3D} is regarded as an experimental parameter.

2.2.3. Feshbach resonances

For two atoms in a particular scattering channel, the scattering phase can also be influenced by bound states of another channel, if a coupling to this channels exist. For simplicity, we assume that the second channel has a continuum energy above the energy of the incoming atoms. It is therefore a *closed* channel and the atoms always have to leave the scattering region in their initial *open* channel (Fig. 2.4). If the open and closed channels are coupled during the scattering process, the phase shift δ_s is affected by bound states in both channels.

This is of particular interest, when the energy of the closed channel can be tuned experimentally with respect to the energy of the open channel. If the bound state of the closed channel is tuned into resonance with the continuum energy of the open channel, the scattering length diverges (Sect. 2.2.2). This so-called Feshbach resonance is a fundamental tool in realizing strong interactions in ultracold atom experiments [Chi10]. Mostly, these experiments use magnetic Feshbach resonances, where the open and closed channel have different magnetic moments and therefore their energy difference can be tuned by changing the magnetic field. Phenomenologically, the scattering length close to such a magnetic Feshbach resonance can be written as

$$a(B) = a_{\text{bg}} \left(1 - \frac{\Delta B}{B - B_0} \right). \quad (2.17)$$

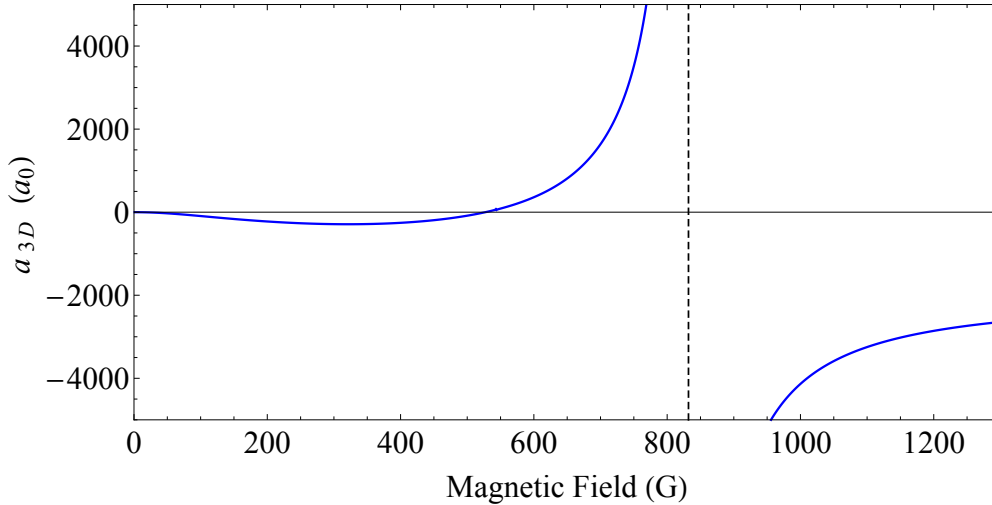


Figure 2.5.: 3D s-wave scattering length a_{3D} between the two lowest hyperfine states of ${}^6\text{Li}$ as a function of the magnetic offset field. A broad s-wave Feshbach resonance with a width of $\Delta B \approx 262$ G occurs at a magnetic field of $B \approx 832$ G [Zür13a]. Below the resonance, a_{3D} has a zero crossing at $B \approx 527$ G, where the system becomes noninteracting. Above the resonance, a_{3D} approaches the background scattering length of about $-2200a_0$ [Joc04].

Here, a_{bg} is the background scattering length of the initial channel, ΔB is the width of the Feshbach resonance and B_0 is the value of the magnetic field where the resonance occurs.

Feshbach resonances in ${}^6\text{Li}$

In ${}^6\text{Li}$, an exceptionally broad magnetic Feshbach resonance exists for scattering between the two energetically lowest hyperfine states (Fig. A.1). As shown in Fig. 2.5, it is located at a magnetic offset field of $B \approx 832$ G and has a width of $\Delta B \approx 262$ G [Joc04, Zür13a]. This allows for the precise control of the interaction strength at both positive and negative values of a_{3D} and for the realization of strongly-interacting Fermi gases. Also, due to a negative background scattering length, a_{3D} can be tuned to zero at approximately 527 G, resulting in a noninteracting Fermi gas.

2.2.4. Scattering in one-dimensional systems

When the motion of two colliding atoms is restricted to only one or two spatial dimensions, their scattering properties change [Bus98, Ols98]. In this section, we

will discuss the case of scattering in a one-dimensional (1D) confinement, which is of great importance for this thesis. We will show that a 1D coupling constant can be defined, which is closely related to the potential strength of the 3D pseudo-potential. Furthermore, we will discuss the model of confinement-induced resonances (CIR), which shows that the position of the scattering resonance in a quasi-1D systems is shifted compared to the 3D Feshbach resonance.

1D and quasi-1D

In the following discussion, we have to distinguish between two related concepts: True 1D and quasi-1D. True 1D is a purely theoretical idea that describes a situation in which all dynamics of a system happens along one spatial dimension, independent of the systems energy. In reality, this can not be achieved, since in any real system the radial confinement can only be of finite strength. Therefore, for large enough energies, excited states of the radial confinement will be populated and the movement of the particles will be in more than one spatial dimension. Still, if in a trap with strong radial confinement, the energy is low enough that particles predominantly populate the radial ground state, the system can be approximately described as 1D. Systems in this limit are then called quasi-1D.

In the experiments presented in Ch. 5 and Ch. 6, we realize quasi-1D systems. By focusing a single Gaussian laser beam, we create a strongly-elongated trapping potential for the atoms (see Sect. 4.3). For low atomic energies, this potential can be harmonically approximated and written as

$$V_{\text{harm}}(\rho, z) = V_{\perp}(\rho) + V_{\parallel}(z) = \frac{1}{2}m\omega_{\perp}^2\rho^2 + \frac{1}{2}m\omega_{\parallel}^2z^2. \quad (2.18)$$

Here, $V_{\perp}(\rho)$ is the potential in radial direction with $\rho = \sqrt{x^2 + y^2}$, $V_{\parallel}(z)$ is the potential in axial direction, and ω_{\perp} and ω_{\parallel} are the radial and axial trap frequencies. The aspect ratio

$$\eta = \frac{\omega_{\perp}}{\omega_{\parallel}}, \quad (2.19)$$

which characterizes how elongated the potential is, has typical values of $\eta \approx 10$ in our experiment⁵.

To realize a quasi-1D system in a trapping potential described by Eq. 2.18, all energies should be much smaller than $\hbar\omega_{\perp}$, which is the energy of the first excited level in the radial confinement. Therefore, the Fermi energy, which in a 1D harmonic trap is given by $E_F = N\hbar\omega_{\parallel}$, limits the maximum atom number in

⁵The realization of this trapping potential is described in Sect. 4.3. A detailed list of the trap parameters can be found in App. A.4.

each spin state to $N \ll \eta$. Also, the motion of the particles should be restricted to the few lowest axially excited states. Both conditions are fulfilled in the experiments presented in this work.

Scattering in 1D

To characterize scattering in a 1D system, the goal is to replace the 3D pseudopotential in Eq. 2.14 by its one-dimensional counterpart

$$V_{\text{int}}(r) = g_{1\text{D}}\delta(r), \quad (2.20)$$

where $g_{1\text{D}}$ is called the 1D potential strength or 1D coupling constant. To calculate the relation between $g_{1\text{D}}$ and $g_{3\text{D}}$, we assume in this section that the atoms are radially confined in a 2D harmonic potential ($V_{\perp}(\rho)$ in Eq. 2.18), but that atomic motion along the z axis is free. We further assume that the 3D wave function $\Psi(\mathbf{r}) = \phi_{\perp}(\rho)\psi_{\parallel}(z)$ factorized into a radial and an axial component and follow the calculations in Refs. [Ols98, Ber03].

Making the unrealistic assumption of a true 1D system, in which the atoms are always in the ground state $\phi_{\perp,0}(\rho)$ of the radial confinement, the 1D coupling constant $g_{1\text{D}}$ can be calculated by simply rescaling the 3D value $g_{3\text{D}}$ [Ber03]. This can be seen by integrating over the transversal density in the 3D pseudopotential

$$\begin{aligned} g_{1\text{D}}\delta(r) &\approx \int 2\pi\rho d\rho |\phi_{\perp,0}(\rho)|^2 g_{3\text{D}}\delta_{\text{res}}(\mathbf{r}) \\ &= 2\frac{g_{3\text{D}}}{a_{\perp}^2}\delta(r) \\ &= \frac{2\hbar^2 a_{3\text{D}}}{ma_{\perp}^2}\delta(r) \end{aligned} \quad (2.21)$$

Here, $a_{\perp} = \sqrt{\hbar/m\omega_{\perp}}$ is the harmonic oscillator length of the radial confinement. During the calculation, the identity $|\phi_{\perp,0}(0)|^2 = 1/\pi a_{\perp}^2$ for the ground state of a harmonic oscillator and Eq. 2.15, which relates $g_{3\text{D}}$ and $a_{3\text{D}}$, were used [Ber03].

Scattering in quasi-1D – Confinement-induced resonances

Despite the unrealistic assumption of a true 1D system, Eq. 2.21 is still a good approximation for the 1D coupling constant of a weakly-interacting quasi-1D system. However, it was shown in Ref. [Ols98] that this approximation fails if $a_{3\text{D}}$ approaches the harmonic oscillator length of the radial confinement [Ber03]. In this case an additional term has to be included and the 1D coupling constant can

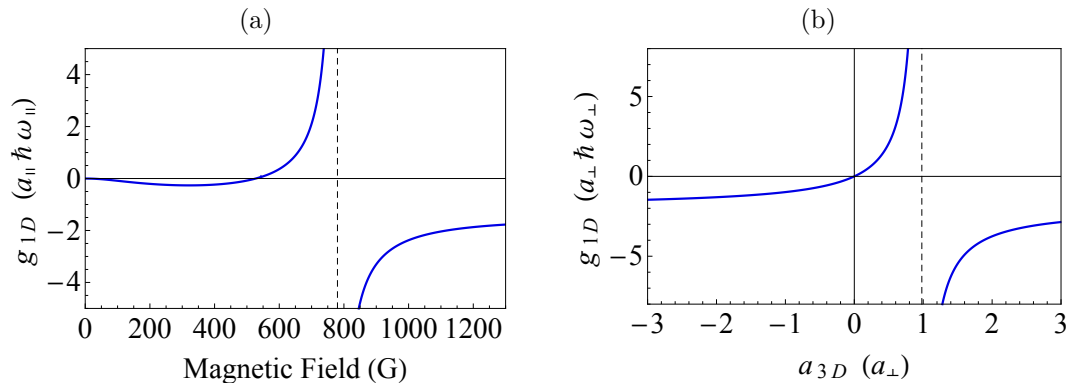


Figure 2.6.: Confinement-induced resonance in a quasi-1D system. (a) 1D coupling constant g_{1D} as a function of the 3D scattering length a_{3D} in units of the harmonic oscillator length of the transversal confinement a_{\perp} . For $a_{3D} \approx 1.0326a_{\perp}$, a confinement-induced resonance (CIR) occurs. (b) 1D coupling constant between ${}^6\text{Li}$ atoms in the two energetically lowest Zeeman sublevels (Fig. A.1). The atoms are trapped in the lowest axial states of a cylindrically symmetric harmonic trap with aspect ratio $\eta \approx 10$. When changing the magnetic offset field, a_{3D} changes as shown in Fig. 2.5 due to a magnetic Feshbach resonance at 832 G. At approximately 780 G, a_{3D} reaches $1.0326a_{\perp}$ and g_{1D} diverges.

be written as

$$g_{1D} = \frac{2\hbar^2 a_{3D}}{m a_{\perp}^2} \frac{1}{1 - C a_{3D}/(\sqrt{2}a_{\perp})}, \quad (2.22)$$

where $C/\sqrt{2} = -\zeta(1/2) \approx 1.0326$, and $\zeta(x)$ is the Riemann zeta-function [Ols98]. The second term in Eq. 2.22 shifts the position of the scattering resonance as shown in Fig. 2.6. Due to the dependence of g_{1D} on the radial confinement, such scattering resonances are called confinement-induced resonances (CIR).

A physical interpretation of the shifted resonance position was first provided in Ref. [Ber03]. Here, the CIR was explained as a scattering resonance between two incoming atoms in the ground state of the radial confinement and a bound state with radial excitation.

2.3. Interacting 1D systems

After discussing the scattering properties of ultracold atoms in 1D and defining the 1D coupling constant g_{1D} in the last section, we will now turn to the energy spectrum of one-dimensional few-atom systems at both attractive and repulsive

interactions. We will specifically concentrate on exact or perturbative solutions of few-particle two-component systems of ultracold fermionic atoms. The special case of infinitely strong repulsive interactions ($g_{1D} \rightarrow \infty$), where the atoms are in the so-called fermionization regime, will be the topic of the next section (Sect. 2.4).

2.3.1. Hamiltonian of two interacting atoms

We will first discuss the problem of two fermionic atoms in a harmonic trap that interact via s-wave scattering. Here, only atoms in a spin-singlet configuration will interact with each other, since the antisymmetric spatial wave functions of fermionic atoms in a spin-triplet configuration prohibits any scattering processes (see Sect. 2.2.1).

The Hamiltonian of two interacting ultracold atoms in a harmonic potential $V_{\text{harm}}(\mathbf{r})$ with cylindrical symmetry (Eq. 2.18) can be written as

$$H = -\frac{\hbar^2 \nabla_1^2}{2m} - \frac{\hbar^2 \nabla_2^2}{2m} + V_{\text{harm}}(\mathbf{r}_1) + V_{\text{harm}}(\mathbf{r}_2) + V_{\text{int}}(\mathbf{r}_1 - \mathbf{r}_2). \quad (2.23)$$

Here, \mathbf{r}_1 and \mathbf{r}_2 are the positions of the two atoms, and the interaction potential is given by the regularized delta potential of Eq. 2.14. In a harmonic potential, the relative (rel) and the center of mass (COM) motion separate and two independent single-particle Hamiltonians can be defined as

$$\begin{aligned} H_{\text{rel}}(\mathbf{r}) &= -\frac{\hbar^2 \nabla_r^2}{2\mu} + \frac{\mu}{m} V_{\text{harm}}(\mathbf{r}) + V_{\text{int}}(\mathbf{r}) \quad \text{and} \\ H_{\text{COM}}(\mathbf{R}) &= -\frac{\hbar^2 \nabla_R^2}{2M} + \frac{M}{m} V_{\text{harm}}(\mathbf{R}). \end{aligned} \quad (2.24)$$

Here, M is the mass of both atoms, μ is the reduced mass, and $\mathbf{r} = \mathbf{r}_1 - \mathbf{r}_2$ and $\mathbf{R} = (\mathbf{r}_1 + \mathbf{r}_2)/2$ are the relative and COM coordinate respectively.

The eigenfunction of H_{COM} can be separated in radial and axial parts and written as

$$\Psi_{\text{COM}}(\mathbf{R}) = \Theta_{n_{\parallel}}(z) \Phi_{n_{\perp},0}(\rho). \quad (2.25)$$

Here, $\Phi_{n_{\perp},0}$ is a 2D harmonic oscillator wave function with radial quantum number n_{\perp} and angular quantum number $m = 0$, and $\Theta_{n_{\parallel}}$ is a 1D harmonic oscillator wave function with axial quantum number n_{\parallel} . The energy of the COM motion can be written as

$$E_{\text{COM}} = \hbar\omega_{\parallel}(n_{\parallel} + \frac{1}{2}) + \hbar\omega_{\perp}(n_{\perp} + 1). \quad (2.26)$$

The problem of two interacting atoms in a harmonic trap is now reduced to finding

the solutions to the Schrödinger Equation

$$H_{\text{rel}}(\mathbf{r})\Psi_{\text{rel}}(\mathbf{r}) = E_{\text{rel}}\Psi_{\text{rel}}(\mathbf{r}) \quad (2.27)$$

of the relative motion.

2.3.2. Ground-state energy of two atoms in a harmonic trap

Noninteracting two-atom systems

For a vanishing interaction strength ($g_{1D} = 0$), the system becomes noninteracting and the solutions of Eq. 2.27 are harmonic oscillator wave functions as described for the COM motion (Eq. 2.25). In this case, the ground-state energy of two atoms in a spin-singlet configuration is given by the combined energies of the zero-point oscillations of relative and COM motion and can be written as

$$E_{S,0} = \hbar\omega_{\parallel} + 2\hbar\omega_{\perp} = \hbar\omega_{\parallel}(1 + 2\eta). \quad (2.28)$$

For a spin triplet, Pauli exclusion prohibits both particles from occupying the single-particle ground state of the trap and therefore the lowest energy is

$$E_{T,0} = E_{S,0} + \hbar\omega_{\parallel}. \quad (2.29)$$

Here one particle occupies the singlet-particle ground state of the trap, while the second particle occupies the first axially excited state.⁶

When the 1D coupling constant is not zero anymore, the energy of two interacting atoms in a spin-singlet configuration changes. In the following section, we will discuss the 3D solution of this problem [Idz06] and compare it to a 1D approximation [Bus98]. We will see that the 1D approximation provides remarkably good results, if the 1D coupling constant of Eq. 2.22, which incorporates the influence of the radial confinement, is used as an input [Idz06].

Energy shift in a cylindrically symmetric trap

To solve the Schrödinger equation of the relative motion (Eq. 2.27), the wave function $\Psi_{\text{rel}}(\mathbf{r})$ can be expanded in wave functions of the 3D harmonic oscillator with cylindrical symmetry (see Eq. 2.25). Inserting this expansion into Eq. 2.27 results in an implicit integral equation, which relates the energy of two attractively interacting atoms to the 3D s-wave scattering length [Idz06]. Using an analytic

⁶Since, the zero-point oscillations of the radial motion only add a constant term of $2\hbar\omega_{\perp}$ to the energy of all systems described in this thesis, we will neglect it in all further discussions.

continuation, the solution can be extended to repulsive interactions and the implicit equation can be written as

$$-\frac{1}{a_{3D}} = \frac{\eta}{(2\pi)^{3/2}} \sum_{n=0}^{\infty} \left(\frac{\Gamma(-\mathcal{E}/2 + n\eta)}{\Gamma(1/2 - \mathcal{E}/2 + n\eta)} \right) + \frac{\sqrt{\eta}}{(2\pi)^{3/2}} \zeta\left(\frac{1}{2}\right). \quad (2.30)$$

Here, $\Gamma(x)$ is the Euler gamma function and $\mathcal{E} = E - E_0$ is the energy of the system without the energy E_0 of the zero point oscillation [Idz06]. All energies and lengths in this equation are expressed in units of $\hbar\omega_{\parallel}$ and a_{\parallel} respectively, which are the characteristic units of harmonically trapped particles. The solutions of Eq. 2.30 can be found numerically and are shown as red lines in Fig. 2.7.

Energy shift in the 1D regime

Assuming a true 1D system and expanding the relative wave function of two interacting atoms in the axial harmonic oscillator states results in an approximate formula for the energy of the system. Similar to Eq. 2.30, an implicit equation can be calculated, which connects the energy shift due to interactions to the 1D coupling constant

$$-\frac{1}{g_{1D}} = 2^{3/2} \frac{\Gamma(-\mathcal{E}/2)}{\Gamma(-\mathcal{E}/2 - 1/2)}. \quad (2.31)$$

Again, energies and lengths were expressed in characteristic trap units. By relating g_{1D} to a_{3D} via Eq. 2.22, which describes the shifted position of the scattering resonance in a quasi-1D system [Ols98], this 1D approximation can be significantly improved [Idz06]. In contrast to the 3D case, Eq. 2.31 can be evaluated analytically and the solutions are shown as blue lines in Fig. 2.7.

As we can see in Fig. 2.7, the 1D model offers a good approximation of the exact energies for small coupling constants ($|g_{1D}| \ll 1$). The discrepancy between the 1D approximation and the exact 3D solution at $g_{1D} \gg 1$ is a result of a virtual populations of excited states during the scattering process. For large values of the interaction strength, radially excited states are included in the 3D evaluation, but they are missing in the 1D case. This also explains, why the 1D approximation worsens for excited states with energies approaching $\eta\hbar\omega_{\parallel} = \hbar\omega_{\perp}$. Also, the attractive ground state shows a clear disagreement between the 1D approximation and the exact solution. We will discuss this deviation in the next section.

Attractive and Repulsive interactions

Neglecting the zero-point oscillation energy of the radial motion, the ground-state energy of a noninteracting spin singlet of two atoms in a harmonic trap is given

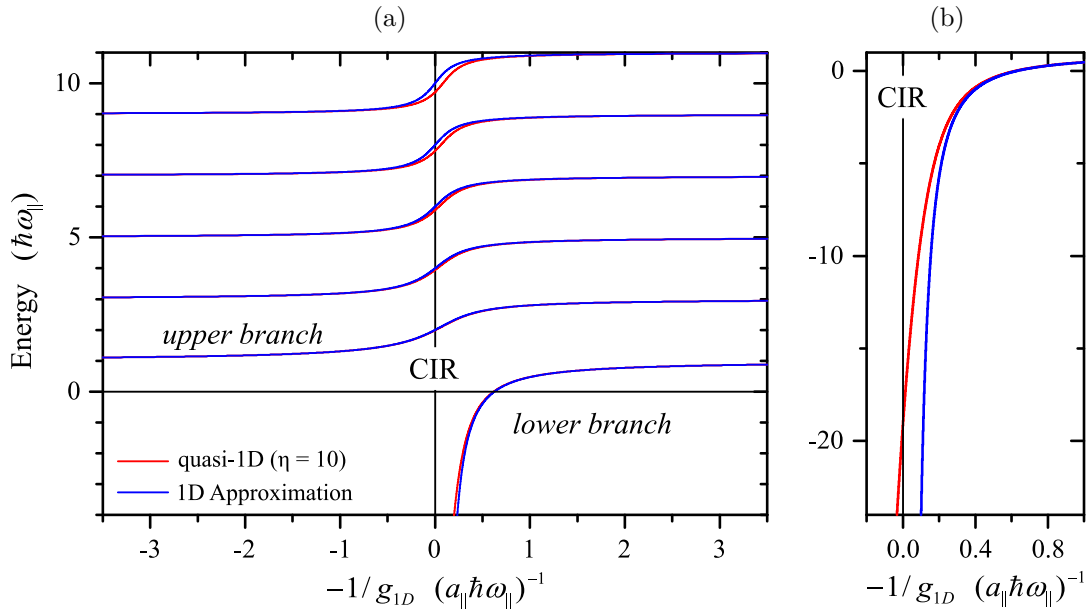


Figure 2.7.: Energy of two interacting atoms in a harmonic trap as a function of the inverse 1D interaction strength (Eq. 2.22) [Ols98]. Negative (positive) values of $-1/g_{1D}$ correspond to repulsive (attractive) interactions. In both (a) and (b), red lines depict the energy of a quasi-1D system with aspect ratio $\eta = 10$ [Idz06], while blue lines depict the energy of the system in a 1D approximation [Bus98]. The energy of the radial zero-point oscillation has been subtracted. (a) The *upper branch* and the *lower branch* are connected to the noninteracting two-particle ground state at $-1/g_{1D} \rightarrow -\infty$ and $-1/g_{1D} \rightarrow +\infty$. While the atoms in the *lower branch* form a molecule for increasing attractive interactions, they keep an atomic character in the *upper branch*, even if the system crosses the CIR to attractive interactions. Excited molecular states, which cross the *upper branch* close to the CIR are not depicted. (b) In the 1D approximation, the binding energy of two atoms in the *lower branch* diverges when approaching the CIR. In a real quasi-1D system, the molecule eventually loses its 1D character and its energy stays finite while crossing the CIR [Mor05b].

by $E_{S,0} = \hbar\omega_{\parallel}$ (Eq. 2.28), as shown in Fig. 2.7 for $-1/g_{1D} \rightarrow \pm\infty$. Finite values of $|g_{1D}|$ shift the energy upwards (downwards) if $-1/g_{1D} < 0$ ($-1/g_{1D} > 0$) corresponding to repulsive (attractive) interactions. The attractive and repulsive states that are connected to the noninteracting ground state of the system will in the following be called the *upper branch* and *lower branch*⁷.

In contrast to the homogeneous 3D case, where molecular states only exist for repulsive interactions, a 1D system supports a two-particle bound state also if the atoms interact attractively. For large $|g_{1D}|$ two atoms in the *lower branch* form a molecule, which achieves bosonic properties [Ast04]. In a 1D harmonic trap, the energy of this bound state diverges when approaching the scattering resonance [blue line in Fig. 2.7(b)]. However, in a real quasi-1D system, the molecule will lose its 1D character when a_{3D} approaches the harmonic oscillator length a_{\perp} of the radial confinement [Blo08b, Gha14]. The bound state energy therefore crosses the scattering resonance at a universal value of $2\hbar\omega_{\perp}$ [red line in Fig. 2.7(b)] and eventually approach the binding energy of a 3D molecule given by $\hbar^2/(ma_{3D}^2)$ (Eq. 2.16) [Mor05b, Blo08b].

Starting from the noninteracting limit at $-1/g_{1D} \rightarrow -\infty$, the energy of the *upper branch* continuously increases with growing g_{1D} until reaching a value of $E_{S,0} + \hbar\omega_{\parallel}$ at the position of the CIR [Bus98, Zür12b]. As we will see in the next section, the interacting atoms obtain properties of identical noninteracting fermions at this point [Gir60, Gir10, Zür12b], which allows for a simplified way of solving the Schrödinger equation. As a result of this so-called fermionization, the energies of a strongly interacting spin singlet and a spin triplet coincide at the position of the CIR as shown in Fig. 2.8. The energy of the spin singlet on the *upper branch* continuously crosses the CIR and becomes an excited state for $-1/g_{1D} > 0$ [Ast05, Hal09]. It continues to increase in energy until it reaches a limiting value of $E_0 + 2\hbar\omega_{\parallel}$ for vanishing attractive interactions ($-1/g_{1D} \rightarrow \infty$).

This structure of an *upper branch* and a *lower branch* exists for all excited states in the harmonic potential with symmetric spatial wave functions ($n = 0, 2, 4, \dots$) and therefore repeats itself in the energy spectrum every $2\hbar\omega_{\parallel}$. The attractive states of excited levels, which are not shown in Fig. 2.7, cross the *upper branch* of the ground state close to the CIR. In a harmonic trap, no couplings between the *upper branch* and excited molecular states are expected, but in an anharmonic potential, the atoms can couple to molecular states with radial COM excitations [Sal13].

⁷This nomenclature will later also be used for states with more than two atoms.

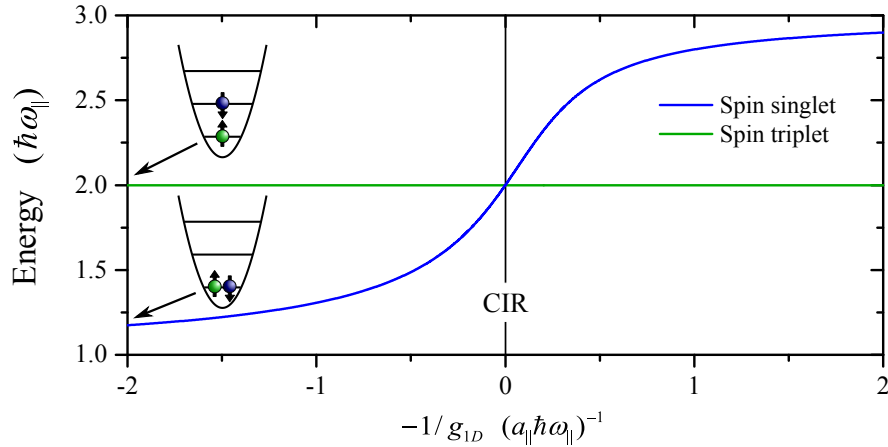


Figure 2.8.: Ground-state energy of a spin singlet (blue) or a spin triplet (green) of two harmonically trapped fermions in 1D as a function of the inverse 1D coupling constant. The sketches on the left side show the unsymmetrized single-particle level distributions of the singlet and triplet state in the noninteracting limit ($-1/g_{1D} = -\infty$). The states of the spin-triplet can not interact via s-wave scattering and have a constant energy of $2\hbar\omega_{||}$. In contrast, the energy of two atoms in a spin-singlet configuration depends on g_{1D} . At the position of the CIR ($-1/g_{1D} = 0$), the energy of spin singlets and spin triplets is identical and the system fermionizes (Sect. 2.4) [Gir60, Gir10, Zür12b].

2.3.3. Ground-state energy of more than two atoms

For quasi-1D systems of more than two interacting atoms, no explicit formulas for the energy as a function of the interaction strength are known. Therefore, a vast amount of numerically exact [Gha12, Gha13, Bro13, Bug13, Sow13, Cui14, Lin14] and other approximate methods [Bro13, Gha15, Gri15, D'A14] for the energy of two-component systems of three and more atoms were developed in recent years, largely inspired by the experimental progress in our group [Ser11b, Zür12b, Zür13b, Wen13b, Mur15b]. Also, much theoretical effort was directed toward identifying the eigenstates of these systems for $g_{1D} \rightarrow +\infty$ at the position of the CIR (i.a. [Gir07, Deu08, Gua09, Gir10, Vol14]), which will be the topic of the next section.

The conceptionally simplest and most widely used method of numerically calculating the energy of interacting particles is the exact numerical diagonalization of the problem [Gha12, Gha13, Bug13, Sow13, Cui14, Lin14]. In its most basic realization, the wave function of the many-body system is expanded in single-particle wave functions and subsequently diagonalized numerically. Typically, a

cut-off energy is defined, which limits the number of basis functions and therefore the size of the Hilbert space. This necessary cutoff restricts simple numerical diagonalization methods to relatively small atoms number of $N \lesssim 6$ and moderate interactions strengths. However, the capability of exact diagonalization methods could be significantly enhanced by incorporating the analytic solution of the two-body problem [Gha12, Gha13, Lin14]. Also, the investigation of the symmetry of individual states can help to limit the amount of basis functions and therefore improve the efficiency of numerical algorithms [Har14].

Lower branch and upper branch for more than two atoms

The general trend of the energy eigenstates of quasi-1D two-component systems of few harmonically trapped atoms is always similar to the two-particle case 2.3.2. This fact is not surprising, since two-particle scattering is the dominant form of interactions, even in strongly-interacting two-component Fermi systems⁸ [Ket08]. In the *lower branch*, the attractively interacting atoms form molecular pairs, which consist of one spin-up and one spin-down atom in a spin-singlet configuration [Ast04, Mor05b]. For equal number of spin-up and spin-down atoms, the system forms a bosonic gas with repulsive interactions between the pairs [Mor05a, Blo08b]

Also the general trend of the states on the *upper branch* is similar for any two-component few-fermion system. But, in contrast to the case of one spin-up and one spin-down atom, where only one singlet and one triplet states exist, more eigenstates can be found for higher atoms numbers. For N_\uparrow spin-up and N_\downarrow spin-down atoms, the number of states in each multiplet is given by

$$M = \binom{N_\downarrow + N_\uparrow}{N_\downarrow}. \quad (2.32)$$

As an example, the ground state multiplet of the ($N_\uparrow = 2, N_\downarrow = 1$) system is shown in Fig. 2.9.

As for the case of two atoms, the highest excited state of each multiplet below resonance is a noninteracting state with a completely antisymmetric spatial wave function. Furthermore, all M states of the multiplet are degenerate at $-1/g_{1D} = 0$ (see Sect. 2.4) with an energy of $\hbar\omega_{||}(N_\uparrow + N_\downarrow)^2/2$. Above the CIR ($-1/g_{1D} > 0$), each state gains as much energy as below ($-1/g_{1D} < 0$).

⁸This is due to the Pauli principle that prohibits two identical fermions from coming close to each other.

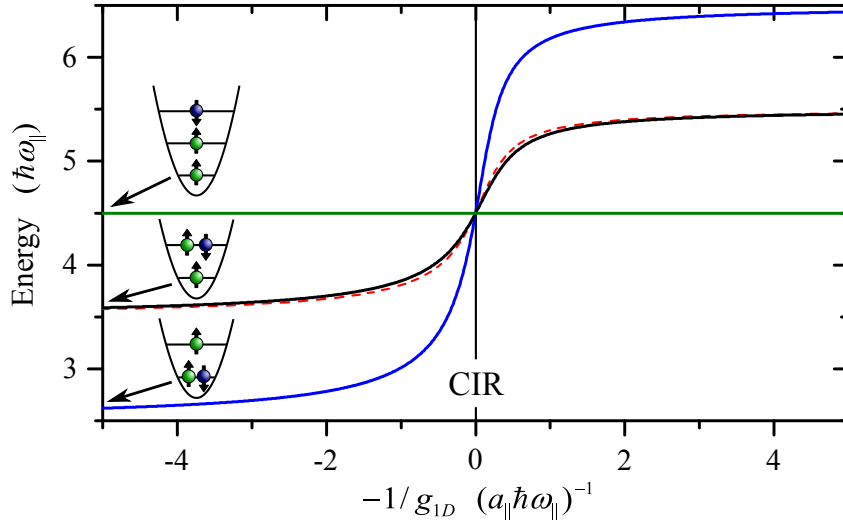


Figure 2.9.: Energies of the states of the *upper branch* of two spin-up and one spin-down atoms in a harmonic 1D trap. The sketches on the left show unsymmetrized single-particle level distributions of the individual states in the noninteracting limit ($-1/g_{1D} = -\infty$). The solid lines show approximations for the energy of three particles as a function of $-1/g_{1D}$. The state depicted by the green line has a completely antisymmetric spatial wave function and is therefore noninteracting for any value of g_{1D} . At the position of the CIR, all three states are degenerate and have an energy of $4.5\hbar\omega_{||}$. The red dashed line compares the energy of the intermediate state (black line) to the energy of an isolated two-particle spin singlet (blue line in Fig. 2.8) shifted by $2.5\hbar\omega_{||}$. The good agreement between both curves shows that the intermediate state can be seen as an interacting spin singlet and a noninteracting spectator atom [Lin14]

2.4. Fermionization of ultracold atoms

In the last section, it was shown that for a diverging coupling constant ($g_{1D} \rightarrow \infty$) a 1D system of two strongly-interacting fermionic atoms in a spin-singlet configuration obtains the energy of two identical noninteracting fermions. The basic principle behind this observation, which in fact is much more general, is called fermionization. It was originally proposed as a one-to-one mapping between the wave functions of impenetrable identical bosons and identical fermions in one-dimensional systems [Gir60]. The main idea behind the fermionization of bosons is that for a diverging 1D coupling constant, the interactions between bosons have just the same strength as the Pauli pressure between identical fermions. The impenetrable bosons will thereby obtain the same energy and density distribution as

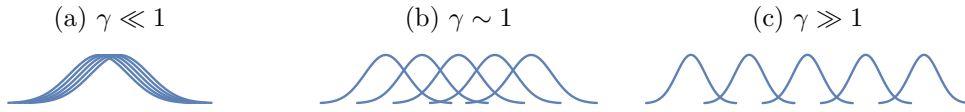


Figure 2.10.: Fermionization of identical bosons in 1D. (a) For weak interactions and cold temperatures, trapped bosons form a Bose-Einstein condensate and populate the same state. (b) Intermediate interaction cause the single-particle wave functions to separate. (c) For strong interactions, the single-particle wave functions completely separate and the system reaches the Tonks-Girardeau regime. Figure adapted from Ref. [Kin04].

a Fermi system.

In this section, we will first explain this mapping between the wave functions of identical bosons and fermions (Sect. 2.4.1) [Gir60], before discussing the fermionization of two-component Fermi systems (Sect. 2.4.2) [Deu08, Gir10].

2.4.1. Fermionization of identical bosons

In a 1D gas of trapped identical bosons, different regimes can be identified depending on the strength of interparticle interactions [Pet00]. The regimes are usually characterized using the dimensionless Lieb-Liniger parameter

$$\gamma = \frac{mg_{1D}}{\hbar^2 n}, \quad (2.33)$$

where n is the 1D density. For $\gamma \ll 1$ and low enough temperatures, a trapped 1D Bose gas forms a Bose-Einstein condensate, where all bosons occupy the single-particle ground state [Fig. 2.10(a)]. In this limit, the single-particle wave functions overlap completely. For growing values of γ the particles start to separate in order to minimize the interaction energy in the system [Fig. 2.10(b)]. Finally, in the limit of $\gamma \gg 1$, the so-called Tonks-Girardeau limit, the single-particle wave functions separate completely and the bosons become impenetrable [Gir60, Kin04, Kin05]. Assuming two-body contact interactions as introduced in Eq. 2.20, this complete separation of single-particle wave functions is the only possibility to prevent the interaction energy from diverging for a diverging coupling constant.

The infinitely strong interactions therefore impose the condition

$$\Psi^B(z_1, \dots, z_N) = 0 \quad \text{if} \quad z_i - z_j = 0, \quad 1 \leq j < i \leq N \quad (2.34)$$

on the wave functions of N bosons with contact interactions⁹. The same condition is also true for N identical fermions, since the antisymmetry of the fermionic wave function prohibits two identical fermions to occupy the same position in space (see Eq. 2.2). This similarity inspired Girardeau to write the bosonic wave function Ψ^B as a symmetric version of a fermionic wave function Ψ^F

$$\Psi^B = \prod_P (-1)^P \Psi^F. \quad (2.35)$$

Comparing this mapping to the definition of a fermionic many-particle state via the Slater determinant (Eq. 2.2), we can see that the factor $(-1)^P$ removes the minus sign of every odd permutation of particles in Ψ^F and therefore creates a state with completely symmetric exchange symmetry. For ground-state systems, the Fermi-Bose mapping of Eq. 2.35 reduces to

$$\Psi^B = |\Psi^F| \quad (2.36)$$

In Ref. [Gir60], Girardeau argues that for any permutation of particles, the mapping in Eq. 2.35 is constant (either $+1$ or -1). Assuming that Ψ^F satisfies the systems Schrödinger equation, he then concludes that also Ψ^B does. Furthermore, he shows that both the energy spectrum and the density distribution of the bosonic and fermionic systems are identical.

Since Ψ^F can be calculated as the Salter determinant of product states of single-particle wave functions (Eq. 2.2), the complexity of finding the solution of a strongly-interacting Bose gas is vastly reduced by this mapping.

2.4.2. Fermionization of spin-1/2 fermions

The fermionization of identical bosons can be extended to multicomponent particles in 1D, and in particular to two-component fermions [Gir10, Zür12b]. As shown in Fig. 2.8, two harmonically trapped atoms in a spin-singlet configuration obtain the energy of two noninteracting identical fermion for $g_{1D} \rightarrow \infty$. In this limit, also the spatial wave functions of a spin singlet [Fig. 2.11(c)] can be related to the spatial wave function of two identical fermions [Fig. 2.11(f)] by the mapping established between bosons and fermions in Eq. 2.36. This fermionization of two fermionic particles was demonstrated in our group by measuring the energy of both a spin singlet and a spin triplet as a function of the interaction strength throughout the regime of strong interactions [Zür12b].

⁹The assumption of contact interactions is just a simplification. In general any kind of interactions with an "impenetrable core" is sufficient [Gir60].

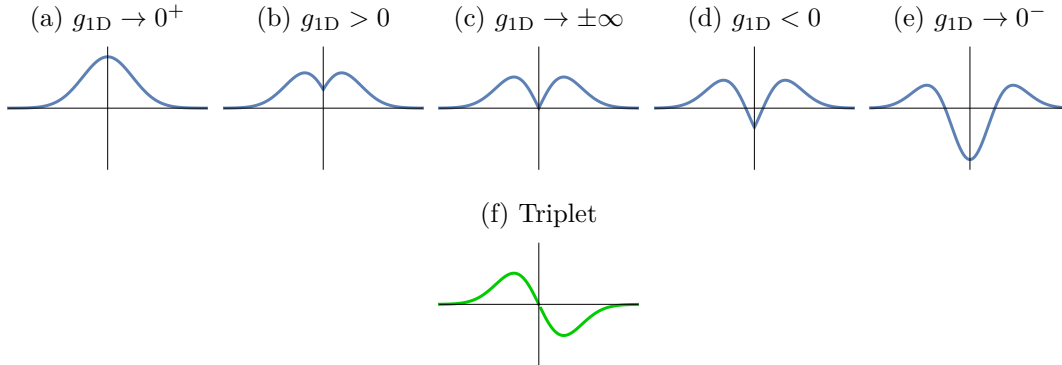


Figure 2.11.: Relative spatial wave function of two repulsively interacting atoms in a spin-singlet [(a)-(e)] or a spin-triplet configuration (f) [FA03, Gir10, Zür12b]. (a) Noninteracting ground state wave function. (b) Repulsive interactions lead to a cusp in the spatial wave function of a spin singlet, which approaches zero at the position of the CIR (c). At this point, the absolute of the spatial wave functions of two atoms in a spin-singlet and in a spin-triplet are identical. (d, e) Above the CIR, the relative wave function approaches the second excited eigenfunction of the harmonic oscillator.

However, for more than two spin-1/2 particles, the simple mapping of Eq. 2.35 is not sufficient anymore. This is due to the fact that the relative spatial wave function of two atoms in a two-component Fermi system can either be symmetric or antisymmetric. This additional degree of freedom, given by the spin of the particles causes the fermionized ground state of N_{\uparrow} spin-up and N_{\downarrow} spin-down particles to be M -fold degenerate (see Eq. 2.32) as already seen for three particles in Fig. 2.9.

Nearly 50 years after the original Fermi-Bose mapping, generalized fermionization schemes for multi-component particles were developed [Gir07, Deu08, Gir10]. They use the fact that for $g_{1D} \rightarrow \infty$ the spin and the density degrees of freedom of the particles decouple. States of multi-component particles can then be constructed from the wave function of noninteracting spinless fermions, as in the original Fermi-Bose mapping, combined with an arbitrary spin wave function [Deu08]. The difficult problem of solving a strongly-interacting system of multi-component particles is thereby reduced to a discrete spin model. The effective Hamiltonian of this spin model was later solved for small particle numbers by using a perturbative ansatz around the limit of $g_{1D} = \pm\infty$ [Deu14, Vol14]. It was furthermore recognized that in the case of spin-1/2 particles, this effective spin Hamiltonian is identical to a Heisenberg Hamiltonian (see Sect. 3.4.2) [Mat08, Deu14, Lev15].

2.4. Fermionization of ultracold atoms

These findings opened up the possibility of simulating Heisenberg spin chains with fermionic atoms in the fermionization regime. The realization of this approach in our experiment is the topic of Ch. 6 and Ref. [\[Mur15b\]](#).

3. Quantum magnetism with ultracold atoms

Magnetic interactions change the energy of two particles dependent on the relative orientation of their spins. In quantum many-body systems, such magnetic interactions can emerge between identical particles, even if their fundamental interactions, e.g. the Coulomb interactions between electrons or the s-wave interactions in a gas of ultracold atoms, are nonmagnetic [Aue94]. Since these magnetic interactions depend on the exchange symmetry of the interacting particles, they are often called exchange interactions. The paradigmatic model to explain the formation of magnetic phases due to exchange interactions is the Heisenberg model [Hei28], which will be the topic of this chapter.

We will start by explaining how exchange interactions emerge between two fermions in a double-well potential (Sect. 3.1). To describe this system, we will introduce and apply the formalism of the two-site Hubbard model [Hub63]. We will see that in the limit of large repulsion, an effective Hamiltonian emerges that only acts on the spin state of the two particles. In the next section (Sect. 3.2), we will extend these ideas to a many-body Hubbard system and identify the effective Hamiltonian as the Heisenberg Hamiltonian [Hei28]. We will discuss the properties of its ground state and mostly focus on antiferromagnetic exchange interactions. Especially, the assembly of antiferromagnetic ground-state systems by combining individual spin-dimers will be discussed (Sect. 3.3) [Sac08], because of its importance for the experiments described in this thesis.

In the final section of this chapter (Sect. 3.4), we will review two methods of experimentally realizing the Heisenberg Hamiltonian by using systems of ultracold atoms as quantum simulators. The first method uses the already mentioned connection between the Heisenberg Hamiltonian and the Hubbard model with strong repulsive interactions (Sect. 3.4.1) [Jak98, Dua03]. The implementation of this method in our experiment with only two atoms in an isolated double-well potential is the topic of Ch. 5 [Mur15a]. In the second method, atoms in a strongly elongated trapping potential are brought into the fermionization regime (see Sect. 2.4) and used to simulate Heisenberg spin chains (Sect. 3.4.2) [Deu14]. The realization of such spin chains in our experiment, is discussed in Ch. 6 [Mur15b].

3.1. Superexchange interactions

Superexchange interactions have first been predicted to explain the binding energy in the ground state of the hydrogen molecule [Hei27]¹. There, the two hydrogen atoms exchange their electrons and thereby reduce the energy of the system, if the electrons are in a spin-singlet configuration. As it turned out, the concept of superexchange interactions is not dependent on the specific properties of the hydrogen atoms. Instead, it can be seen as the generic way of introducing magnetic interactions in a quantum many-body system [Aue94].

In this section, we will explain how superexchange interactions emerge between two fermions trapped in a double-well potential. We will use a two-site Hubbard Hamiltonian to model this system [Hub63]. The Hubbard model is one of the most fundamental models of correlated quantum many-body systems. Its popularity is often attributed to the fact that it is the simplest model for interacting quantum particles that can not be reduced to a single-particle theory [Aue94]².

3.1.1. The two-site Hubbard model

To explain the origin of superexchange interactions, it is necessary to include both the motion and the interactions of quantum-mechanical particles in the model. In the Hubbard model both of these processes are present, but they are reduced to their simplest possible form. Within this model, particles only move by tunneling from one well into a neighboring one and they only interact when occupying the same well.

The Hubbard model can be conveniently described by using the second quantization formalism. Within this formalism the operator $c_{i,s}^\dagger$ ($c_{i,s}$) creates (annihilates) a fermionic particles in spin state $|s\rangle = \{|\uparrow\rangle, |\downarrow\rangle\}$ and spatial state i . Many-body states can then be expressed within a Fock basis, where the number of spin-up or spin-down particles in each single-particle spatial state i is counted. The anti-symmetry of the fermionic wave function is ensured by the usual anticommutation relations between the creation and annihilation operators [Aue94].

¹Note that in solid state literature (i.e. p. 681 of [Ash76]), the exchange of spins on neighboring sites of a lattice is typically referred to as *direct exchange*, while only processes that involve nonmagnetic intermediate sites are referred to as *superexchange*. This differs from the usage of these term in this thesis, which follow Ref. [Aue94] (see p. 17). Here, *superexchange* is generally used to describe the process that allows two particles with nearly completely separated spatial wave functions to exchange their position and thereby change the energy of the system energy.

²The fundamental approximations leading to the Hubbard model, which are important for its implementation in an ultracold-atom experiment, are discussed in Sect. 3.4.1.

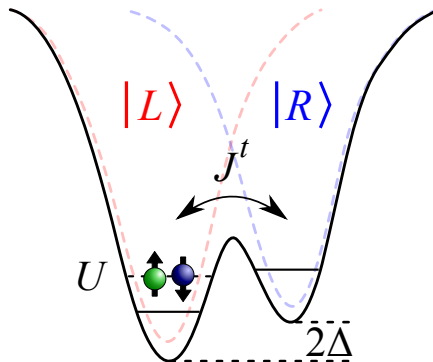


Figure 3.1.: Parameters of the two-site Hubbard model. Particles can tunnel between the right and the left well with a rate determined by the tunneling matrix element J^t . If both particles occupy the same well, they interact and change the energy of the system by the on-site interactions energy U . Additionally, the tilt Δ describes an energy difference between the two wells.

For the two-site Hubbard model (Fig. 3.1), the spatial states i are in good approximation the ground-states of the left and the right well. We first assume that the two wells are completely separated and therefore atoms can not tunnel between them. Assuming that particles occupying different wells do not interact, the Hamiltonian in this limit can be written as

$$H_{\text{int}} = U \sum_{i=\{L,R\}} n_{i,\uparrow} n_{i,\downarrow}. \quad (3.1)$$

Here, U is the on-site interaction energy and the operator $n_{i,s} = c_{i,s}^\dagger c_{i,s}$ counts the number of particles in spin state s and spatial state i . Importantly, only particles in a spin-singlet configuration can interact, since only for spin singlets, one spin-up and one spin-down particle are allowed to occupy the ground state of the same well. For repulsive interactions ($U > 0$), the energy of any superposition of the states $|\uparrow\downarrow, 0\rangle$ and $|0, \uparrow\downarrow\rangle$ with two particles on one site increases by U . In this case, the ground-state is fourfold degenerate and given by superpositions of the states $\{|\uparrow, \uparrow\rangle, |\uparrow, \downarrow\rangle, |\downarrow, \uparrow\rangle, |\downarrow, \downarrow\rangle\}$ with separated atoms.

If the two wells of the double-well system are not fully separated anymore, the spatial wave function of a particle localized in one well reaches into the other well. This allows single particles to tunnel from one site to the other, which can be expressed within second quantization as

$$H_t = -J^t \sum_{s=\{\uparrow,\downarrow\}} \left(c_{L,s}^\dagger c_{R,s} + c_{R,s}^\dagger c_{L,s} \right), \quad (3.2)$$

where J^t is the tunneling matrix element³. For two particles in the double-well system, the tunneling behavior of the particles is strongly influenced by their exchange symmetry. Thereby, only atoms in a spin-singlet correlation can tunnel, since two atoms in a spin-triplet state always have to occupy different sites.

The full Hamiltonian of the two-site Hubbard model is finally given by the sum of Eqs. 3.1 and 3.2 and an additional term describing an energy tilt Δ between the left and the right well

$$H_{\text{H}} = H_{\text{t}} + H_{\text{int}} + \sum_{s=\{\uparrow,\downarrow\}} (n_{L,s} - n_{R,s})\Delta. \quad (3.3)$$

This two-site Hubbard model can be solved analytically for any strength of U , J^t , and Δ . However, in order to understand the emergence of exchange interactions, it can nevertheless be instructive to calculate approximate solutions in the limit of strong repulsive interactions ($U/J^t \gg 1$). This is the topic of the next section⁴.

3.1.2. Superexchange in the Hubbard model

In the limit of strong repulsion ($U/J^t \gg 1$), the tunneling Hamiltonian H_{t} (Eq. 3.2) can be regarded as a small perturbation on the interaction Hamiltonian H_{int} (Eq. 3.1). Diagonalizing the states $\{|\uparrow, \uparrow\rangle, |\uparrow, \downarrow\rangle, |\downarrow, \uparrow\rangle, |\downarrow, \downarrow\rangle\}$ of the ground-state multiplet of H_{int} with respect to the perturbation Hamiltonian H_{t} leads to the spin singlet

$$|\psi^{(0)}\rangle = \frac{1}{\sqrt{2}} (|\uparrow, \downarrow\rangle + |\downarrow, \uparrow\rangle), \quad (3.4)$$

and the three spin-triplet states

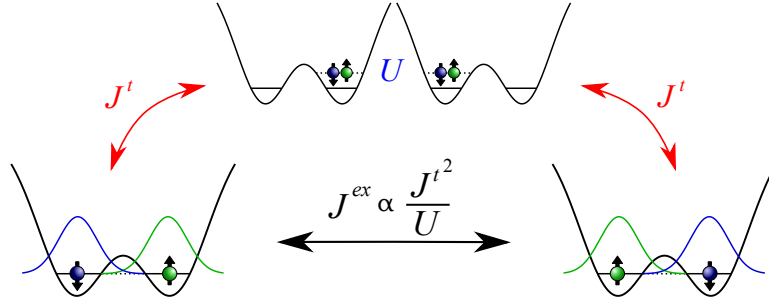
$$|\uparrow, \uparrow\rangle, \quad \frac{1}{\sqrt{2}} (|\uparrow, \downarrow\rangle - |\downarrow, \uparrow\rangle), \quad |\downarrow, \downarrow\rangle. \quad (3.5)$$

Since tunneling of the particles in a spin-triplet states is forbidden, only the energy of the spin singlet can change when applying H_{t} as a perturbation.

Starting from the spin-singlet state $|\psi^{(0)}\rangle$, the tunneling of only one particle leads to a final state with two particles in one well and is therefore strongly sup-

³Note that the letter J is used to describe both tunnel couplings and exchange couplings in order to be consistent with the notations in Ref. [Mur15a] and Ref. [Mur15b]. To avoid confusion, we will denote tunnel couplings as J^t and exchange couplings as J^{ex} .

⁴A detailed discussion of the eigenstates of the two-site Hubbard model at both repulsive and attractive interactions can be found in Ch. 5. In this chapter, we will mostly focus in the ground-state of the two-site Hubbard model, since there the influence of exchange interactions is the most apparent.



Paths without exchange

$$|\uparrow, \downarrow\rangle \rightarrow |0, \uparrow\downarrow\rangle \rightarrow |\uparrow, \downarrow\rangle \quad |\uparrow, \downarrow\rangle \rightarrow |\uparrow\downarrow, 0\rangle \rightarrow |\uparrow, \downarrow\rangle \quad |\downarrow, \uparrow\rangle \rightarrow |0, \uparrow\downarrow\rangle \rightarrow |\downarrow, \uparrow\rangle \quad |\downarrow, \uparrow\rangle \rightarrow |\uparrow\downarrow, 0\rangle \rightarrow |\downarrow, \uparrow\rangle$$

Paths with exchange

$$|\uparrow, \downarrow\rangle \rightarrow |0, \uparrow\downarrow\rangle \rightarrow |\downarrow, \uparrow\rangle \quad |\uparrow, \downarrow\rangle \rightarrow |\uparrow\downarrow, 0\rangle \rightarrow |\downarrow, \uparrow\rangle \quad |\downarrow, \uparrow\rangle \rightarrow |0, \uparrow\downarrow\rangle \rightarrow |\uparrow, \downarrow\rangle \quad |\downarrow, \uparrow\rangle \rightarrow |\uparrow\downarrow, 0\rangle \rightarrow |\uparrow, \downarrow\rangle$$

Figure 3.2.: Sketch of exchange processes in the Mott-insulating regime of a two-site Hubbard model. For strong repulsive interactions ($U/J^t \gg 1$), the tunneling of single particles in a symmetric double-well ($\Delta = 0$) is far off resonant. This is due to the energy difference of U between states with both particles in one well and states with separated atoms. However, two particles in a spin-singlet configuration can still perform higher-order tunneling processes, during which doubly-occupied states are virtually populated. Eight distinct second-order tunneling channels, which either exchange the position of the two particles or not, can be constructed. If they are combined, they lower the energy of the spin singlet by $4J^t{}^2/U$.

pressed. However, the two particles can still exchange their position in a correlated tunneling process, during which states with double occupations are virtually populated (Fig. 3.2). The influence of such correlated tunneling processes on the energy E_s of the spin singlet can be calculated by using second-order perturbation theory [Aue94, Sak85] as

$$\Delta E_s = \langle \psi^{(0)} | H_{\text{eff}} | \psi^{(0)} \rangle = - \langle \psi^{(0)} | H_t \frac{P}{H_{\text{int}}} H_t | \psi^{(0)} \rangle. \quad (3.6)$$

Here, H_{eff} is an effective Hamiltonian that we will identify as the Heisenberg Hamiltonian in Sect. 3.2.2 and $P = |\uparrow\downarrow, 0\rangle \langle \uparrow\downarrow, 0| + |0, \uparrow\downarrow\rangle \langle 0, \uparrow\downarrow|$ is an operator projecting on double-occupied states.

When inserting the spin-singlet wave function (Eq. 3.4) into Eq. 3.6, eight distinct second-order tunneling channels can be identified (see Fig. 3.2), which either exchange the position of the two particles or not. Their combination changes E_s

by

$$\Delta E_s = -J^{ex} = -4 \frac{J^t{}^2}{U}, \quad (3.7)$$

where J^{ex} is called superexchange coupling, or superexchange interaction. Since these effective interactions change the energy of two nearly separated atoms, dependent on their spin state, they can be interpreted as a magnetic interaction. For fermionic atoms and repulsive interactions, superexchange interactions are always positive and therefore reduces the energy of the spin singlet. This leads to a preferential antiparallel alignment of neighboring spins and therefore to an antiferromagnetic ground state [Lie62].

3.2. The Heisenberg model

As we have seen in the last section, an effective Hamiltonian H_{eff} can be defined to explain the energy splitting in the ground-state multiplet of the two-site Hubbard model at large repulsive interactions. This Hamiltonian only acted on the spin state of the particles and therefore allows to reduce the system to a pure spin model. This concept can be directly extended to many-body Hubbard systems, which is the first topic of this section. Afterwards, we will express the effective Hamiltonian H_{eff} within the formalism of a spin model and see that it actually is the Heisenberg Hamiltonian. Finally, we discuss the structure of the ground-state of the Heisenberg Hamiltonian in the case of antiferromagnetic exchange interactions. A compilation of the basic definitions of a spin model can be found in App. A.1.

3.2.1. Emergence of spin models

Extending the two-site model in Eq. 3.3 to many sites and particles leads to the Hubbard Hamiltonian

$$H = - \sum_{\langle i,j \rangle, s} J_{ij}^t (c_{i,s}^\dagger c_{j,s} + c_{j,s}^\dagger c_{i,s}) + \sum_i U_i n_{i,\uparrow} n_{i,\downarrow} + \sum_i \epsilon_i n_i, \quad (3.8)$$

where $\langle i, j \rangle$ denotes neighboring lattice sites, and ϵ_i is a site-dependent energy offset. We limit the discussion to a homogeneous half-filled Hubbard model with $\epsilon_i = 0$, $J_{ij}^t = J^t$, and $U_i = U$ for each site and a mean atom number of one per lattice site (Fig. 3.3)⁵.

⁵An exact definition of the Hubbard parameters can be found in Sect. 3.4.1, where the implementation of Hubbard models in ultracold-atom experiments is discussed.

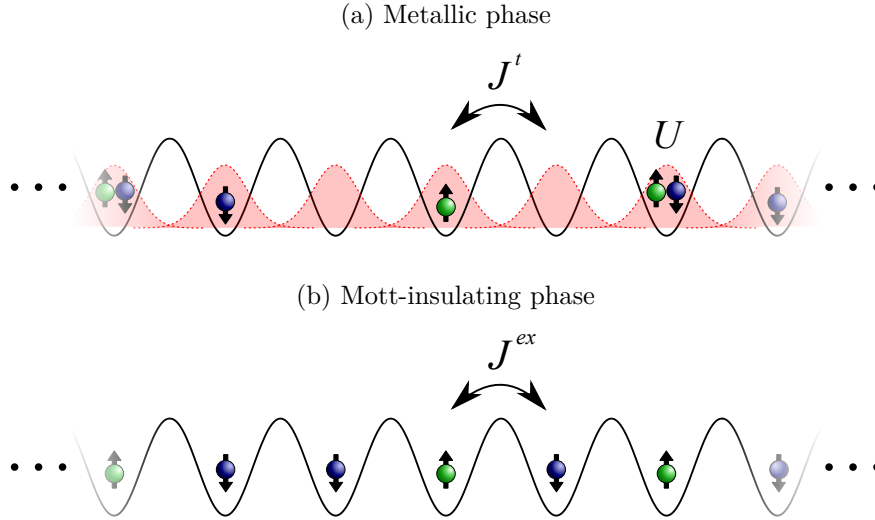


Figure 3.3.: Metal to Mott-insulator transition in the Hubbard model. (a) For weak on-site interaction energies ($U/J^t \ll 1$), single particles tunnel freely through the lattice and form a metallic state. (b) For strong repulsive on-site interactions ($U/J^t \gg 1$), single-particle tunneling in a half-filled Hubbard model is strongly suppressed. For sufficiently low temperatures, the particles form a Mott-insulator with exactly one particle per site. In this limit, the system can be modeled by a pure spin Hamiltonian with magnetic superexchange interactions ($J^{ex} = 4J^{t2}/U$) between neighboring spins.

For weak interactions $U/J^t \ll 1$ the particles tunnel independently through the lattice, and the Hubbard model describes a metallic phase [Fig. 3.3(a)]. In this limit, the motion of particles is only limited by the antisymmetry of the fermionic wave function that prohibits any two particles that are not in a spin-singlet configuration to occupy the same site. When introducing repulsive on-site interactions ($U > 0$), the probability of two atoms occupying the same well decreases. Eventually, the Hubbard system undergoes a transition into a Mott-insulating state, where each well is occupied by exactly one particle [Fig. 3.3(b)]. The critical interaction strength of this transition depends on the dimensionality of the system and the lattice geometry.

For infinite repulsive interactions ($U/J^t = \infty$), any tunneling in the Mott-insulating state is completely suppressed and the ground-state of the Hubbard

system with N_\uparrow spin-up and N_\downarrow spin-down atoms and $N = N_\uparrow + N_\downarrow$ wells is

$$\begin{pmatrix} N_\uparrow + N_\downarrow \\ N_\downarrow \end{pmatrix} \quad (3.9)$$

times degenerate. For each state within this ground-state multiplet, every lattice site is occupied by exactly one particle. In this limit, different states can fully characterized by their spin state. To define a spin model, the particle picture is abandoned completely, and the spin of each particle is directly attributed to the lattice site.

For strong but finite interactions $1 \ll U/J^t \ll \infty$, the degeneracy in the ground-state multiplet is lifted due to correlated tunneling processes between neighboring particles in a spin-singlet configurations. Although density fluctuations are not fully suppressed anymore, the system can approximately still be described as a spin model. The energy splitting between the states is then interpreted as the result of exchange interactions between neighboring spins⁶.

3.2.2. The Heisenberg Hamiltonian

In Sect. 3.1.2, we defined an effective Hamiltonian H_{eff} in a Fock basis, which describes the influence of superexchange interactions on the energy of nearly separated particles. We will now see that H_{eff} is in fact identical to the Heisenberg Hamiltonian, when expressed within a spin basis.

To transform H_{eff} into an Hamiltonian acting on a pure spin basis, one can express the different second-order tunneling paths listed in Fig. 3.2 by spin operators (see Eq. A.1). Considering only the tunneling paths that do not exchange the two particles ($|\uparrow, \downarrow\rangle \rightarrow |\uparrow, \downarrow\rangle$ and $|\downarrow, \uparrow\rangle \rightarrow |\downarrow, \uparrow\rangle$), this results in an effective spin Hamiltonian given by

$$H_{\text{Ising}} = J^{ex} \left(S_L^z S_R^z - \frac{1}{4} n_L n_R \right), \quad (3.10)$$

where S_i^z is the z component of the spin operator \vec{S}_i on site i (Eq. A.1). This is an Ising Hamiltonian that is for instance used to describe the alignment of separated spins interacting via dipole-dipole interactions.⁷

⁶Since superexchange interactions depend on the wave function overlap of the interacting particles, their range is typically very short

⁷The second term on the right-hand side of Eq. 3.10 ensures that the energy of spin triplets is zero. It does not change the overall structure of the energy spectrum and is often neglected.

To express the second-order tunneling paths that exchange the position of the two particles ($|\uparrow, \downarrow\rangle \rightarrow |\downarrow, \uparrow\rangle$ and $|\downarrow, \uparrow\rangle \rightarrow |\uparrow, \downarrow\rangle$), it is convenient to use the raising and lowering operators defined in Eq. A.5. The effective Hamiltonian can then be written as

$$H_{\text{XY}} = J^{ex} \left(\frac{1}{2} (S_L^+ S_R^- + S_L^- S_R^+) \right), \quad (3.11)$$

and is typically called XY Hamiltonian. The origin of this name becomes apparent when using Eq. A.5 to rewrite the XY Hamiltonian as

$$H_{\text{XY}} = J^{ex} (S_L^x S_R^x + S_L^y S_R^y), \quad (3.12)$$

where S_i^x and S_i^y are the x and y-component of the spin operator.

The combination of all eight distinct paths of second-order tunneling (Fig. 3.2) leads to the two-site Heisenberg Hamiltonian

$$\begin{aligned} H &= H_{\text{Ising}} + H_{\text{XY}} \\ &= J^{ex} \left(S_L^x S_R^x + S_L^y S_R^y + S_L^z S_R^z - \frac{1}{4} n_L n_R \right) \\ &= J^{ex} \left(\vec{S}_L \cdot \vec{S}_R - \frac{1}{4} n_L n_R \right). \end{aligned} \quad (3.13)$$

It can be easily expanded to larger spin chains by imposing superexchange interactions J_i^{ex} between any two neighboring spins on lattice sites i and $i + 1$

$$H_{\text{QHM}} = \sum_i J_i^{ex} \left(\vec{S}_i \cdot \vec{S}_{i+1} - \frac{1}{4} n_i n_{i+1} \right). \quad (3.14)$$

Combining all second-order tunneling paths therefore lead to an Hamiltonian that has equal contribution from all three spin components (see second line of Eq. 3.13) and hence contains the SU(2) spin-rotation symmetry.

Symmetries of the Heisenberg Hamiltonian

In order to characterize the eigenstates of the Heisenberg model, we will now discuss the symmetries of H_{QHM} . Both the Ising Hamiltonian and the XY Hamiltonian do not change the z-component $\mathbf{S}^z = \sum_i S_i^z$ of the total spin operator $\vec{\mathbf{S}} = \sum_i \vec{S}_i$ [Par10]⁸. Both H_{Ising} and H_{XY} and also the Heisenberg Hamiltonian H_{QHM} must therefore commute with \mathbf{S}^z . Hence, any eigenstate $|\chi\rangle$ of H_{QHM} is also

⁸The XY Hamiltonian does not change \mathbf{S}^z since it contains equal numbers of raising and lowering operators.

an eigenstate of \mathbf{S}^z with

$$\mathbf{S}^z |\chi\rangle = M |\chi\rangle, \quad (3.15)$$

where M is an integer number between $-N/2$ and $N/2$ and N is the number of spins in the system.

Furthermore, the fact that the Heisenberg Hamiltonian conserves the full spin-rotational symmetry can be exploited. Since H_{QHM} commutes with \mathbf{S}^z it must also commute with the other spin components \mathbf{S}^x and \mathbf{S}^y . As a consequence, H_{QHM} and $\vec{\mathbf{S}}^2 = (\mathbf{S}^x)^2 + (\mathbf{S}^y)^2 + (\mathbf{S}^z)^2$ commute [Par10], which allows to define the total spin quantum number S according to

$$\vec{\mathbf{S}}^2 |\chi\rangle = S(S+1) |\chi\rangle. \quad (3.16)$$

Importantly, S is only a good quantum number for the Heisenberg Hamiltonian and not for either the Ising or the XY model, separately.

3.2.3. Antiferromagnetism

Depending on their sign, magnetic interactions can either be antiferromagnetic (AFM) ($J^{ex} \geq 0$) or ferromagnetic (FM) ($J^{ex} \leq 0$). Thereby, AFM (FM) interactions reduce (increase) the energy of neighboring spins in a singlet configuration (see Sect. 3.1.2) and favor the antiparallel (parallel) alignment of neighboring spins. The ground state of a Heisenberg model with only FM correlations is generally easy to determine, since it contains only spin-triplet correlations between any two spins in the system. In this case, all individual spins are aligned in parallel leading to a total spin quantum number of $S = N/2$.

In contrast, the AFM Heisenberg model typically has a much richer low-temperature phase diagram, which depends not only on the interactions, but also on the dimensionality of the system and the underlying lattice geometry [Aue94, Sac08]. The difficulty of finding the antiferromagnetic ground-state is thereby fundamentally connected to the exchange symmetry of fermions, which prohibits to create completely antisymmetric spin states out of more than two spin-1/2 particles [Sak85]. As a result, the ground state of the AFM Heisenberg model is formed by superpositions of singlet and triplet correlations, which generally makes its description very involved.

Even without knowledge of its exact form, Lieb and Mattis could prove the important result, that the ground state of an AFM Heisenberg model always has the smallest total spin quantum number ($S = |N_{\uparrow} - N_{\downarrow}|$) out of all states [Lie62]⁹.

⁹The theorem requires that the underlying lattice is bipartite, which is true for spin chains, or for simple cubic lattices in higher dimensions.

For equal numbers of spin-up and spin-down particles, the ground state of the AFM Heisenberg model is therefore always a spin singlet with a total spin quantum number of $S = 0$.

Importantly, the state with "perfect" antiparallel alignments of neighboring spins ($|\cdots \uparrow \downarrow \uparrow \cdots\rangle$), which is usually called the Néel state, is not the ground-state of the quantum Heisenberg model. Since any permutation of neighboring spins would destroy its ordering, the Néel state is not even an eigenstate of \vec{S} or of the Heisenberg Hamiltonian (Eq. 3.14). In a homogeneous two or three-dimensional lattice without frustration, the antiferromagnetic ground state of the Heisenberg model can nonetheless have long-range alternating spin order, due to the spontaneous breaking of the spin-rotational symmetry [Aue94, Mat01, Sac08]. However, the "perfect" Néel order will also in these cases be destroyed by quantum fluctuation. In one-dimensional systems, these quantum fluctuations prevent any spontaneous breaking of the spin-rotational symmetry and no phase with long-range alternating spin order exist [Mer66].

3.3. Assembling many-body spin systems

The experiments presented in this thesis, follow the premise of assembling many-body spin systems from small and individually prepared components. When trying to assemble the ground state of an antiferromagnetic Heisenberg Hamiltonian, these components have to fulfill specific requirements.

A first idea could be to start from a product state of individually prepared spin-1/2 particles and combine them by slowly introducing AFM superexchange interactions. However, the lack of correlations between the particles in the initial state will always make their combination non-adiabatic. Even for an initial state prepared in Néel order, this would prohibit the formation of spin order in the final state [Ho08].

This problem does not exist, when starting from individual components that already possess the full spin-rotational symmetry of the final AFM state [Lub11]. The smallest system with a full spin-rotational symmetry is the two-particle spin singlet, for which the spin state can be written as¹⁰

$$|\chi^{(0)}\rangle = \frac{1}{\sqrt{2}} (|\uparrow_L \downarrow_R\rangle - |\downarrow_R \uparrow_L\rangle). \quad (3.17)$$

This spin singlet is the ground state of the two-site AFM Heisenberg Hamiltonian

¹⁰Note that here the state of the spin singlet is given in a spin basis. In Eq. 3.4, the spin singlet was given in a Fock basis instead, which explains the opposite sign.

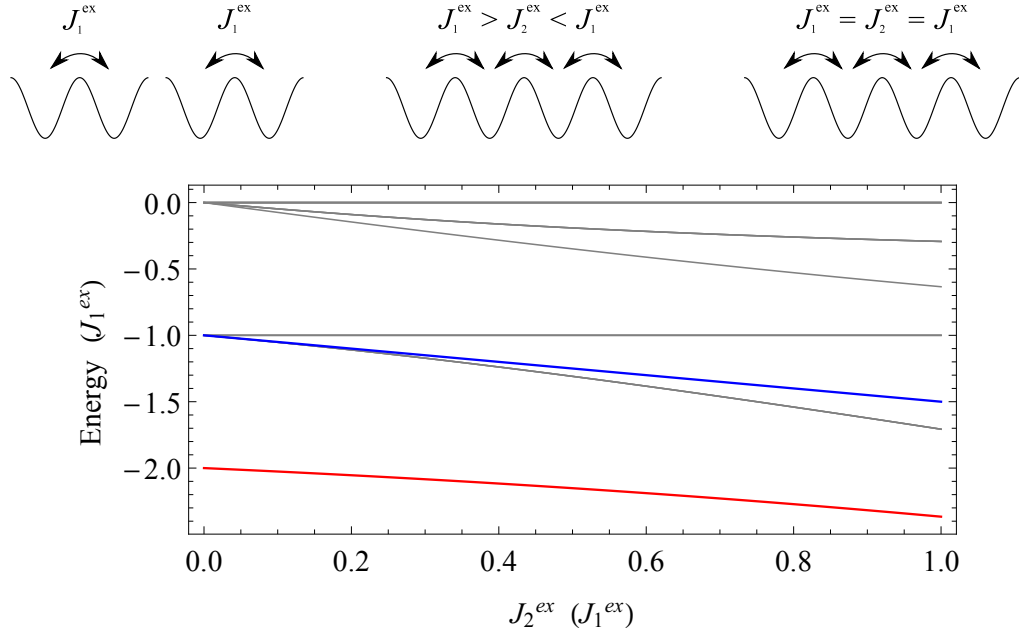


Figure 3.4.: Connecting two separated spin-singlets. The red and gray lines show eigenenergies of the four-site Heisenberg system as a function of the superexchange interaction J_2^{ex} between the two central sites. The energies and J_2^{ex} are both given in units of the superexchange energy J_1^{ex} of the outer links. For $J_2^{ex} = 0$, the system consists of two independent two-site Heisenberg systems. In this limit, the ground state is a product state of two two-particle spin singlets. For $J_2^{ex} = J_1^{ex}$, the homogeneous four-site Heisenberg model is reached. For comparison, the blue line shows a state with perfect Néel order. This is the ground state of the Ising Hamiltonian (Eq. 3.10).

(see Sect. 3.1.2) and as we will discuss in this section, it is a building block for AFM ground states of larger spin systems [Mat01, Sac08, Lub11].

3.3.1. Combination of two spin singlets

The smallest spin system in which the adiabatic connection of spin singlets can be demonstrated is a four-site Heisenberg spin chain. We assume fixed exchange interactions (J_1^{ex}) between the outer sites and a variable exchange interaction (J_2^{ex}) between the two central sites and solve the systems by numerically diagonalizing the corresponding Heisenberg Hamiltonian (Fig. 3.4). For $J_2^{ex} = 0$, the spin chain consists of two separated two-site Heisenberg systems and its ground state is a

product state of two-particle spin singlets in each of these double wells

$$|\Psi_2^{(0,0)}\rangle \otimes |\Psi_2^{(0,0)}\rangle = \frac{1}{2} (|\uparrow\downarrow\uparrow\downarrow\rangle - |\uparrow\downarrow\downarrow\uparrow\rangle - |\downarrow\uparrow\uparrow\downarrow\rangle + |\downarrow\uparrow\downarrow\uparrow\rangle). \quad (3.18)$$

This ground state has an energy of $-2J_1^{ex}$ and a gap of J_1^{ex} to the first excited state, which corresponds to the transformation of one of the spin singlets into a spin triplet. When combining the two-site systems ($J_2^{ex} > 0$), the spin singlets are not localized anymore. At the same time, the ground state energy is further reduced until it reaches a value of about $-2.366 J_1^{ex}$ in the four-site spin chain with equal exchange couplings ($J_1^{ex} = J_2^{ex}$).

Importantly, the four-particle ground state of this system is always nondegenerate for any value of J_2^{ex}/J_1^{ex} between zero and one. Starting from two individually prepared spin singlets, it is therefore theoretically possible to connect the two-site systems with an adiabatic ramp and reach the ground-state of the homogeneous four-site spin chain with arbitrary fidelity [Lub11].

3.3.2. Combining antiferromagnetic spin systems

The adiabatic combination of two two-particle spin singlets is the minimum example for the assembly of antiferromagnetic Heisenberg systems. The concept can directly be extended to larger dimerized spin chains.

For any number of isolated dimers, the ground state of the whole system is given by a product states of two-particle spin singlets in each dimer. Since each of these spin singlets has a spin quantum number of $S = 0$, also the total spin quantum numbers of the whole spin chain will be $S = 0$. In agreement with Lieb-Mattis theorem, the initial ground state is therefore a spin singlet [Lie62]. Again, the excitation energy to the first excited state is given by the superexchange energy (J_1^{ex}) in the individual dimers. This discrete energy gap always ensures the possibility of an adiabatic combination of the dimers [Sac08]. The time t it takes to adiabatically combine the dimers into a homogeneous spin chain thereby scales with $t \propto N^2$, where N is the number of sites in the system [Lub11].

The same ideas can also be applied to two-dimensional dimerized lattices (see Fig. 1.1). However, when combining individual spin singlets into an homogeneous two-dimensional spin system, the ground state undergoes a quantum phase transition [Sac08]. Assuming that the exchange interactions between the dimers have the same size in all directions, a critical value of $J_2^{ex}/J_1^{ex} \approx 0.52$ can be calculated at which the system spontaneously breaks the spin-rotational symmetry and acquires long-range spin order [Mat01, Sac08].

The inverse process of splitting up a many-body spin system into individual

dimers and measuring the fraction of spin-singlets in these dimers was recently used to measure the amount of antiferromagnetic correlations in a system of ultracold atoms [Gre13, Mes15].

3.4. Realization of Heisenberg spin chains

The exact theoretical description of Heisenberg and Hubbard systems is only possible in few limiting cases. These cases include systems of small size, for which the Hamiltonian can still be solved by numerically exact methods [Par10], or one-dimensional systems, for which specific numerical and analytical methods could be developed [Gia04]. However, away from these limits, many fundamental questions about the low-temperature phases of these two fundamental models remain unanswered to this day. Interest in these questions was especially boosted by the observation of high-temperature superconductivity in cuprates with antiferromagnetic interactions, which to this day remains not understood [Bed86, And87, Nor11]. So far, it is still unclear if the Hubbard model suffices to explain this unconventional superconductivity, or if more sophisticated models are needed.

Following the concept of quantum simulation, ultracold-atom experiments were proposed to contribute to the solution of these problems [Fey82, Jak98]. In this approach, the outstanding versatility of atomic systems is supposed to allow the realization of specific quantum many-body Hamiltonians. From the experimental investigation of those atomic system, new input into the theoretical models is expected. The starting point for all experiments with fermionic atoms is thereby given by the Hamiltonian

$$\begin{aligned}
 H = \sum_{s=\{\uparrow,\downarrow\}} \int d^3x \hat{\psi}_s^\dagger(\mathbf{x}) \left(-\frac{\hbar^2 \nabla^2}{2m} + V_0(\mathbf{x}) \right) \hat{\psi}_s(\mathbf{x}) \\
 + g_{3D} \int d^3x \hat{\psi}_\uparrow^\dagger(\mathbf{x}) \hat{\psi}_\downarrow^\dagger(\mathbf{x}) \hat{\psi}_\downarrow(\mathbf{x}) \hat{\psi}_\uparrow(\mathbf{x}),
 \end{aligned}
 \tag{3.19}$$

of an interacting two-component Fermi system in second quantization. Here, $\hat{\psi}_\uparrow$ and $\hat{\psi}_\downarrow$ are the fermionic field operators for atoms in two different hyperfine states, $V_0(\mathbf{x})$ is an external potential and g_{3D} is the coupling constant between two atoms in a spin-singlet configuration (see Eq. 2.15).

In this section, we will discuss two distinct methods for the realization of the Heisenberg Hamiltonian in experiments with ultracold fermionic atoms. In both methods specific external trapping potentials are used (see Sect. 4.3) and the coupling constant g_{3D} between the atoms is adjusted by using a magnetic Feshbach resonance (see Sect. 2.2.3).

In the first method (Sect. 3.4.1), ultracold atoms are trapped in the periodic potential of an optical lattice [Gri00] and used to simulate the Hubbard model [Jak98]. The Heisenberg Hamiltonian can then be realized by bringing the Hubbard system into the Mott-insulating regime (Sect. 3.2) [Dua03]. In Ch. 5 of this thesis, the implementation of this method in our experiment using only two fermionic atoms in a double-well potential is discussed [Mur15a]. For the second method of simulating the Heisenberg Hamiltonian (Sect. 3.4.2), ground-state systems of few fermionic atoms in a strongly-elongated trap are brought into the fermionization regime (Sect. 2.4) [Gir60, Deu08]. The atoms thereby from a spin chain which is stabilized by the strong repulsion between the atoms and the one-dimension trap geometry. The state of this spin chain is determined by a Heisenberg Hamiltonian [Deu14]. This method was first realized in our experiment [Mur15b] and is discussed in Ch. 6.

3.4.1. Realization of the Hubbard model

In order to realize the Hubbard Hamiltonian in an ultracold-atom experiment, the atoms are usually trapped in an optical lattice. Optical lattices are conservative periodic potentials, generated by the standing-wave intensity pattern of interfering laser beams. Many different lattice geometries can be realized, but in their simplest form, optical lattices have a potential given by $V_0(\mathbf{x}) = \sum_{j=1}^3 V_{j,0} \sin^2(kx_j)$. Here, $k = 2\pi/\lambda$ is the wave vector and λ is the wavelength of the trapping light leading to a lattice spacing of $a = \lambda/2$. The lattice depth $V_{j,0}$, can typically be changed separately for each spatial direction by changing the intensity of the corresponding laser beams, which allows the realization of one, two, and three-dimensional optical lattices. Additionally, the trapping potential of an optical lattice usually has a slow overall variation due to the inhomogeneous profile of the trapping beam.

Tight-binding and single-band approximation

The motion of atoms in an optical lattice can be separated into two parts: the vibrations of atoms within the individual wells and their tunneling between different wells. By superimposing vibrational eigenstates of the individual wells that have an equal number n of excitations, energy bands with a width proportional to the tunneling matrix element between wells can be defined. The energy eigenstates of noninteracting atoms that tunnel through the lattice are then given by Bloch states [Ash76]. If tunneling between different sites of the lattice is weak, the system can also be expressed in a real-space basis, by using the Wannier functions. Thereby, each Wannier function $w^n(\mathbf{x} - \mathbf{x}_i)$ is centered at an individual lattice site with position \mathbf{x}_i and is orthogonal to all other Wannier functions. In this limit, the

fermionic field operators of Eq. 3.19 can be expanded within the basis of Wannier functions

$$\hat{\psi}_s(\mathbf{x}) = \sum_{i,n} c_{i,n,s} w^n(\mathbf{x} - \mathbf{x}_i), \quad (3.20)$$

where the operator $c_{i,n,s}$ creates one fermion in spin state s and energy band n in the Wannier state centered at \mathbf{x}_i .

In a sufficiently deep optical lattice, the Wannier functions are strongly localized at the individual wells. In this limit, $w^n(\mathbf{x} - \mathbf{x}_i)$ can be approximated by the n -th vibrational eigenstate on site i with only small additional contributions from the n -th eigenstates on neighboring sites. This is the so-called tight-binding limit, which is an essential prerequisite for the Hubbard model. In this limit, energy attributed to single-particle tunneling between different wells are much smaller than the excitation energy within the wells, which leads to well-separated energy bands. In the following, we will assume that the Fermi edge is within the lowest energy band of the system and therefore only this band is populated ($n = 0$). This so-called single-band approximation is necessary to obtain the standard Hubbard Hamiltonian of Eq. 3.8, but can be omitted in extended Hubbard models.

Definition of the Hubbard parameters

Within the tight-binding approximation, the tunneling of noninteracting particles in an lattice can be written by using Eq. 3.20 to express the first line of the Fermi Hamiltonian (Eq. 3.8) within the Wannier basis

$$\sum_{i,j,s} \int d^3x c_{i,s}^\dagger w^*(\mathbf{x} - \mathbf{x}_i) \left(-\frac{\hbar^2 \nabla^2}{2m} + V_0(\mathbf{x}) \right) c_{j,s} w(\mathbf{x} - \mathbf{x}_j) \quad (3.21)$$

Since the Wannier states in a deep optical lattice decay very rapidly with distance, Eq. 3.21 is well approximated by only considering tunneling between nearest-neighbor sites $\langle i, j \rangle$. By comparing Eq. 3.21 to the tunneling term of the Hubbard model in Eq. 3.8, the tunneling matrix element $J_{i,j}^t$ can be defined as

$$J_{i,j}^t = \int d^3x w^*(\mathbf{x} - \mathbf{x}_i) \left(-\frac{\hbar^2 \nabla^2}{2m} + V_0(\mathbf{x}) \right) w(\mathbf{x} - \mathbf{x}_j) \quad (3.22)$$

When introducing interparticle interactions, the interaction energy in the system can be expressed by writing the second line of Eq. 3.8 within the Wannier basis

$$\begin{aligned} \sum_{i,j,k,l} g_{3D} \int d^3x c_{i,\uparrow}^\dagger w^*(\mathbf{x} - \mathbf{x}_i) c_{j,\downarrow}^\dagger w^*(\mathbf{x} - \mathbf{x}_j) \\ \times c_{k,\downarrow} w(\mathbf{x} - \mathbf{x}_k) c_{l,\uparrow} w(\mathbf{x} - \mathbf{x}_l) \end{aligned} \quad (3.23)$$

Again, the tight-binding approximation can be applied to simplify the Hamiltonian. Approximately, only on-site interactions can be considered, since the density overlap of particles on different lattice sites is vanishingly small. The on-site interaction energy U_i of Eq. 3.8 can then be written as

$$U_i = g_{3D} \int d^3x |w(\mathbf{x} - \mathbf{x}_i)|^4 \quad (3.24)$$

Similarly, the energy offset of particles on site i in a spatially varying lattice can be calculated as $\epsilon_i = \int d^3x V_{\text{ext}}(\mathbf{x}) |w(\mathbf{x} - \mathbf{x}_i)|^2$, where $V_{\text{ext}}(\mathbf{x})$ describes the overall variation of the lattice potential.

Experimental realization

Instead of using an optical lattice in our experiment, we realize periodic potentials of finite size, by generating arrays of partially overlapping microtraps (Sect. 4.3.2) [Zim11, Les15]. Each of these microtraps is realized by the focus of a single Gaussian laser beam [Gri00]. However, the formalism developed in the last section is still valid in our experiment, since also here, the Wannier states are well approximated by the vibrational ground-states in the individual wells. Compared to optical lattices, our method of creating periodic potentials is more versatile, since position and depth of each well can be adjusted. However, this versatility comes with the drawback that the necessary stability of the individual wells is much harder to accomplish. Also, our current setup is limited to two-dimensional arrays of approximately four by four wells.

In Ch. 5, we will describe the simulation of the two-site Hubbard model with two fermionic atoms in a double-well potential. We will show that both the tight-binding and the single-band approximation are fulfilled in our experiment (Sect. 5.1.3) and experimentally calibrate the Hubbard parameters by using tunneling measurements (Sect. 5.2). By preparing eigenstates of the Hubbard model and introducing strong repulsive interactions, we realize the two particle version of a Mott-insulating state and demonstrate the connection between the Hubbard and the Heisenberg Hamiltonian.

3.4.2. Heisenberg spin chains in the fermionization limit

In the special case of an one-dimensional system, Heisenberg spin chains can also be realized in ultracold-atom experiments without an external periodic potential [Deu14, Vol14, Lev15]. This method uses the fact that in the fermionization regime of infinite repulsive coupling constants (see Sect. 2.4), atoms in an one-dimensional system can not pass through each other. Instead, the atoms self-align in a quasi-

periodic chain, much similar to a Wigner crystal of electrons [Mat04a, Mat04b]. Thereby, all states with an equal number of atoms N and an equal number of density excitations n , also have an equal density distribution and energy, independent of their spin state (i.e. Fig. 2.9). For multi-component systems, this leads to the formation of a degenerate ground state at $g_{3D} \rightarrow \infty$ [Gir07, Deu08].

For strong, but finite repulsion, the single-particle wave functions of neighboring atoms start to overlap, and the degeneracy of states with different spin distributions is lifted. The situation can directly be compared to the Mott-insulating regime of the Hubbard model (Sect. 3.2.1), where also quasi-degenerate multiplets of states were found for large repulsive interactions. Again, the state of the system can be approximated by only its spin distribution and the energy splitting between different spin states can be attributed to exchange processes. Since no sites of an external lattice potential exist in the method, the spin state is simply defined by the order of the spins along the atomic chain.

Equivalent to the case of the Hubbard model, an effective Hamiltonian can be calculated by using perturbation theory around the limit of infinite interaction strength [Deu14, Vol14]. Again, this effective Hamiltonian can be identified as a Heisenberg Hamiltonian in the spin basis. We limit the discussion to systems without density excitations ($n = 0$) and write the effective spin Hamiltonian of N fermions as

$$H = \sum_i E_F^{(N)} n_i n_{i+1} + 2 \sum_i J_i^{ex} \left(\vec{S}_i \cdot \vec{S}_{i+1} - \frac{1}{4} n_i n_{i+1} \right), \quad (3.25)$$

Here, the first term adds a constant energy of $E_F^{(N)}$, which is the energy of N noninteracting identical fermions, to all eigenstates and the factor of two in front of the second term has been introduced in order to stay consistent with the notation in Ref. [Mur15b]. The exchange interactions in the limit of $g_{1D} \rightarrow \infty$ can be calculated as

$$J_i^{ex} = \frac{N! \hbar^4}{m^2 g_{1D}} \int dz_1 \cdots dz_N \delta(z_i - z_{i+1}) \theta(z_1, \dots, z_N) \left| \frac{\partial \psi_F}{\partial z_i} \right|^2, \quad (3.26)$$

where the Heaviside step function $\theta(z_1, \dots, z_N)$ is one for $z_1 < \dots < z_N$ and zero for any other permutation of atoms. The function ψ_F is the ground-state wave function of N identical and noninteracting fermions, which can be calculated as the Slater determinant of product states of the N lowest single-particle levels in the system.

Unfortunately, the multi-dimensional integral in Eq. 3.26 can in practice only be solved for small particle numbers. This problem can be circumvented, by ap-

proximating the exact exchange coupling of Eq. 3.26 by

$$J_i^{ex} = \frac{\hbar^4 \pi^2 n_{\text{TF}}^3(\tilde{z}_i)}{3m^2 g_{1\text{D}}}. \quad (3.27)$$

Here, $n_{\text{TF}}(z) = 1/(\pi\hbar) \sqrt{2m(\mu - V(z))}$ denotes the 1D Thomas-Fermi density and \tilde{z}_i is the center-of-mass position of atoms i and $i + 1$ [Deu14, Mar15]. For the special cases of an harmonic trapping potential, which is approximately realized in our experiment (see Ch. 6), an analytical formula that closely approximates the exact exchange couplings was found [Lev15].

Experimental realization

For the discussion of the realization of these Heisenberg spin chains in our experiment (Ch. 6), two important things should be noted. First, the superexchange interactions J_i^{ex} approximately depend on the third power of the local density between the two interacting atoms and therefore on the trapping potential (see Eq. 3.27). As we will see in Ch. 6, changing the potential shape couples different states that have the same total spin quantum number and leads to a new set of eigenstates in the spin chain. Second, the superexchange interactions are proportional to the inverse 1D coupling constant $1/g_{1\text{D}}$. For a large, but finite positive (negative) coupling constant of $g_{1\text{D}}/\sqrt{N} \gg 1$ ($g_{1\text{D}}/\sqrt{N} \ll 1$), the spin chains therefore split up and have an antiferromagnetic (ferromagnetic) ground state.

4. Experimental setup

In this section, we will introduce the experimental techniques that we use to deterministically prepare ground-state systems of few fermionic atoms. Further, we will describe how we can manipulate and detect the state of these systems in order to realize and observe quantum magnetism. We will start this chapter by describing the sequence of events in a typical run of our experiment. This can be seen as an introduction to the experimental techniques and components that will later be discussed in detail.

4.1. The experimental sequence

The measurements described in this thesis all follow a similar experimental sequence that can be divided into four major stages (Fig. 4.1): the collection of atoms in a magneto-optical trap, the generation of a quantum-degenerate Fermi gas, the preparation and manipulation of few-atom systems, and finally the counting of atoms in the system. The course of events of this sequence is completely automated and all devices (like laser shutters, power supplies, voltage-controlled oscillators, and many more) are computer controlled with sub-millisecond time resolution¹. For a measurement run, this sequence is repeated over and over again while only individual parameters are varied in order to isolate their effect on the atomic system. For our measurements on few-atom systems it is often necessary to repeated the sequence thousands of times in order to gain statistically significant results. Therefore, the long-term stability of the experiment will be a recurring theme throughout this chapter.

Stage 1) and 2) Generation of a degenerate Fermi gas: The starting point for the preparation of few-atom systems in our experiment is a quantum-degenerate Fermi gas (DFG) of ⁶Li atoms. We generate the DFG in two successive cooling stages. First, we collect and cool about 10^8 atoms in a magneto-optical

¹For the computer control of our experiment we use a ADwin Pro II from Jäger Messtechnik with 32 digital input/output channels, 16 analog output and 8 analog input channels. Analog channels can be set with 10 μ s time steps, which allows the implementation of real-time PID loops for the active stabilization of experimental parameters. Details on the computer control can be found in Ref. [Lom08].

4.1. The experimental sequence

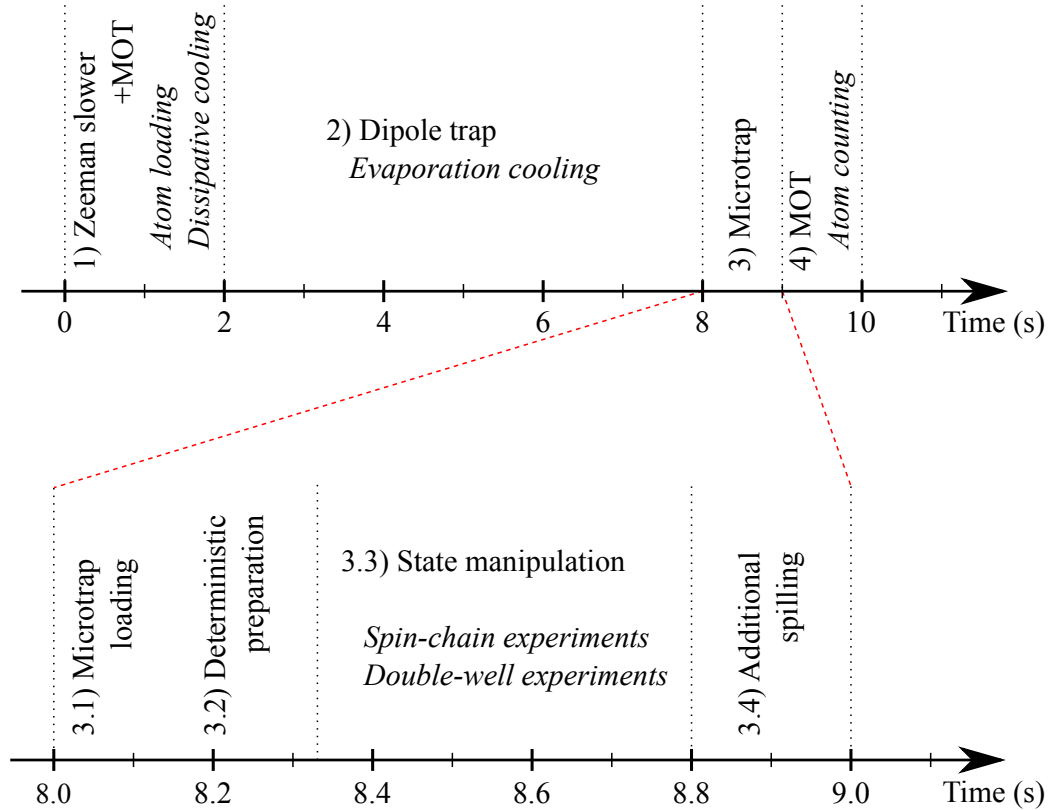


Figure 4.1.: The experimental sequence. In stages 1) and 2) fermionic ${}^6\text{Li}$ atoms are collected and cooled to quantum degeneracy. Stage 3) contains the deterministic preparation and manipulation of ground-state systems of few fermions, which are performed in a small-scale dipole trap, called *microtrap*. All experiments described in Ch. 5 and Ch. 6 are performed in this microtrap during the manipulation stage. In stage 4) the atoms are transferred into a magneto-optical trap (MOT) and counted in order to gain information about their state.

trap (MOT) [Met99]. Since temperatures and densities in the MOT are limited, we then use evaporative cooling in an optical dipole trap (ODT) to reach the quantum-degenerate regime [Met99, Gri00]. These techniques allow us to prepare a DFG of about 10^5 ${}^6\text{Li}$ atoms in a balanced mixture of the two lowest hyperfine states (see Fig. A.1). The atomic samples have a final temperature of $T \lesssim 250$ nK, which corresponds to a degeneracy parameter of $T/T_F \approx 0.5$ in the ODT [Ser11a]. Since the experimental techniques for these initial cooling stages are well-established [Met99, Ket08] and already discussed in several theses of our group [Ser07, Lom08, Ott10, Lom11, Ser11a, Zür12a, Wen13a], we will only shortly

summarize them in Sect. 4.2.

Stage 3) Preparation and manipulation of few-atom systems: To increase the quantum degeneracy of the sample even further, we use yet another ODT, which is created by a single, tightly-focused laser beam (Sect. 4.3) [Gri00]. The main idea behind the use of this small trap, which we will call the *microtrap*, is that it locally increases the Fermi temperature T_F , while the temperature T of the sample approximately stays constant. Using this so-called dimple trick [SK98] we reach a degeneracy of $T/T_F \approx 0.05$, which results in a nearly unity occupation probability on the lowest single-particle levels of the microtrap [Ser11a]. In Sect 4.4, we will describe how we select only the atoms on these lowest trap levels to deterministically prepare ground-state systems of up to ten atoms with a probability above 90 % [Ser11a, Ser11b, Zür12a]. Importantly, this preparation method not only fixes the number of atoms in the trap, but also determines their state. Therefore, also the exchange symmetry of the spin wave function of any two atoms in the sample is determined, which is of great importance for the realization of quantum magnetism in our experiment (see Ch. 5 and Ch. 6).

The actual experiments discussed in this thesis are all performed in one or two microtraps during the state-manipulation stage of the sequence. While the spin-chain experiments (Ch. 6) were performed in a single microtrap (Sect. 4.3.1), which had already been used in previous experiments of our group [Ser11b, Zür12b, Zür13b, Wen13b, Sal13]), the double-well experiments (Ch. 5) were only possible after an upgrade of the experimental apparatus. This upgrade included amongst other things the integration of a new high-resolution objective [Ser11b, Ber13] for the creation of even smaller microtraps and the addition of an acousto-optic deflector (AOD) to the optics setup of the microtrap [Kli12, Ber13]. The AOD allows us to generate multiple partially overlapping microtraps and manipulate their relative height and distance (Sect. 4.3.2).

Stage 4) Atom counting: Finally, after the experiments on the few-atom system have been performed, we count the number of atoms in the system [Ser11a, Ser11b]. In combination with additional state-manipulation techniques the counting of atoms allows us to gather information about the state of the system as discussed in Sect. 4.5.

4.2. Experimental setup and initial cooling stages

4.2.1. The vacuum chamber

A mayor asset of ultracold-atom experiments is the outstanding isolations from the environment that is primarily reached by performing such experiments on clouds

4.2. Experimental setup and initial cooling stages

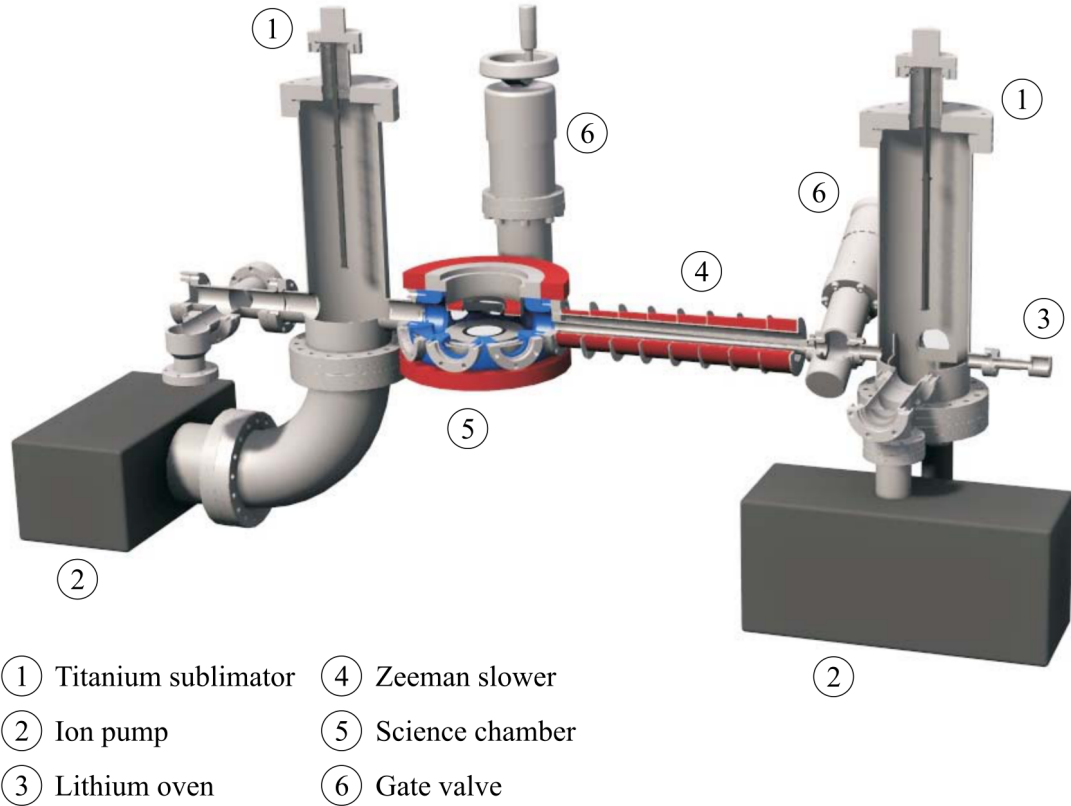


Figure 4.2.: The vacuum system including the magnetic field coils of the Zeeman slower and the MOT. Figure taken from Ref. [Ser07].

of neutral atoms confined in an ultra-high vacuum environment. Fig. 4.2 shows the vacuum chamber of our setup. All experiments are performed in the center of the science chamber (5) and only rely on interactions of the atoms with AC and DC electromagnetic fields. Two titanium sublimator pumps (1), two ion pumps (2) and a non-evaporable getter coating on the walls of the science chamber are used to ensure a pressure on the order of 10^{-12} mbar in the science chamber. To insert ${}^6\text{Li}$ atoms into the vacuum chamber, a solid piece of lithium is placed in a small oven (3) and vaporized by heating the oven to 360°C . At the end of the oven, a collimating aperture forms a beam of hot gaseous atoms that enters the Zeeman slower (4). After being decelerated in the Zeeman slower, the atoms are collected in the center of the science chamber by a MOT. The science chamber has the shape of an octagon with six view ports on the side and two reentrant view ports at the top and the bottom. The view port on the top of the science chamber allows optical access with a numerical aperture of $\text{NA}=0.65$ and is completely covered

by a high-resolution objective used for the creation of the microtrap (not shown in Fig. 4.2). Around the reentrant view ports magnetic field coils that generate a magnetic offset field at the position of the atoms are placed. We will call these coils *Feshbach coils*, since they are used to control the interaction strength between the atoms using a Feshbach resonance (Sect. 2.2.3).

4.2.2. Zeeman slower

After being evaporated, the atoms leave the oven with an average velocity of above 1000 m/s. This is far above the maximum capture velocity of a magneto-optical trap and hence the atoms have to be decelerated before reaching the science chamber. This is achieved in the Zeeman slower by exposing the atoms to a counterpropagating laser beam and an inhomogeneous magnetic field [Met99]. The laser light is red detuned to the optical D_2 transition in ^6Li in order to compensate the Doppler shift of the atoms moving towards the beam. When an atom absorbs a photon from the laser beam its momentum is changed by $\hbar\mathbf{k}$, where \mathbf{k} is the wave vector of the light field. Assuming that the following decay of the atom is spontaneous, and therefore the outgoing photon is scattered in a random direction, the net momentum transfer averaged over many scattering processes is $\hbar\mathbf{k}$. Hence, the motion of the atoms towards the laser light is eventually decelerated, which changes the Doppler-shifted resonance frequency of the atoms. In order to keep the atoms on resonance over a long distance, this change of the Doppler shift is compensated by a position-dependent Zeeman shift created by the inhomogeneous magnetic field.

In our experiment, the Zeeman slower has a length of 40 cm and allows to reduce the longitudinal velocity of the atoms to approximately 60 m/s. The flux of atoms that reach the capture region of the MOT is on the order of 10^{10} atoms/s and about one percent of these atoms is actually trapped [Ser07]. A detailed description and characterization of the Zeeman slower in our experiment can be found in Ref. [Ser07]

4.2.3. Magneto-optical trap (MOT)

In a magneto-optical trap, atoms can be simultaneously cooled and trapped by nearly resonant laser light [Met99]. As in the case of the Zeeman slower, the laser light is slightly red detuned to the atomic transition and is therefore preferentially absorbed by atoms that move towards the beam. If counterpropagating laser beams are applied in all three spatial dimensions, atoms below a certain initial velocity are efficiently cooled. However, without any position-dependent forces, the atoms diffuse and eventually leave the trapping region of this so-called optical

molasses [Met99]. This diffusion can be avoided by adding a linear inhomogeneous magnetic field \mathbf{B} to the system, which has a point with $|\mathbf{B}| = 0$ within the crossing region of the laser beams. For suitable polarizations of the laser beams, the atoms experience a restoring force that traps sufficiently slow atoms in the center of the trap [Met99].

In our experiment, the MOT is realized by two MOT coils in anti-Helmholtz configuration and three retroreflected laser beams that are red detuned to the D2 transition of ${}^6\text{Li}$ by about 6Γ . Here, $\Gamma = 2\pi \times 5.87$ MHz is the natural line width of the D2 transition in ${}^6\text{Li}$. The MOT coils generate a magnetic quadrupole field with a gradient of about 40 G/cm along the central axis. The laser light for both the MOT and the Zeeman slower is generated by a tapered amplifier laser system (TA100, Toptica photonics) and brought to the experimental setup using optical fibers. A detailed description of the laser setup, including the frequency stabilization and partitioning into separate beams can be found in Ref. [Ser07].

In our experiment, we obtain loading rates of about 10^8 atoms/s in the MOT for an oven temperature of 360°C . Since the deterministic preparation of low atom numbers in our experiment is stable for initial atom numbers on the order of 10^7 or larger, we typically load the MOT for about two seconds. Although the MOT is an efficient first stage for the capturing and cooling of atoms, the minimum temperatures and densities that can be reached in a MOT are limited². In our experiment, the atoms in the MOT are cooled to a temperature of about $400\ \mu\text{K}$ and the phase space densities are on the order of 10^{-6} [Ser11a]. However, the regime of quantum degeneracy is reached at phase space densities on the order of one and is therefore still six orders of magnitude away. To achieve this vast increase in phase space density, we transfer the atoms into an optical dipole trap (ODT) and perform evaporative cooling as a second cooling stage.

4.2.4. Evaporative cooling in an optical dipole trap (ODT)

In evaporative cooling, the average temperature of an atomic sample is steadily decreased by removing atoms with above-average energies from the sample. For a gas of atoms in a conservative trapping potential, this can be realized by reducing the depth of the potential and thereby releasing atoms from the high-energy tail of the Boltzmann distribution. At the same time, elastic scattering processes in the gas are needed to rethermalize the atomic sample at any time. The efficiency of evaporative cooling is therefore strongly influenced by the elastic scattering rate between individual atoms.

²The Doppler temperature, which sets the minimum temperature that can be reached in a standard MOT setup, is $140\ \mu\text{K}$ for ${}^6\text{Li}$ atoms.

Although this process reduces the number of atoms in the trap, it increases the phase space density of the remaining atoms and is the standard experimental tool to produce Bose-Einstein condensates or degenerate Fermi gases in ultracold-atom experiments [Ket99, Ket08]. However, to reach ultracold temperatures with fermionic atoms is slightly more involved, since for low enough temperatures a gas of identical fermionic alkali atoms will become non-interacting (see Sect. 2.2), which prevents thermalization. Therefore, evaporative cooling of fermionic atoms requires a second distinguishable type of atoms in the system, which can either be atoms in another hyperfine state, or even atoms of another species [Ket08]. However, also in this case, the collision rate of fermionic atoms is significantly suppressed if the temperature falls below T_F , since then the majority of low-energy states is blocked by the Pauli principle. This prevents efficient thermalization and typically limits the quantum degeneracy after evaporative cooling to $T/T_F \approx 0.5$ [Hol00, McK11].

To realize a conservative trapping potential for evaporative cooling in our experiment, we use an ODT [Gri00]. In such a trap, the potential is generated by a spatially varying light shift in the ground state of the atoms. This light shift ΔE is induced by the interaction between the electric field of the laser light and the induced electric dipole moment of the atoms and can for a sufficiently large detuning be written as

$$\Delta E = \frac{3\pi c^2}{2\omega_{\text{res}}^3} \left(\frac{\Gamma}{\omega_{\text{res}} - \omega} + \frac{\Gamma}{\omega_{\text{res}} + \omega} \right) I. \quad (4.1)$$

Here, ω_{res} is the resonance frequency and Γ is the natural line width of the atomic transition, ω is the frequency of the laser light, and I is the local light intensity. Following this formula, atoms feel a force toward regions of high intensity (low intensity) if $\Delta < 0$ ($\Delta > 0$) and therefore the laser is detuned to the red (blue) of the atomic transition. Although both red and blue-detuned laser light allows the trapping of atoms in specific spatial intensity patterns, dipole traps of red-detuned laser light are more common due to the versatile possibilities of realizing intensity maxima [Gri00].

In an optical dipole trap, the scattering of photons is usually an unwanted process, since it leads to the heating of the atomic sample, or even the direct loss of atoms from the trap. Luckily, the photon scattering rate drops off quadratically with growing detuning, while the light shift only decreases linearly (Eq. 4.1). This allows to ratio the ratio of scattering rate and potential depth by increasing the laser detuning. But, the creation of a sufficiently deep dipole trap then needs a high peak intensity of the trapping light.

Since we directly load atoms from the MOT into an optical dipole trap in our

experiment, we need an ODT that is both deep and has a big trapping volume. The combination of those properties can only be reached with a high laser power. We therefore chose a continuous-wave fiber laser (YLR-200-LP, IPG Photonics) operating at a wavelength of 1070 nm that has a maximum output power of 200 W as laser for our dipole trap. The laser light is far red detuned from all atomic transitions of the ${}^6\text{Li}$ ground state and therefore allows for the trapping of atoms in an intensity maximum. We create this maximum by superimposing the foci of two laser beams under a shallow angle of about 14° , which leads to a cigar-shaped dipole trap with a waist of about $40\ \mu\text{m}$ and an aspect ratio of about 10 [Lom11]. At full laser power, the trap depth is on the order of $k_B \times 3\ \text{mK}$. This allows us to transfer about 10^6 atoms into the ODT, which is approximately 1 % of the atoms in the MOT.

Immediately after this transfer, we ramp the magnetic offset field to 760 G, where the atoms have a positive scattering length of about $4200\ a_0$, and start the evaporation process by reducing the laser power. At the same time, we couple the two energetically lowest hyperfine states with a radio-frequency pulse in order to create a balanced two-component Fermi gas and thereby ensure thermalization. Since for repulsive interactions, scattering between sufficiently cold atoms can lead to the formation of molecular atom pairs [Joc03, Joc04, Lom08], we jump the magnetic offset field to 300 G before the temperature of molecule formation is reached. At 300 G, the sample is attractively interacting with a scattering length of about $-300\ a_0$, which prohibits the production of molecules in a 3D system. After further evaporation at low magnetic field, we eventually end up with a degenerate Fermi gas of approximately 5×10^4 atoms in each of the two lowest hyperfine states with a degeneracy parameter of $T/T_F \lesssim 0.5$ [Ser11a].

4.2.5. The Feshbach coils

To create a magnetic offset field at the position of the atoms and thereby control their interaction strength with a Feshbach resonance, we use a pair of coils that are located around the view ports at the top and bottom of the science chamber. Due to their purpose these coils are called *Feshbach coils*. Details about the design of the Feshbach coils and the exact magnetic field profile can be found in Refs. [Ser07, Lom08]. Both coils consist of 15 windings of $5 \times 1\ \text{mm}$ copper wire that is glued to a water-cooled heat sink using diamond-filled epoxy. Each coil is connected to a separate power supply (SM15-400, Delta Elektronika), which provides a maximum current of 400 A. In their normal operation mode, the coils are close to a Helmholtz configuration in order to generate a homogeneous offset field at the position of the atoms. We actively control the sum and the difference of the currents through the two coils using two current transducers as inputs and thereby stabilize both the

offset value and the gradient of the magnetic field [Ber13]. This setup allows us to generate peak values of the magnetic offset field of up to 1450 G. To generate large magnetic field gradients, we can reverse the current through one of the Feshbach coils and thereby create an anti-Helmholtz configuration. In the detection stage of our experimental sequence, we use this to create magnetic field gradients of up to 250 G/cm and thereby compress the volume of the magneto-optical trap (Sect. 4.5).

4.3. Optical dipole traps for the realization of quantum magnetism

Optical dipole traps play an essential role in the simulation of Hubbard physics and quantum magnetism in ultracold-atom experiments [Jak05, Blo08b, Ess10]. Mostly they are used in the form of optical lattices, which are generated by the standing-wave intensity pattern of counterpropagating laser beams and typically consist of a few hundred lattice sites per spatial dimension [Gri00]. However, for the few-atom experiments described in this thesis other trap geometries are more favorable. For the realization of Heisenberg spin chains (Ch. 6), we trap the atoms in the focus of a single far-red-detuned Gaussian beam (Sect. 4.3.1) [Gri00]. The resulting potential of this so-called *microtrap* is cylindrically symmetric and strongly elongated along the axial direction [Fig. 4.3(a)]. This geometry will allow us to prepare few-atom systems in the radial ground state of the microtrap and thereby realize quasi-1D systems. For the simulation of two-site Hubbard physics (Ch. 5), a double-well potential is realized by two partially overlapping microtraps [Fig. 4.3(b)]. In Sect. 4.3.2, we will discuss our setup for the generation of multiple microtraps, which was implemented during the course of this thesis.

4.3.1. The microtrap: Realization of quasi-1D systems

Potential shape of a microtrap

The focus of a single far-red-detuned Gaussian laser beam can be seen as the conceptually simplest realization of an ODT [Gri00]. The spatial intensity distribution of such a beam, which according to Eq. 4.1 is proportional to the potential for ground-state atoms, is given by

$$I(\rho, z) = \frac{2P}{\pi w^2(z)} \exp\left(-2\frac{\rho^2}{w^2(z)}\right). \quad (4.2)$$

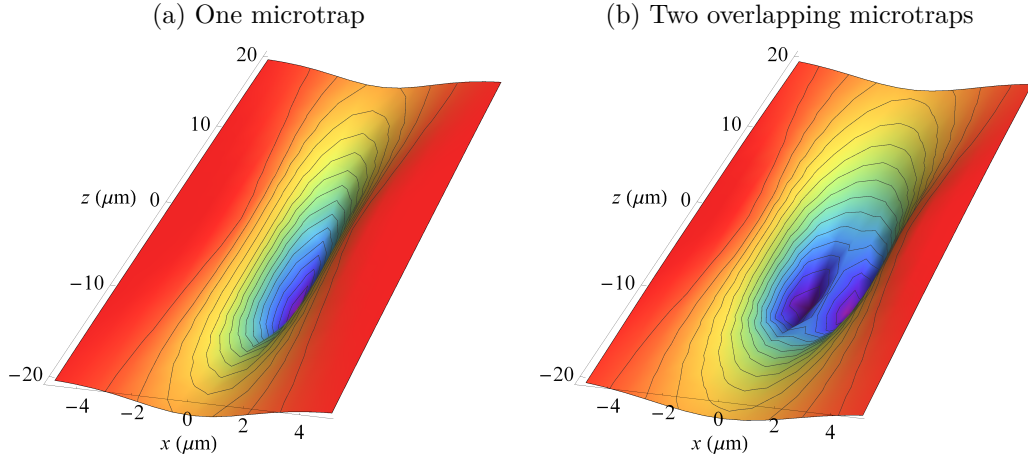


Figure 4.3.: Potential shape of a single microtrap (a) or of two partially overlapping microtraps (b) forming a double well. The individual traps have an aspect ratio of $\eta \approx 7$. They are created by Gaussian beams propagating in z -direction and focused to a waist of $1.6 \mu\text{m}$. The two foci in (b) are placed at a distance of $2 \mu\text{m}$.

Here, z is the propagation direction of the beam, ρ denotes the radial coordinate and P is the light power in the beam. The $1/e^2$ radius $w(z)$ can be calculated as

$$w(z) = w_0 \sqrt{1 + \left(\frac{z}{z_R}\right)^2}, \quad (4.3)$$

where the beam waist w_0 is given by the radius at the position of the focus ($z = 0$) and the Rayleigh range is defined as $z_R = \pi w_0^2 / \lambda$ [Gri00]. The trap depth V_0 for ground-state atoms in this potential is given by the light shift at the position of the maximum intensity ($z = 0, r = 0$) and can be calculated as

$$V_0 = \frac{3Pc^2}{\omega_{\text{res}}^3 w_0^2} \left(\frac{\Gamma}{\omega_{\text{res}} - \omega} + \frac{\Gamma}{\omega_{\text{res}} + \omega} \right), \quad (4.4)$$

using Eqs. 4.1, 4.2, and 4.3.

Close to the potential minimum, the trap can be approximated by a cylindrically symmetric harmonic potential (Eq. 2.18). In this approximation, the axial and radial trapping frequencies are given by $\omega_{\parallel} = (2V_0/mz_R^2)^{1/2}$ and $\omega_{\perp} = (4V_0/mw_0^2)^{1/2}$ [Gri00], which results in an aspect ratio (see Eq. 2.19) of the micro-

trap of

$$\eta = \frac{\sqrt{2\pi}w_0}{\lambda}. \quad (4.5)$$

The smallest value that can be reached for both the focal waist w_0 and the aspect ratio η depends on the numerical aperture of the focusing objective. Also, the ratio $T = w_{\text{ap}}/r_{\text{ap}}$ between the Gaussian beam waist w_{ap} at the entrance aperture of the objective and the radius of this aperture r_{ap} influences these values [Ser11b]. For $T \gg 1$ both w_0 and η are minimized, but the intensity pattern in the focal plane is not Gaussian anymore and instead given by an Airy function. In our experiment, the ratio T is about 0.8, which sets theoretical lower limits of $w_0 \approx 0.47 \lambda/\text{NA}$ and $\eta \approx 2.1/\text{NA}$ on the focal waist and the aspect ratio³.

Determination of trap parameters

To calibrate the trap parameters in our experiment, we measure the trap frequencies ω_{\parallel} and ω_{\perp} using trap-modulation spectroscopy. For these measurements two atoms are prepared in the ground state of the microtrap, as described in Sect. 4.4. Then, the potential is modulated either in depth or in position. If the modulation frequency is equal to the trap frequency (for position modulation) or twice the trap frequency (for depth modulation) atoms are transferred into excited states, which can be measured as a depletion of the ground state (see Sect. 4.5). Other trap parameters, like the aspect ratio and the trap depth, are calculated from the measured trap frequencies. A detailed description of this calibration can be found in Ref. [Zür12a]. All measured and calculated trap parameters can be found in App. A.4.

Although the formulas derived in the last section theoretically allow the determination of all trap parameters from ab-initio calculations, these calculations are typically inaccurate. The main reasons for this inaccuracy are wavefront errors and imaging aberrations that influence the trap geometry. Although all optical elements in the beam path of the trapping light have been aligned interferometrically [Ber13], these aberrations are unavoidable, for example due to the finite aperture and quality of the optical components. Since the trap parameters measured by modulation spectroscopy indicate a larger focal waist than we expected from test measurements of the focusing objective, we conclude that the vacuum viewports of the vacuum chamber are a major source of wavefront errors in our experiment [Ber13].

³The diffraction limited numerical apertures of the two objectives used for the experiments presented in this thesis can be found in App. A.4.

Implementation of a high-resolution objective

The wish of performing experiments in a microtrap with a small waist and aspect ratio lead to the design of a custom-made objective with a nominal numerical aperture of 0.6 in our group that is described in detail in the PhD thesis of Friedhelm Serwane [Ser11a]. This objective was tested and aligned as part of the Masters theses of Vincent Klinkhamer [Kli12] and Andrea Bergschneider [Ber13] and implemented in the experimental setup during an extensive upgrade of our experiment. As a result, the experiments described in Ch. 5 and Ch. 6 are performed in different microtraps. A list of the design parameters of both the old and the new focusing objective and the corresponding trap parameters can be found in App. A.4.

4.3.2. Two microtraps: Realization of a double-well potential

After working with a single microtrap for several years [Ser11a, Ser11b, Zür12a, Zür12b, Zür13b, Wen13a, Wen13b], we upgraded our experimental setup in early 2013 in order to generate finite-size periodic potentials realized by arrays of overlapping microtraps [Zim11, Les15]. The first measurements performed in the upgraded setup are the experiments on double-well systems, which are presented in Ch. 5. In this section we will explain how the double-well potential consisting of two overlapping microtraps is generated and how the potential shape can be changed.

Optical setup and acousto-optic deflector

Our optical setup for the generation of two partially overlapping microtraps is shown in Fig. 4.4. Its main purpose is the generation and shaping of two trapping beams and the stabilization of the overall light power. The infrared trapping light (1064 nm) is provided by a single-mode solid-state laser (Mephisto NE, Innolight) with relative intensity noise of $RIN < 130$ dB/Hz in the relevant frequency range below 100 kHz [Nei13]. The power of the trapping light is actively stabilized using the signal of a photo diode (blue section in Fig. 4.4) on which 50 % of the trapping light is focused. Details on the power stabilization [Ser11a, Zür12a] and the adjustment of the optical setup [Kli12, Ber13] have been discussed in previous theses.

The centerpiece of the new optical setup is a two-axis acousto-optic deflector (A2D-404AH4, IntraAction Corp.), which we use to split the trapping light into two partially overlapping beams. In the acousto-optic deflector (AOD), the light passes through a crystal and is deflected proportionally to the frequency of a radio-frequency (RF) signal applied at the crystal. The efficiency of the deflection and

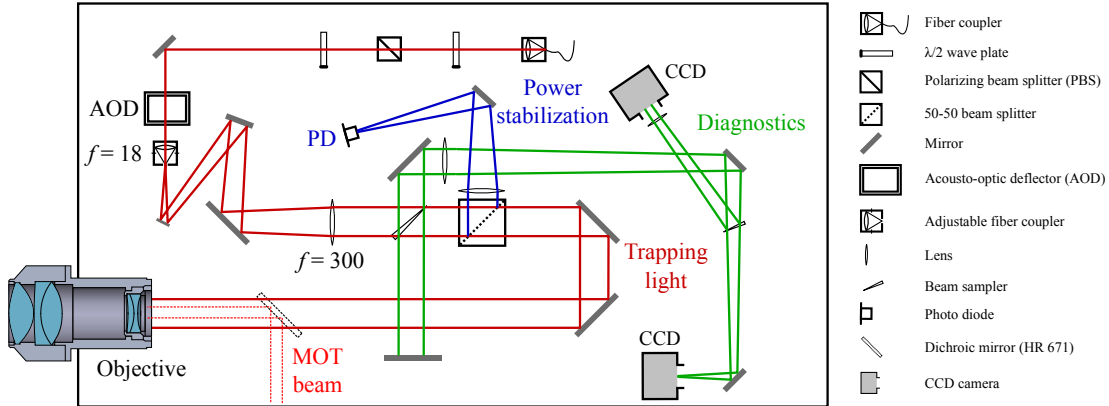


Figure 4.4.: Optical setup for the generation of one or multiple microtraps. The infrared light enters the experimental setup through an optical fiber (top right) and is collimated with a $1/e^2$ diameter of (1.23 ± 0.02) mm. In the AOD the light is deflected according to the power and frequency of one or multiple RF signals applied at the AOD. For the double-well experiments, we apply two RF signals with frequencies of 32 MHz and 38 MHz, which leads to two partially overlapping light beams. After the AOD, we block all light except for the first diffraction order of the AOD and use two lenses that form a telescope to increase the size of the beams to about 19.9 mm. In a non-polarizing 50 – 50 beam splitter half of the light is deflected and focused on a photo diode. This signal is used as input for an active stabilization of the overall light power in both trapping beams [Ser11b, Zür12a]. The light which passes through the beam splitter is redirected on the high-resolution objective (see App. A.4 for the design parameters of the objective) and focused into the experimental chamber. Using the diagnostics setup (green), a Michelson interferometer can be realized that enables us to interferometrically align the objective in order to minimize wave front errors on the laser beam [Ber13]. To load atoms from the microtrap into the MOT (see Sect. 4.5), a beam of red light (671 nm) is superimposed with the infrared light on a dichroic mirror (bottom left). More details on the optical setup can be found in Refs. [Kli12, Ber13].

therefore the power of the deflected light beam depends on the power and the frequency of the RF signal. The diffraction efficiency of our AOD has a maximum at a frequency of about 28 MHz and stays above 50 % of its maximum value between about 25 MHz and 45 MHz [Kli12]⁴.

⁴Unfortunately, the diffraction efficiency of the AOD shows additional fast modulations when the RF frequency is changed, which have a periodicity of about 30 kHz and a relative height of $\lesssim 5\%$ [Kli12]. We assume that these modulation result from reflections of the RF signal within the AOD. However, since we will only work with fixed RF frequencies in our

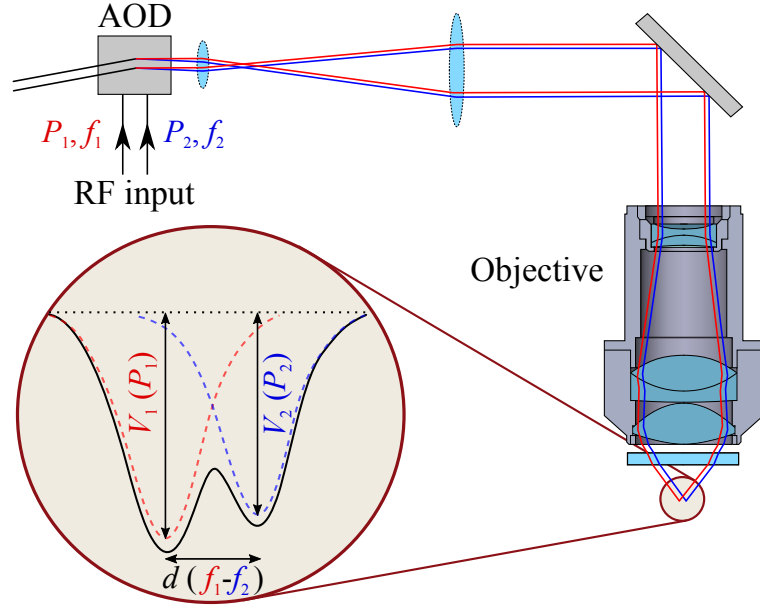


Figure 4.5.: Creation of a double-well potential. The trapping beam is split in an AOD by applying two RF signals with different frequencies f_1 and f_2 . The beams are focused into the experimental chamber by a high-resolution objective. The small differential angle between the beams, which depends on the frequency difference of f_1 and f_2 , leads to a shift d between the positions of the foci. The relative power in the two beams, which depends on the relative power of the RF signals, determines the relative depth of the wells.

We apply two RF signals at the same axes of the AOD (see next section for the discussion of the RF setup) and block all light except for the first diffraction order after the AOD (Fig. 4.5). For a difference Δf of the frequencies of the RF signals the two first-order beams have a small differential angle, which is translated by the objective into a position difference of $d \approx 330 \text{ nm/MHz} \times \Delta f$ of the respective foci. If the frequency difference is small enough to create partially overlapping beams, a double-well potential can be realized in the focal plane. By changing the relative RF power of the two signals, the relative light power in the two beams can be changed, which modifies the relative depth of the two wells. Additionally, by changing the overall light power in both trapping beams, the absolute depth of the two wells and therefore effectively the height of the potential barrier between the wells can be adjusted.

For the experiments described in Ch. 5, we used RF frequencies of $f_1 = 32 \text{ MHz}$

experiments on a double well, we are not effected by these modulations.

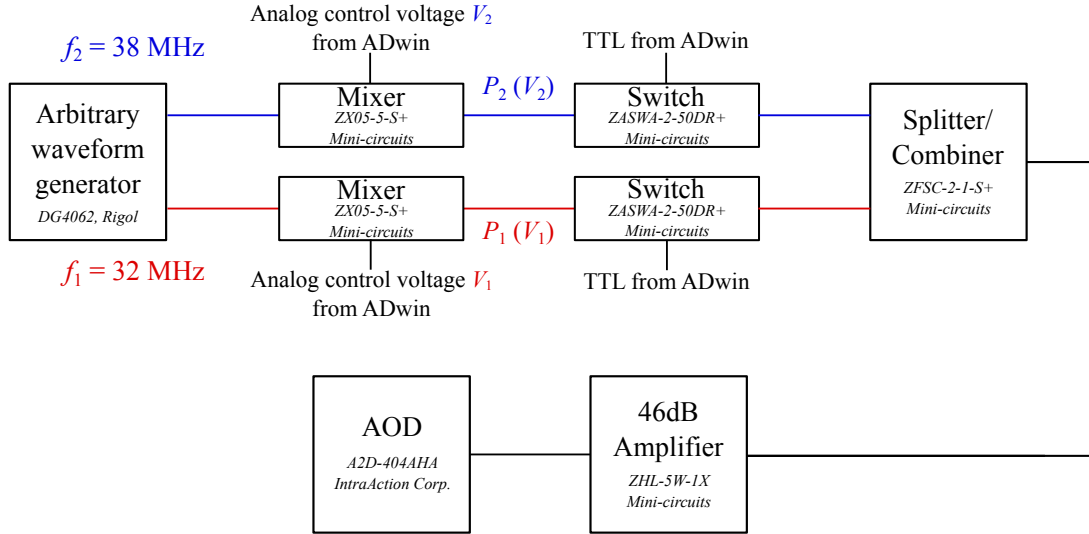


Figure 4.6.: RF setup for the generation of a double-well potential. We use a two-channel arbitrary waveform generator as stable frequency source to generate two sinusoidal signals with frequencies of $f_1 = 32$ MHz and $f_2 = 38$ MHz and constant power. The power of each RF signal is reduced in a controlled way by mixing it with a DC voltage (V_1 and V_2). Both voltages can be set in the experimental control and are provided by the ADwin. Additionally, each RF signal can be quickly turned on and off with a power switch. Finally, the two signals are combined, amplified and applied at the AOD.

and $f_2 = 38$ MHz. We chose these values since the frequency difference of 6 MHz corresponds to a distance of about $2 \mu\text{m}$ between the two wells of the double-well potential. This distance leads to experimentally accessible oscillation frequencies for atoms tunneling between the wells, which are on the order of 100 Hz at typical light powers of about $150 \mu\text{W}$ (see Fig. 5.3).

Radio-frequency setup

In order to observe tunneling oscillations between two wells over multiple periods, both the distance of the wells and their relative depth must be stable. Therefore, one of the main concerns in implementing the setup that generates the RF signals driving the AOD was to achieve an adequate level of stability. In Fig. 4.6, a sketch of the final RF setup, which fulfills these requirements and allowed us to perform the tunneling measurements presented in Ch. 5, is shown.

Since tunneling is extremely sensitive to the distance of the two microtraps, the frequency stability of the RF signals is of major importance. We achieve the

necessary stability by using an two-channel arbitrary waveform generator, which provides a frequency accuracy 2 ppm⁵. We set the output power on both channels of the arbitrary waveform generator to a constant value and control the strength of the RF signals by adjusting the control voltage on the mixers shown in Fig. 4.6. Subsequently the RF signals are combined, amplified, and fed into the AOD.

Stability of the double-well potential

As shown in Ch. 5, we can use the tunneling dynamics of atoms between the ground states of the two microtraps as a probe for the potential shape. This allows us to precisely determine the relative power of the two RF signals that generates a balanced double-well (see Sect. 5.2.3). We also estimate the amount of fluctuations in the relative depth of the two wells using this technique. It turns out that the main source of fluctuations are temperature-dependent drifts of the diffraction efficiency of the AOD. These drifts are unavoidable, since we initially prepare the atoms in only one microtrap and switching on the RF signal of the second microtrap leads to heating of the AOD. This results in drifts of the relative trap depth of approximately 300 Hz over several seconds. Since tunneling frequencies between the traps are on the order of 100 Hz in our experiment, these drifts would strongly limit the visibility of tunneling oscillations. Fortunately, the drifts are reproducible in each experimental cycle and we can measure them using the atoms as a probe. We compensate the drifts in the diffraction efficiency by applying an exponential ramp to the relative power of the two RF signals. Using this technique, the stability of our double-well potential is currently limited by slow drifts in the relative depth of the two microtraps which are on the order of about 10 Herz per day.

4.4. Deterministic preparation of few-atom systems

The basis for all experiments described in the next chapters are deterministically prepared ground-state samples of atoms in a single microtrap. We will now explain how we prepare these samples, starting from a quantum-degenerate Fermi gas of about 10^5 ^6Li atoms in a large ODT (Sect. 4.2.4). The preparation technique described in this section was developed in our group and published in Ref. [Ser11b]. We will first discuss the general idea of our preparation scheme, before explaining details of its experimental realization⁶.

⁵In a first version of the setup, voltage controlled oscillators (ZOS-50+, Mini-curcuits) have proven to be insufficient in frequency stability despite the usage of a stabilized control voltage.

⁶The experimental parameters listed in this section are for the current microtrap setup and slightly differ from the parameters used for the experiments in Ch. 6. Further details on the

4.4.1. Preparation scheme

The goal of the preparation scheme realized in our experiment is to prepare ground-state systems of up to about 10 atoms with a fidelity in the order of 90 % [Ser11b, Ser11a, Zür12a, Zür12b]. We achieve this goal by removing all atoms from a quantum-degenerate Fermi gas, except for the atoms on the few energetically lowest trap levels. According to the Fermi-Dirac statistics, these levels have an occupation probability of nearly one for a sufficiently low degeneracy parameter T/T_F . Therefore, the number of atoms in the system can be precisely determined by controlling the number of trap levels in the system.

However, the quantum degeneracy of $T/T_F \approx 0.5$ that we reach after evaporative cooling in the large ODT, only results in an occupation probability of about 88 % per spin state on the lowest trap levels. Additionally, the trap frequency in the large ODT is much too small to experimentally separate different trap levels. We overcome this problem by using the large ODT as a reservoir and superimpose it with a tightly-focused microtrap to create a dimple in the potential (Fig. 4.7) [SK98, Ser11a]. Since the number of atoms that fit into the microtrap is small compared to the number of atoms in the reservoir, the temperature of the whole sample is not significantly influenced by this process. At the same time, the depth of the microtrap in our experiment is approximately a factor of ten larger than the depth of the reservoir. Therefore, the Fermi temperature of atoms in the microtrap is ten times larger than before and the degeneracy parameter is reduced to $T/T_F \approx 0.05$. Selecting only the atoms on the few lowest microtrap levels now leads to a theoretical limit above 99.99 % for the probability of preparing up to 10 atoms.

4.4.2. Experimental realization of the deterministic preparation

In order to experimentally realize the preparation scheme described in the last section, we start by slowly ramping on the microtrap, which is overlapped with the large ODT. This ramp is slow enough to avoid significant heating [Zür12a]. During the ramp, the magnetic offset field is at 300 G, corresponding to a scattering length of $-300 a_0$, in order to sustain thermalization in the sample. At its final value, the power in the microtrap is about $P = 400 \mu\text{W}$, which leads to a trap depth of about $k_B \times 4.85 \mu\text{K}$. We ramp the magnetic offset field to the zero-crossing of the scattering length at 527 G and switch off the reservoir. At this point, the microtrap contains about 1000 atoms.

experimental parameters for the preparation of few-atom systems in the old microtrap can be found in Refs. [Ser11a, Ser11b, Zür12a].

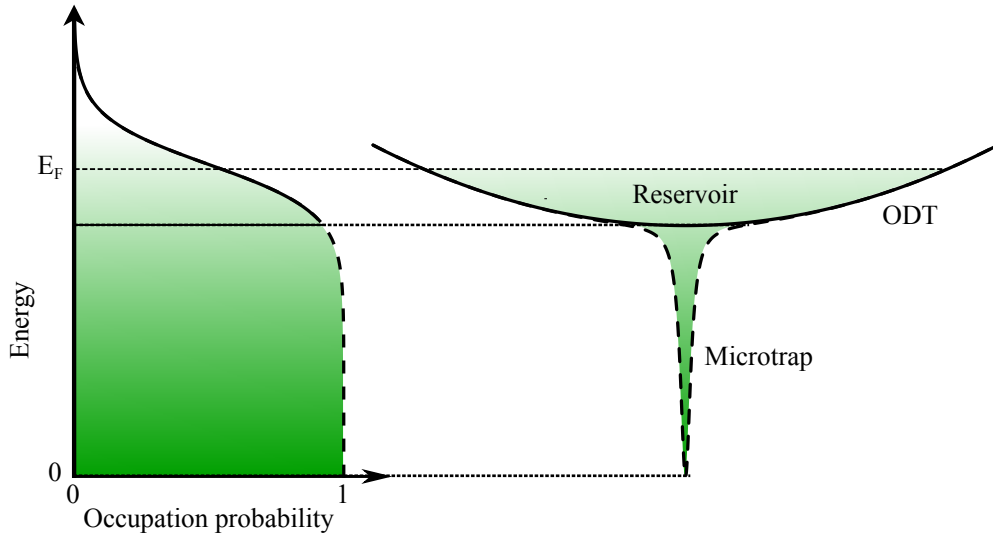


Figure 4.7.: Optical potential for the creation of highly-degenerate Fermi gases (right) and resulting Fermi-Dirac distribution (left). Initially, the Fermi gas is only in a large ODT, which acts as a reservoir. A microtrap is superimposed with the ODT to create a dimple in the potential. As a result, the Fermi temperature $T_F = E_F/k_B$ locally increased at the position of the microtrap and therefore the degeneracy parameter T/T_F locally decreases [SK98]. As indicated by the Fermi-Dirac distribution (left), the occupation probability for atoms on the lowest microtrap levels is almost one.

To spill atoms from excited states of the microtrap, we tilt the trap by applying a magnetic field gradient along its axial direction (Fig. 4.8) until approximately 20 atoms remain. Since at 527 G, the ^6Li atoms are well within the Paschen-Back regime, the gradient has approximately the same effect on atoms in both of the two lowest hyperfine states (see Fig. A.3). The combined optical (see Eq. 4.2) and magnetic potential can be written as

$$V(z) = V_{\text{optical}}(z) + V_{\text{magnetic}}(z) = pV_0 \left(1 - \frac{1}{1 + (z/z_R)^2} \right) - \mu_m B' z, \quad (4.6)$$

where $V_0 = k_B \times 4.85 \mu\text{K}$ is the initial depth of the optical potential at a light power of $(390 \pm 39) \mu\text{W}$, p is the trap depth parameter, μ_m is the magnetic moment of the atoms, and $B' = 30 \text{ G/cm}$ is the strength of the magnetic field gradient⁷. As shown in Fig 4.8(b), the combined potential has a barrier, which separates the

⁷Further trap parameters are listed in the Tab. A.4

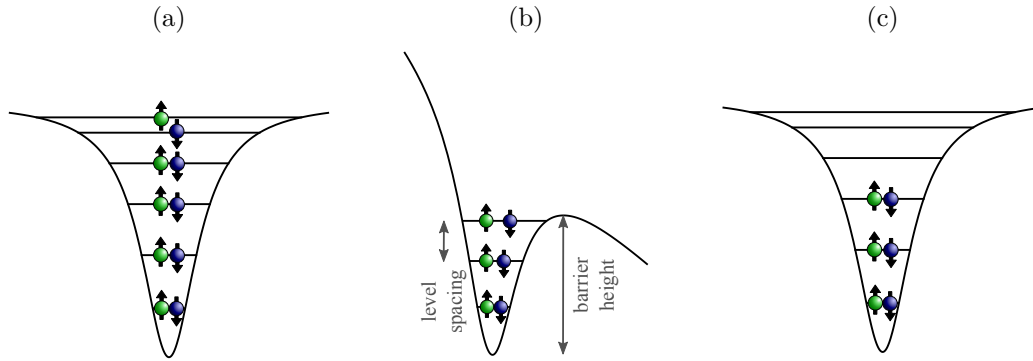


Figure 4.8.: The spilling process. (a) We start with a two-component sample of about 1000 quantum-degenerate atoms ($T/T_F \approx 0.05$) in the microtrap. (b) We apply a magnetic field gradient and thereby tilt the potential of the microtrap and spill atoms from the trap. By reducing the light power in the microtrap, we fine-tune the height of the potential barrier that separates the in-trap states from the continuum of states outside of the trap. Atoms now leave the trap with a rate that strongly depends on their energy. (c) After restoring the original trapping potential, a well-defined number of atoms is left in the trap.

energetically lowest in-trap states from the continuum of states outside of the trap. Since the magnetic field gradient needs too long to reach its steady state after a ramp (on the order of 10 ms), we perform the last part of the spilling process by lowering the optical trap depth to approximately $0.5 V_0$. This effectively lowers the potential barrier and thereby reduces the number of trap levels. Atoms with energies above or marginally below the potential barrier now leave the trap, while atoms with significantly lower energies remain. After 25 ms, we restore the original microtrap geometry, by ramping the optical trap depth back to V_0 and switching off the magnetic field gradient [Fig. 4.8(c)].

In Fig. 4.9, the number of atoms in the microtrap (see Sect. 4.5.1) is plotted as a function of the trap depth parameter p during the spilling process. The plot shows broad plateaus for even atom numbers. From the center position of these plateaus, we identify the trap depth parameters p_N for the deterministic preparation of N atoms. After a preparation with $p = p_N$, each of the $N/2$ energetically lowest trap levels is populated by two atoms in different hyperfine states. As shown by the variance on the right side of Fig. 4.9, the atom-number fluctuations are strongly suppressed for preparations with p_N .

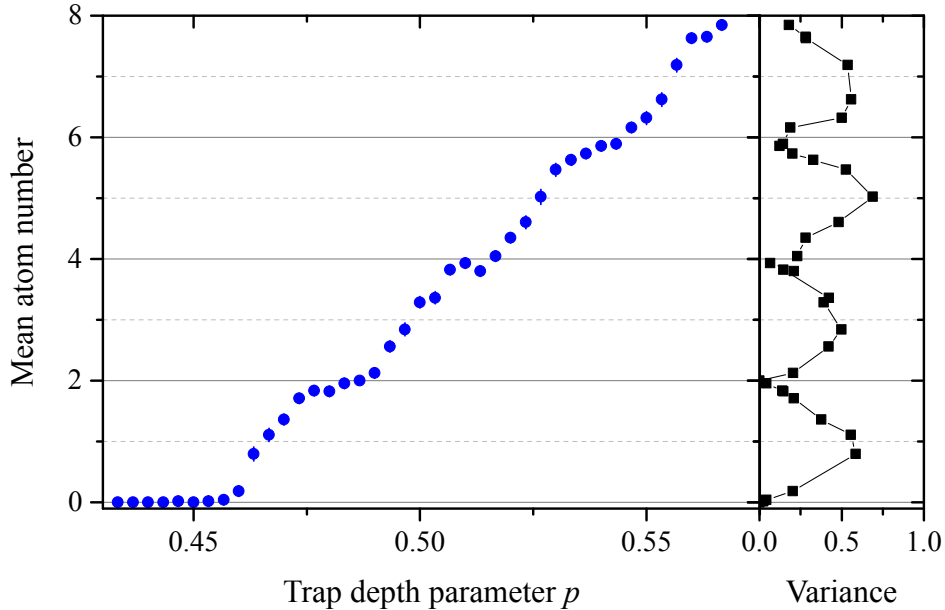


Figure 4.9.: Mean atom number and atom-number fluctuations after the spilling process. (left side) By changing the optical trap depth p during the spilling process, the number of atoms that remain in the trap can be selected. Each shot is the average of about 50 individual measurements. (right side) The fluctuations of the atom number show a clear suppression at even atom numbers. At these values all trap levels below a certain energy are populated with two atoms each, while all atoms from energetically higher levels have been removed from the trap. For six atoms a variance of $\sigma^2 = 0.12$ is measured, which corresponds to a suppression of $\sigma^2 / \langle N \rangle = 0.02 = 17$ dB compared to a system obeying Poissonian statistics. The single-particle preparation fidelity, which was extracted from the probabilities of preparing two, four, or six atoms with minimum atom-number fluctuations, is (97.8 ± 0.6) %.

4.4.3. Deterministic preparation of a spin-1/2 system

Throughout this thesis, we use the two lowest hyperfine states of ${}^6\text{Li}$ to realize an effective spin-1/2 system. We define spin-up and spin-down states as $|\uparrow\rangle = |m_S = -1/2, m_I = 0\rangle$ and $|\downarrow\rangle = |m_S = -1/2, m_I = 1\rangle$ (see Fig. A.1). Importantly, the preparation scheme described in the last section also determines the two-particle spin correlations in the system. This is remarkable, since without interactions between spin-up and spin-down atoms, the deterministic preparation for both components seems independent of each other. But, as we will discuss in this section, the preparation of two-component ground-state systems together with

the intrinsic antisymmetry of the fermionic wave function leads to the emergence of simple rules for spin correlations.

Let us assume that the preparation lead to a noninteracting spin-balanced sample of N fermions, which is in the many-particle ground state of the microtrap. Due to Fermi-Dirac statistics, the atoms have to occupy the $N/2$ energetically lowest trap levels with one spin-up and one spin-down atom each. Since the total wave function of two atoms with the same orbital wave function can only be antisymmetrized by an antisymmetric spin wave function, two atoms on the same single-particle trap level are always in a spin-singlet configuration. The N atoms therefore form $N/2$ spin singlets, which are uncorrelated from each other and can only be distinguished by the excitation of their center-of-mass motion. The combination of $N/2$ spin-singlets with a spin quantum number of $S = 0$ each necessarily leads to a total spin quantum number of $S = 0$ of the N -particle system.

When introducing interactions in this system, the single-particle trap levels are not eigenstates of the atoms anymore. Therefore, the spin-singlet correlations can no longer be attributed to fixed pairs of atoms, but are instead shared by all atoms in the system. Still, the total spin quantum number of $S = 0$ is conserved⁸, which is of major importance for the realization of quantum magnetism as discussed in the next chapters.

Preparation of spin-imbalanced samples

To prepare spin-imbalanced ground-state systems, we first prepare a spin-balanced system and then remove a particular number of spin-down atoms in a second spilling process. To do this, we change the magnetic offset field to 27 G, which is in the crossover region between the Zeeman and the Paschen-Back regime. Here, the atoms in state up have a vanishing magnetic moment as shown in the inset of Fig. A.2. The magnetic gradient does therefore only tilt the potential of the spin-down atoms and they can be spilled from the trap. Afterwards the spin-composition of the sample can be changed by radio-frequency or microwave transitions between the different hyperfine states [Lom11, Zür12a].

4.5. State detection in one and two wells

In a single repetition of the experimental cycle, we can only measure the number of atoms that are in the microtrap at the end of the sequence. However, by repeating

⁸The total spin quantum number can only be changed by introducing a coupling between the spin and the spatial degrees of freedom. In Sect. 5.6, we will use such a coupling to introduce oscillation between spin-singlet and spin-triplet states of two atoms in a double well.

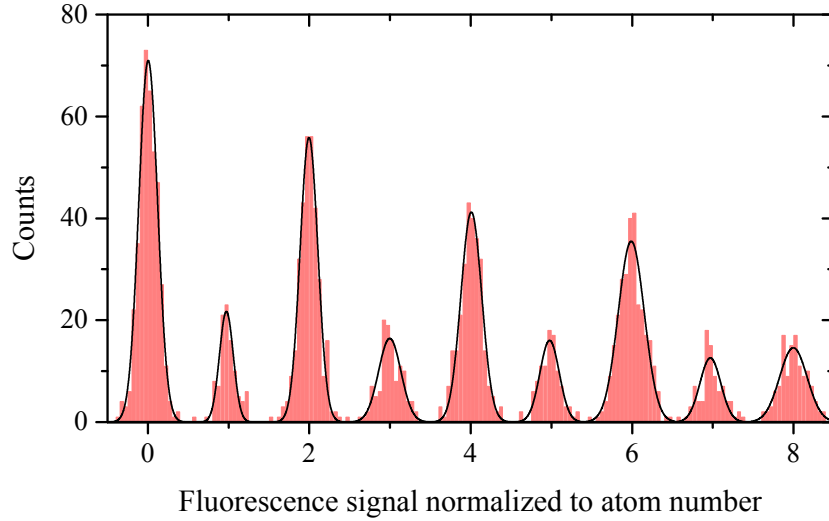


Figure 4.10.: Detection of the atom number. Histogram of the integrated fluorescence signal of the MOT normalized to the number of atoms. The fluorescence signal corresponding to two atoms (six atoms) has a standard deviation of $\sigma = 0.11$ ($\sigma = 0.16$), which leads to a separation of peak centers of about 9σ (6σ).

the experimental cycle over and over again and combining this measurement with specific manipulation processes, additional information about the atomic state can be extracted. We will first explain how we measure atom numbers in our experiment before listing the manipulation processes that we used for the state detection in this thesis.

4.5.1. Atom-number counting

To count the number of atoms, we release them from the microtrap, recapture them in a MOT, and detect their fluorescence signal [Hu94, Ser11b, Hum13]. We imaging the MOT on a CCD camera and integrate the fluorescence signal for 0.5 s. The imaging optics has a numerical aperture of about 0.17, which leads in combination with the quantum efficiency of the camera to the detection of approximately 1 % of the emitted photons [Ser11b]. Finally, the pixel values in the region of the MOT are integrated and normalized to determine the number of atoms [Ser11b, Hum13]. To maximize the signal to noise of this measurement, the MOT parameters are optimized for a small trapping volume and a large fluorescence signal. We therefore apply a magnetic field gradient of 250 G/cm and tune the detuning to a relatively

small detuning of about -2Γ [Ser11b]⁹. In Fig. 4.10 a histogram of the normalized fluorescence signal corresponding to different atom numbers between zero and eight is shown.

4.5.2. Additional state manipulation

By loading the atoms into the microtrap, and counting their number as described in the last section, all information about the spatial state of the atoms in the microtrap, or their spin composition is lost. To gather these important information, we repeatedly prepare the atoms in a certain state and measure the number of atoms after different state-selective spilling processes. These processes are similar to the spilling of atoms from the microtrap for the preparation of few-atom systems (Sect. 4.4.2). For certain measurements we apply combinations of several of these spilling processes.

Measuring the number of spin-up and spin-down atoms

For a system of atoms in the two lowest hyperfine states, we can not only measure the total number of atoms N , but also deduce the number of spin-up atoms N_{\uparrow} and spin-down atoms N_{\downarrow} . To do this, we apply a spilling pulse at 27 G as described for the preparation of spin-imbalanced systems (Sect. 4.4.2). In this pulse we spill all spin-down atoms from the microtrap, while the spin-up atoms remain. Afterwards, we count the number of atoms as described before and thereby determine N_{\uparrow} . The number of spin-down atoms is then calculated as $N - N_{\uparrow}$.

Measuring the population on single-particle trap levels

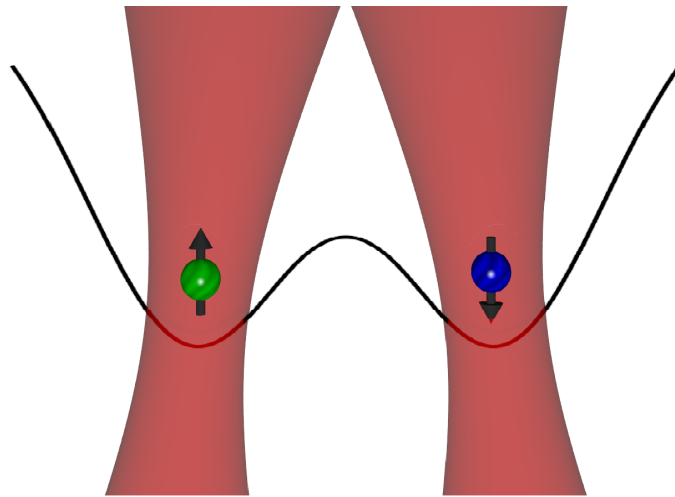
In a noninteracting system, we can measure the mean occupation number on single-particle levels of the microtrap. To do this, we repeatedly prepare an atomic state, remove all population above a certain trap level i by performing our spilling technique, and finally count the number of remaining atoms. The mean number N_i of remaining atoms in the microtrap corresponds to the sum of the populations on trap levels 0 to i . While the population of the ground state is directly given by N_0 , we can calculate the population on excited states as $N_i - N_{i-1}$.

⁹Although the maximum fluorescence signal would be reached at a detuning of $-\Gamma/2$, we use a larger detuning to avoid the risk of losing atoms due to the fluctuating frequency of the laser light.

Measuring the single-well populations in a double well

For atoms in a double-well potential, our atom-counting measurement determines the number of atoms in both wells. To perform site-selective atom-number measurements, we switch off one potential well before transferring only the atoms of the other well into the MOT. For this method to work, we first decouple the two wells by increasing the power in the double-well system to more than 1 mW. With a duration of 2 ms, this separation is fast compared to typical tunneling rates in our double-well system, but slow enough to avoid excitations. Then, we slowly turn off the RF power that generates one of the wells, while keeping the overall light power constant. To avoid the recapture of atoms in excited states of the remaining well, we spill all population above the tenth excited trap level before counting the number of atoms.

5. Two fermions in a double well



This chapter describes the deterministic preparation and manipulation of one isolated spin singlet consisting of two fermionic atoms in a double-well potential. Making use of our scheme for the preparation of few atoms in a single trap (Sect. 4.4), we first prepare one spin-up and one spin-down atom in the ground state of one well, before adiabatically changing the potential shape to reach the ground state of a double well. We demonstrate full control over the double-well system by independently adjusting the interparticle interactions, the tunneling rate between the wells, and the tilt of the potential. We compare the influence of these operations on the two-particle wave function to the predictions of the Hubbard model and find excellent agreement. In particular, we introduce strong repulsive interactions and observe the crossover of the two-particle system into an effective spin model that is governed by the Heisenberg Hamiltonian.

The work presented in this chapter can be seen as a first step in a new approach to the simulation of Hubbard physics in ultracold atom experiments [Jak05, Ess10]. While previous experiments mostly focused on the cooling of fermionic atoms in a bulk system and the subsequent transfer of many atoms into an optical lattice, we aim for a bottom-up approach instead. The idea of this approach is to extend the preparation scheme described in this chapter to arrays of isolated double

wells. Each double well would then contain an individually prepared spin singlet consisting of one spin-up and one spin-down atom. By adiabatically combining the double wells, low-entropy phases of the Hubbard or Heisenberg model showing antiferromagnetic spin correlations could be realized (see Sect. 3.3) [Sac08, Lub11]. Using this approach, we hope to circumvent the temperature limitations of current optical-lattice experiments [McK11, Gre13, Har15], which have so far prevented the observation of long-range spin correlations.

Overview

In Sect. 5.1, we will see that the two-site Hubbard model is easily solvable and therefore offers an ideal test ground for the calibration of the tunneling and interaction parameters and of the potential tilt. We realized this calibration using tunneling experiments, which is the topic of Sect. 5.2. In Sect. 5.3, we will describe the preparation of eigenstates in the double-well system. Despite the simplicity of these two-particle states, they still shows similarities to the phases of the many-body Hubbard model. By introducing strong repulsive (attractive) interactions, we realize the two-particle analog of a Mott-insulating (charge-density-wave) state (Sect. 5.4). In Sect. 5.5 we directly measure the kinetic energy in the two-atom system as a function of the interparticle interactions. For increasing repulsive interactions, we observe that the kinetic energy approaches the characteristic energy of superexchange interactions, which connect the Hubbard and the Heisenberg model (see Sect. 3.1). Finally, in Sect. 5.6, we introduce a coupling between spatial and spin degrees of freedom of two fully separated atoms and thereby introduce oscillations between spin-singlet and spin-triplet states.

Parts of this chapter have been published in Ref. [Mur15a].

5.1. The two-site Hubbard model

The Hubbard model, which was introduced in Sect. 3.1.1, reduces the physics of a two-component many-body system to only two fundamental processes, tunneling of single particles between the neighboring sites of a lattice and interactions of two particles on the same lattice site [Hub63]. With only two interacting atoms and only one tunnel junction, the double-well system presented in this chapter is the minimum working example of the Hubbard model and can be seen as its fundamental building block.

In this section, we discuss the energy spectrum and the eigenstates of the two-site Hubbard Hamiltonian (Eq. 3.3) for different values of the interaction strength and the potential tilt. Furthermore, we will discuss why our double-well system

fulfills the tight-binding and single-band approximation (Sect. 3.4.1) and is therefore suited for the realization of Hubbard physics.

5.1.1. Hamiltonian of the two-site Hubbard model

To simplify the spatial wave function of a many-body system, the Hubbard model assumes a discretization of space and confines the particle positions to the sites of a periodic lattice. In the limiting case of only two sites, the basis states of single-particle wave functions can be written as $|L\rangle$ and $|R\rangle$, which in our system correspond to the atom being in the ground state of the left or the right well¹. All spatial two-particle wave functions can then be written within the basis $\{|LL\rangle, |LR\rangle, |RL\rangle, |RR\rangle\}$ of single-particle combinations. Within this basis, the Hubbard Hamiltonian (Eq. 3.3) can be written as

$$H = \begin{pmatrix} U + 2\Delta & -J^t & -J^t & 0 \\ -J^t & 0 & 0 & -J^t \\ -J^t & 0 & 0 & -J^t \\ 0 & -J^t & -J^t & U - 2\Delta \end{pmatrix}, \quad (5.1)$$

with the tunneling matrix element J^t , the on-site interaction energy U , and the potential tilt 2Δ between the two wells (see Fig. 3.1 and Sect. 3.4.1)².

5.1.2. Eigenstates of the two-site Hubbard model

Diagonalizing the two-site Hubbard Hamiltonian leads to four different eigenstates, whose energies are shown in Fig. 5.1(a) for a symmetric double well ($\Delta = 0$) as a functions of U/J^t and in Fig. 5.1(b) for a noninteracting system ($U = 0$) as a function of the tilt Δ/J^t . Since the Hubbard Hamiltonian commutes with the permutation operator P , each of the eigenfunctions has a fixed exchange symmetry. While $|a\rangle$, $|b\rangle$, and $|c\rangle$ are symmetric, state $|d\rangle$ is antisymmetric with respect to exchange of the two particles. Due to the antisymmetry of the total fermionic wave function, the two particles have to be in a spin-singlet configuration for states $|a\rangle$, $|b\rangle$, and $|c\rangle$, while the spin wave function of state $|d\rangle$ belongs to a spin triplet (see Sect. 2.1). However, since the Hubbard Hamiltonian contains no direct spin

¹See Sect. 3.4.1 for a detailed discussion of the single-particle wave functions in the Hubbard model.

²See footnote 3 on page 36.

5.1. The two-site Hubbard model

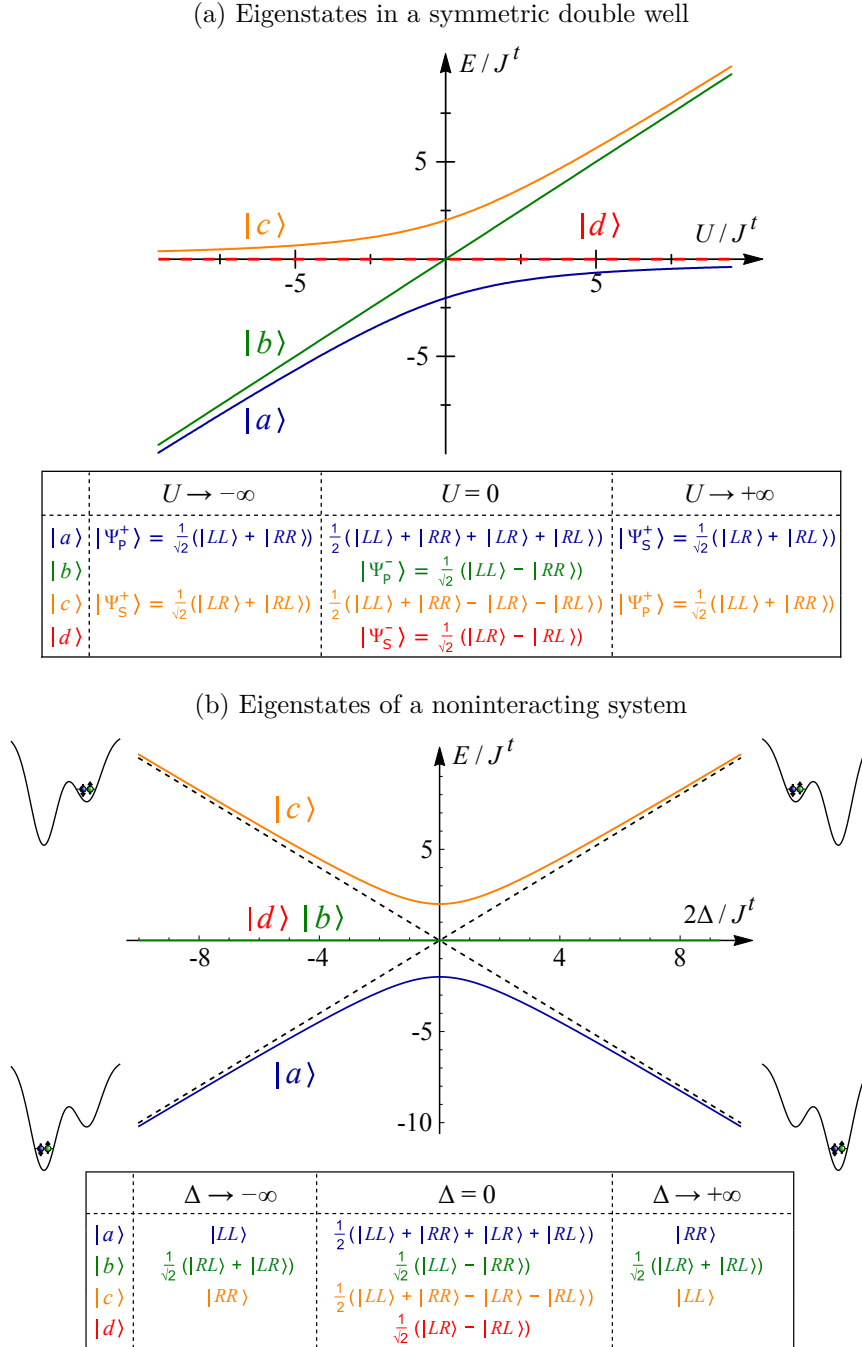


Figure 5.1.: Solution of the two-site Hubbard model. (a) Energy and spatial wave function of the four lowest eigenstates in a symmetric double well ($\Delta = 0$) as a function of the on-site interaction energy U . (b) Eigenenergies and eigenstates in a noninteracting system ($U = 0$) as a function of the potential tilt Δ .

dependence, we will only use the spatial wave function to identify the different states.

The starting point for all experiments presented in this chapter are two atoms, one spin-up and one spin-down, in the ground state of a single well (see Sect. 4.4). The spatial wave function of this initial state is symmetric with respect to the exchange of the two atoms (see Sect. 4.4.3). Since we do not change this symmetry during our experiments, all measurements are performed on the spatially symmetric states. Only in Sect. 5.6, we introduced a controlled coupling between the position and the spin of the atoms by applying a spin-dependent magnetic field gradient. This will allow us to observe oscillations between singlet and triplet spin configurations.

5.1.3. Realization of the two-site Hubbard model

As discussed in Sect. 4.3.2, we realize a double-well system in our experiment by creating two optical microtraps next to each other³. The individual traps are cigar-shaped with a radial harmonic oscillator length of about $0.5 \mu\text{m}$ and an aspect ratio of $\eta \approx 7$. We couple the two microtraps along their radial direction by placing them at a distance of approximately $2\mu\text{m}$ [see Fig. 4.3(b)]. The overall light power P_{tot} in both trapping beams is stabilized and can be adjusted to change the potential depth of both wells. Furthermore, the relative depth of the two wells can be varied by changing the relative power of the RF signals used to create the two trapping beams in an AOD (see Fig. 4.5 and Fig. 4.6).

To realize Hubbard physics in this potential, the tight-binding and the single-band approximation, which are basic requirements for the Hubbard model (see Sect. 3.4.1), have to be fulfilled.

The tight-binding approximation contains the assumption that single-particle wave functions can be given in a basis of wave functions localized at the individual lattice sites. As a consequence, the tunneling matrix element J^t and therefore the band width in a many-body system is much smaller than the excitation energy between different Bloch bands. In our experiment, the lowest excitation energy in the individual wells is given by $\hbar\omega_{\parallel}$, where ω_{\parallel} is the trap frequency along the axial direction of the cigar-shaped traps. During the measurements presented in this chapter, ω_{\parallel} is about $2\pi \times 1 \text{ kHz}$ and typical tunneling frequencies between the wells are given by $J^t/h \approx 100 \text{ Hz}$. We therefore conclude that the tight-binding approximation is well fulfilled in our experiment.

The single-band approximation is the assumption that all population of a Hubbard system is contained in the lowest Bloch band, which is a superposition of

³The trap parameters of a single microtrap are listed in App. A.4

the single-particle ground-states of the individual wells. To fulfill this condition, we prepare the initial system in the ground state of a single well and limit both the on-site interactions energy U and the potential tilt Δ to values smaller than the excitation energy $\hbar\omega_{\parallel}$ in the individual wells. For the largest interaction energies used in this chapter of $U \approx h \times 650$ Hz we calculate a minimum overlap of the interacting two-particle wave function in a single well and the respective noninteracting ground-state wave function of approximately 92 %.

5.2. Calibration of the Hubbard parameters

The tunneling matrix element J^t , the on-site interaction energy U , and the potential tilt Δ are the only three parameters of the two-site Hubbard model. Since our goal is to express the results of our measurements within this model, we have to calibrate these parameters for the specific conditions in our experiment. In this section, we will describe the experimental calibration of all three parameters from tunneling measurements. First we will study the uncorrelated tunneling of noninteracting atoms to determine J^t and Δ . Then, we introduce interactions between the two atoms which correlates their tunneling dynamics and allows us to calibrate the on-site interaction energy U . For the experiments described in subsequent sections, these calibrations were used as inputs.

5.2.1. Tunneling measurements

In all tunneling measurements, we start from a noninteracting spin-singlet in the ground state of a single well. This initial state is prepared by using the methods described in Sect. 4.4. We switch on the second well while the overall light power P_{tot} of the trapping beams is large enough to prevent tunneling between the wells ($J^t \approx 0$). We thereby realize state $|LL\rangle$ with both atoms in the left well. By reducing the overall light power P_{tot} of the trapping beams, we quench the tunneling matrix element to a finite value and allow the atoms to tunnel between the wells. For any on-site interaction energy U/J^t and any tilt Δ/J^t , the initial state $|LL\rangle$ can be expressed as a specific superposition of the double-well eigenstates $|a\rangle$, $|b\rangle$, and $|c\rangle$ and hence the tunneling dynamics depends on the Hubbard parameters.

After a specific tunneling time, we quickly increase the overall light power P_{tot} and thereby separate the two wells. We then measure the atom number in the right well using the detection method described in Sect. 4.5. To detect the tunneling oscillations we determine the mean atom number in the right well a function of the tunneling time and obtain plots as shown in Fig. 5.2.

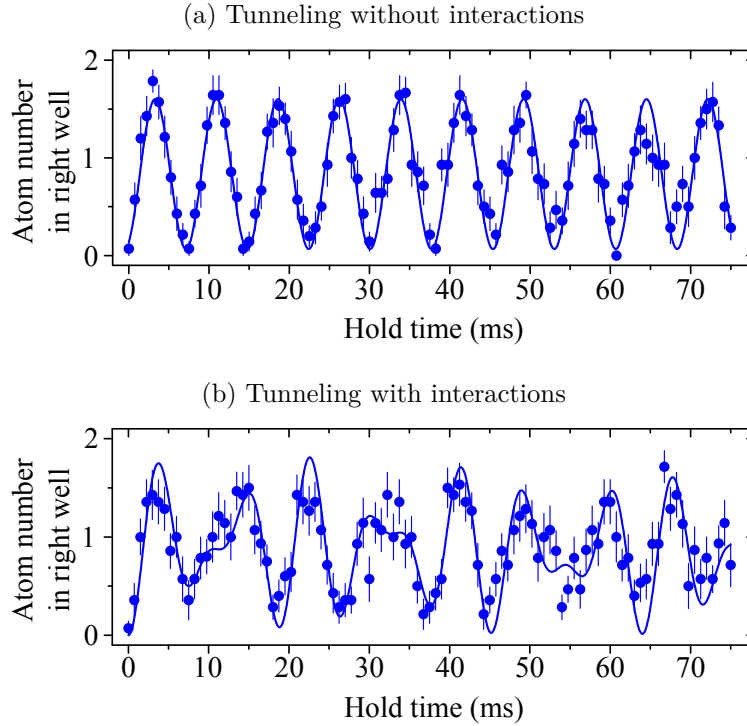


Figure 5.2.: Tunneling with and without interactions in a balanced double well. The data show the time evolution of the mean atom number in the right well after initializing two atoms in the left well and abruptly connecting the wells with a tunnel coupling. (a) For no interactions ($U = 0$), the atoms tunnel independently and we can extract the tunneling frequency J^t/h by a sinusoidal fit to the data (blue line). (b) For an intermediate on-site interaction energy ($U \approx J^t$), we observe correlated tunneling dynamics of the two atoms. The blue curve shows the predictions of the Hubbard model with all Hubbard parameters (J^t , U , and Δ) independently calibrated.

5.2.2. Calibration of the tunneling matrix element

If the two atoms do not interact, their tunneling dynamics between the wells is uncorrelated resulting in sinusoidal oscillations of the atom number in each of the wells [Fig. 5.2(a)]. Each point in this plot is the average of about 15 measurements, which required a total measurement time of approximately 9 hours. To determine the value of the tunneling matrix element J^t , we fit the oscillations with a damped sine wave resulting in values of J^t/h on the order of 100 Hz and typical damping times on the order of 100 ms. Repeating this measurement for different values of the overall light power P_{tot} in the trapping beams during the tunneling dynamics

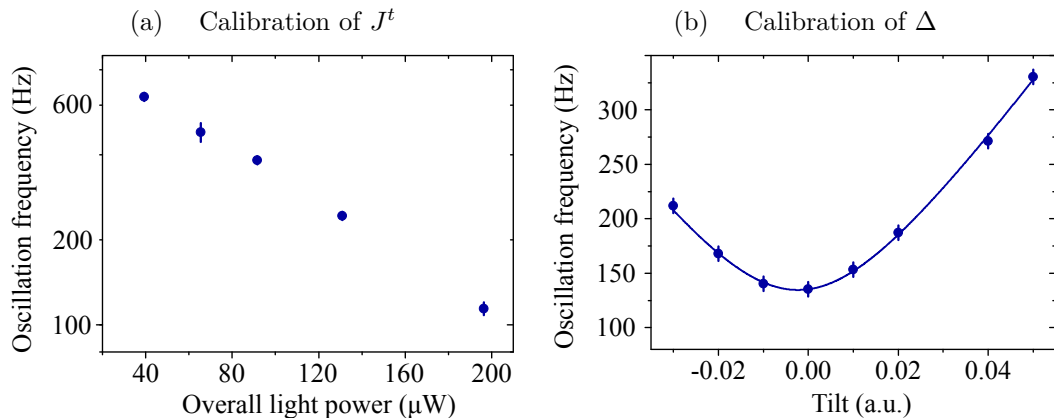


Figure 5.3.: Calibration of the tunneling matrix element J^t and the tilt Δ from tunneling measurements. (a) Tunneling frequency J^t/h of two noninteracting atoms as a function of the overall light power P_{tot} in the trapping beams. Since the potential depth is proportional to the light intensity (see Eq. 4.2), an increase in P_{tot} causes an effective increase of the potential barrier between the two wells and therefore a decrease of the tunneling frequency. (b) Effective tunneling frequency of two noninteracting atoms as a function of the potential tilt. The tilt is controlled by changing the relative power of the RF signals that control the depth of the individual wells (see Fig. 4.5). The blue line shows a fit with the effective tunnel coupling $\sqrt{J^{t2} + \Delta^2}$ expected for a two-level system.

allows us to calibrate the tunnel matrix element in our setup [Fig. 5.3(a)]. For the experiments presented in this chapter, light powers of $P_{\text{tot}} = 131 \mu\text{W}$ and $P_{\text{tot}} = 186 \mu\text{W}$ were used resulting in tunneling frequencies of $J^t/h = (142.0 \pm 0.5)\text{Hz}$ and $J^t/h = (67.3 \pm 0.5)\text{Hz}$.

5.2.3. Calibration of the potential tilt

To calibrate the energy tilt Δ between the two wells, we measure the effective tunneling frequency J_{eff}^t as a function of the relative power of the RF signals that control the depth of the left and the right well. During this measurement, we keep the overall light power in the trapping beams constant. For two noninteracting atoms that tunnel independently between the ground states of the two wells, the Hubbard model reduces to a two-level system. For each of the atoms, the effective tunnel coupling J_{eff}^t as a function of the energy difference 2Δ between the ground state in the left and the right well is given by $J_{\text{eff}}^t = \sqrt{J^{t2} + \Delta^2}$. Fitting this formula to the measured tunneling frequencies allows us to calibrate the potential

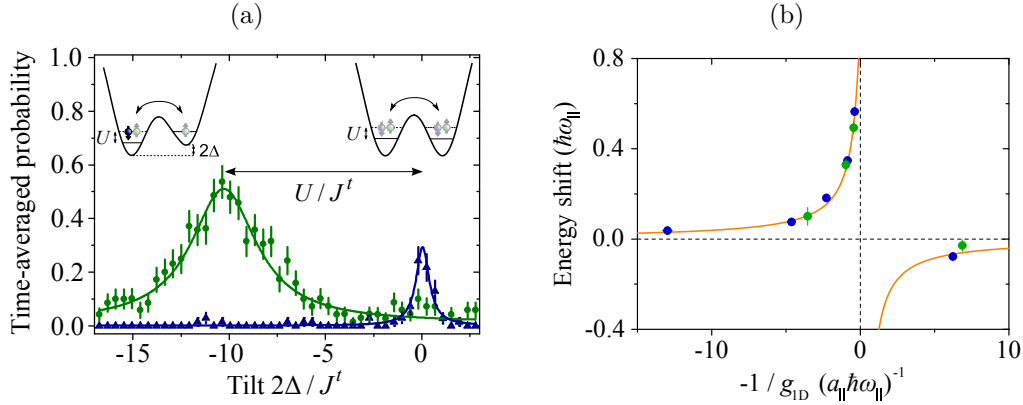


Figure 5.4.: Calibration of the on-site interaction energy. (a) Probability of single-particle (green) and pair tunneling (blue) at a magnetic field of 740 G and a tunneling matrix element of $J^t = (67.3 \pm 0.5)$ Hz as a function of the tilt Δ . At 740 G the two atoms have a scattering length of about $2974 a_0$. While pair tunneling is resonant in a balanced double well ($\Delta = 0$), conditional single-particle tunneling occurs at a tilt of $\Delta = -U/2$. U is extracted from the central positions of the Lorentzian fits to the data (green and blue lines) as $U/J^t = 10.05 \pm 0.19$. (b) Interaction energy in units of the axial harmonic oscillator energy $\hbar\omega_{\parallel}$ as a function of the inverse 1D coupling constant $-1/g_{1D}$ (Eq. 2.22). Blue [green] data point correspond to measurements at a tunneling matrix element of $J^t = (67.3 \pm 0.5)$ Hz [$J^t = (142.0 \pm 0.5)$ Hz]. The orange line depicts the calculated interaction energy of two atoms in one quasi-1D harmonic trap (Eq. 2.30). All measured interaction energies are listed in App. A.3.

tilt Δ and to precisely identify the relative RF power that generates a balanced double-well potential.

5.2.4. Calibration of the on-site interaction energy

In an interacting system, the tunneling dynamics of two atoms becomes correlated [Fig. 5.2(b)]. Thereby, the on-site interaction energy U effectively detunes the energy of states with both atoms occupying the same well. Hence, for large enough U and both atoms in one well, only pair tunneling between the states $|LL\rangle$ and $|RR\rangle$ is possible in a balanced double-well [Win06]. However, single-particle tunneling can be restored, when the on-site interaction energy is compensated by a potential tilt of $\Delta = -U/2$ [Föl07, Sim11]. Measuring the amplitude of single-particle tunneling for a given interaction strength as a function of the potential

tilt therefore allows us to calibrate the on-site interaction energy U .

To perform this calibration, we again start with state $|LL\rangle$, but this time ramp the magnetic field away from the zero-crossing of the scattering length at 527 G to introduce interparticle interactions (see Fig. 2.2.3). For a given tilt Δ of the potential, we couple the two wells and let the system evolve for different hold times. Finally, we measure the number of atoms in the right well. By averaging the probability of finding one atom (two atoms) in the right well over different hold times, we extract the strength of single-particle (pair) tunneling for a given tilt Δ and a magnetic field value B .

For a magnetic field value of 740 G and a tunneling matrix element of $J^t/h = (67.3 \pm 0.5)$ Hz the results of such a measurement are shown in Fig. 5.4(a) as a function of the potential tilt Δ . By using the calibration between Δ and J^t , the on-site interaction energy U can be extracted in units of J^t by comparing the resonance position of single-particle and pair tunneling. In Fig. 5.4(b) the results of these measurements are shown for different interaction strengths and different values of the tunneling matrix element. Because of the strongly-elongated potential shape of the individual wells, we plot the interaction energies as a function of the 1D coupling constant g_{1D} , which characterizes the strength of the contact scattering potential in a 1D systems (see Sect. 2.2.4). Thereby, g_{1D} was determined by using the calibration between the magnetic field and the 3D scattering length a_{3D} shown in Fig. 2.5 and by using Eq. 2.22 to relate a_{3D} and g_{1D} .

We confirm that the interaction energy is not affected by off-site interactions between the wells by comparing the measured data to the calculated interaction energy in a single well as determined by Eq. 2.30 [solid line in Fig. 5.4(b)]. Since we find good agreement for both repulsive and attractive interactions, we use the calculated values as a calibration for the on-site interaction energy.

5.2.5. Validity of the Calibrations

Using the calibrated Hubbard parameters we can fully describe the tunneling dynamics of two interacting atoms in our double-well potential as shown by the solid line in Fig. 5.3(b) that has no free parameter.

We actively stabilize the total light power P_{tot} (see Sect. 4.3.2) and the magnetic offset field (see Sect. 4.2.5), which leads to a good long-term stability of the calibrations of J^t and U . However, the light power in the two trapping beams is not stabilized individually and hence the calibration of the potential tilt Δ relies on the passive stability of the setup. As discussed in Sect. 4.3.2, this passive stability is currently limited by temperature-dependent drifts of the diffraction efficiency of

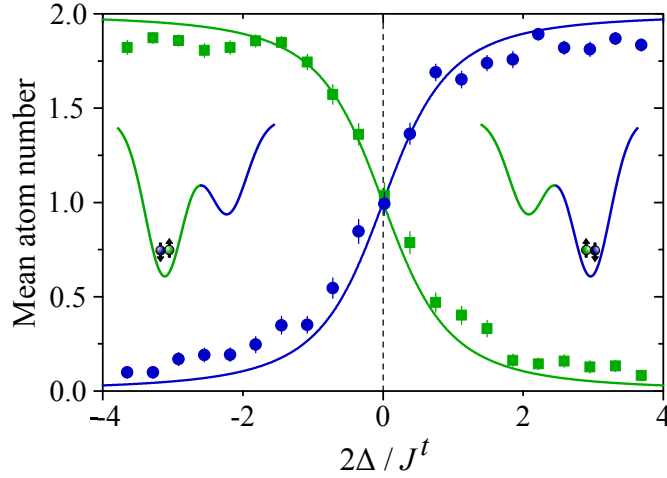


Figure 5.5.: Adiabatic passage of the double-well ground state $|a\rangle$ from $\Delta \ll 0$ to $\Delta \gg 0$. The system is initially prepared in state $|LL\rangle$, the tunneling matrix element between the wells is $J^t = h \times 142.0 \pm 0.5$ Hz, and the tilt is changed with a velocity of approximately $4J^t/100$ ms. The green (blue) data points show the mean atom number in the left (right) well as a function of the potential tilt. Each data point depicts the average of about 130 individual atom-number measurements. The green and blue lines depict the predictions of the Hubbard model [Fig. 5.1(b)].

the AOD, which are on the order of 10 Hz over the course of several days⁴.

5.3. Preparation of eigenstates in the double well

In order to simulate Hubbard physics in our system, we want to prepare the atoms in the ground state of the balanced double well. This capability is also a necessary requirement if we want to use the double well as a building block for larger ground-state Hubbard systems.

To prepare the system in the noninteracting two-particle ground-state $|a\rangle$, we again start with both atoms in the left well. As shown in Fig. 5.1(b), state $|a\rangle$ is approximately given by $|LL\rangle$ for a tilt of $\Delta/J^t \rightarrow -\infty$. We therefore tilt the potential to a value of $\Delta \approx -5J^t$ and then lower the light power to connect the two wells. By slowly changing the potential tilt to $\Delta = 0$, we adiabatically follow state $|a\rangle$ until reaching the ground state of the symmetric double well ($\Delta = 0$). In Fig. 5.5, we demonstrate the adiabaticity of this process by continuing the ramp

⁴We are currently working on the implementation of an active power stabilization for the individual trapping beams to further increase the stability of our system.

to $\Delta/J^t \gg 0$. All population that initially was in the ground state of the left well is then transferred into the ground state of the right well. We conclude that the system occupied the two-particle ground state at every time during the passage.

In a similar preparation scheme, we can also prepare the highest excited state $|c\rangle$ within the ground-state multiplet. Since our two-atom system is well isolated from the environment, this state is stable against decay into energetically lower states. To prepare state $|c\rangle$, we again start from state $|LL\rangle$ but initially set a tilt of $\Delta/J^t \gg 0$. Equivalent to the preparation of state $|a\rangle$, $|LL\rangle$ is now adiabatically connected to the eigenstate of the balanced double-well [Fig. 5.1(b)].

After preparing noninteracting eigenstates of the double-well system, we adiabatically introduce interactions by changing the magnetic field within 60 ms from the zero-crossing of the 3D scattering length at 527 G to values between 300 G ($a_{3D} \approx -288 a_0$) and 740 G ($a_{3D} \approx 2974 a_0$). According to the calibration of the on-site interactions energy described in Sect. 5.2, this corresponds to interaction energies between $U/J^t \approx -1.3$ and $U/J^t \approx 10.1$ for $J^t/h \approx 67.3$ Hz (between $U/J^t \approx -0.3$ and $U/J^t \approx 3.6$ for $J^t/h \approx 142.0$ Hz)⁵.

We confirm the adiabaticity of the preparation process by preparing the system in state $|a\rangle$ of the symmetric double well, ramping to the limit of strong interactions, waiting for different hold times, and finally reversing all ramps to bring the system back into state $|LL\rangle$. Within our statistical uncertainties we detect no heating due to the ramps in Δ and U . The preparation fidelity of eigenstates in the double-well is therefore limited by the preparation fidelity of two atoms in a single well, which in our experiment is typically well above 90 % (see Sect. 4.4).

5.4. Occupation statistics in the double-well

In a first experiment on eigenstates of the double-well system, we measure the distribution of two atoms between the wells as a function of the on-site interaction energy U . We will see that the results for the two-particle ground state show similarities to the metal to Mott-insulator transition of a many-particle Hubbard system [Jör08, Sch08]. Additionally, we will investigate the distribution of atoms in the excited state $|c\rangle$, in which a positive U leads to the formation of repulsively bound pairs [Win06, Föl07]. Finally, we will discuss a particle-hole transformation that connects the states $|a\rangle$ and $|c\rangle$ for any value of the interaction strength U .

⁵Note that both U and J^t depend on the overall light power in the trapping beams.

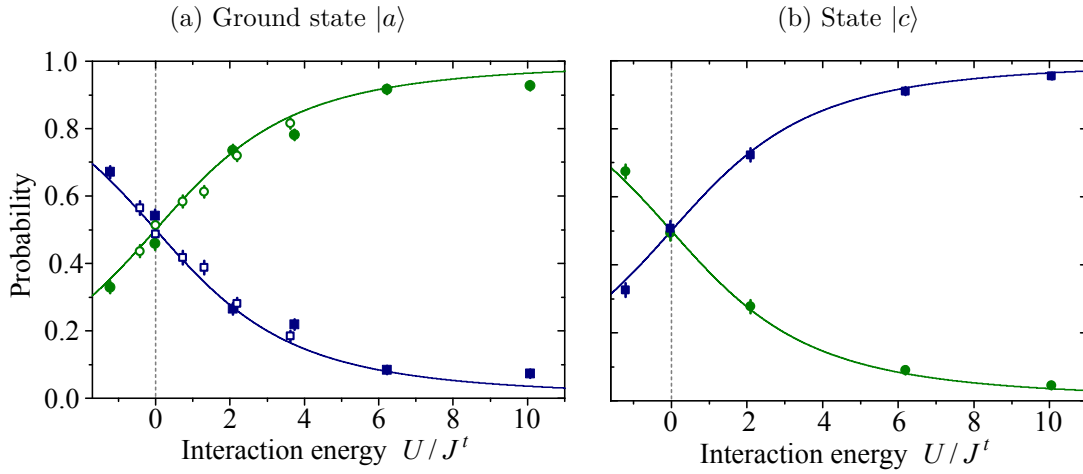


Figure 5.6.: Occupation statistics as a function of the on-site interaction energy. Data points show the probability of two atoms to occupy the same well (blue points) or different wells (green points) in a symmetric double well. Open (filled) symbols correspond to data taken at a tunnel coupling of $J/h = 142$ Hz ($J/h = 67$ Hz). The lines show the predictions of the Hubbard model. (a) For two atoms in the ground state $|a\rangle$, repulsive interactions lead to a suppression of doubly-occupied sites. This can be understood as the two-particle analog of the metal to Mott-insulator transition [Jör08, Sch08]. For attractive interactions the onset of pairing can be observed in the ground state. (b) For atoms in the excited state $|c\rangle$, we observe the crossover into a paired state for repulsive interactions [Win06, Föl07]. The similarity of the curves in (a) and (b) can be explained by a particle-hole symmetry between states $|a\rangle$ and $|c\rangle$ (see Sect. 5.4.4) [Ho09].

5.4.1. Measurement of occupation statistics

To measure the distribution of atoms in a two-particle state $|\Psi\rangle$ between the wells, we quickly separate the wells by ramping up the overall light power. Then, we measure the atom number in either the left or the right well (see Sect. 4.5). We repeat this measurement about 300 times for each well to detect the probabilities a_0 , a_1 , and a_2 of finding zero, one, or two atoms in one of the wells. Using the measurement in the left well as an example, these probabilities are given by the projections

$$\begin{aligned}
 a_0 &= \left| \langle \Psi | RR \rangle \right|^2, \\
 a_1 &= \left| \langle \Psi | LR \rangle \right|^2 + \left| \langle \Psi | RL \rangle \right|^2, \\
 a_2 &= \left| \langle \Psi | LL \rangle \right|^2.
 \end{aligned} \tag{5.2}$$

Combining the probabilities measured in both wells, we define single occupancy as the probability of both atoms occupying different wells ($P_1 = a_1$) and double occupancy as the probability of both atoms occupying the same well ($P_2 = a_0 + a_2$). In Sect. 5.4.2 and Sect. 5.4.3, we describe the measurements of single and double occupancy as a function of U for the ground state and for state $|c\rangle$ of two atoms in a symmetric double well.

Correction of occupation statistics

The probabilities of measuring zero, one, or two atoms in the individual wells (Eq. 5.2) are affected by the finite experimental fidelity of both the preparation of the initial state and the detection of the final state. Both the preparation fidelity and the detection fidelity reduce the mean atom number in the double-well system compared to an ideal measurement. Ideally, two atoms in two wells would lead to a mean atom number per well of one. This allows us to determine the overall fidelity p , by averaging the atom numbers detected in either the left or the right well over all individual shots of a measurement run, which results in typical values of $p \gtrsim 0.9$.

For a symmetric double-well system, we correct the probabilities a_0 , a_1 , and a_2 in the individual wells by

$$\begin{aligned} a_{2,\text{corr}} &= \frac{a_2}{p^2} \\ a_{1,\text{corr}} &= \frac{a_1}{p} - 2\frac{a_2(1-p)}{p^2} \\ a_{0,\text{corr}} &= a_0 - \frac{a_1(1-p)}{p} - \frac{a_2(1-p)^2}{p^2} \end{aligned} \quad (5.3)$$

The effect of this correction on the probabilities P_1 and P_2 of single and double occupancy is $\lesssim 5\%$ for all measurements presented in this chapter.

5.4.2. Ground-state systems

For no interactions ($U = 0$), the ground state of two distinguishable atoms in a balanced double well ($\Delta = 0$) is a combination of two uncorrelated atoms that both populate the single-particle ground state $|L\rangle + |R\rangle$. The two-particle wave function of this state is an equal superpositions of all combinations of placing the atoms in the left and the right well (state $|a\rangle$ at $U = 0$ and $\Delta = 0$ in Fig. 5.1). For this state, equal probabilities of single occupancy and double occupancy are expected, which we observe in the measurement shown in Fig. 5.6(a) at $U = 0$.

Introducing repulsive on-site interactions increases the energy of the basis states $|LL\rangle$ and $|RR\rangle$ and makes their population energetically unfavorable. We observe this as a continuous decrease of the probability of double occupancy P_2 in the ground-state $|a\rangle$ as a function of U . In the limit of $U \gg 0$, the atoms predominantly populate the states $|LR\rangle$ and $|RL\rangle$, which can be understood as a two-particle analog of the Mott-insulating state.

For attractive interactions, the probability of double occupancy in the ground state increases. We interpret this onset of pairing as the two-particle analog of a charge-density-wave state, which in a many-body system is characterized by alternating pairs and empty sites [Ho09, Ess10].

5.4.3. Excited-state systems

In the last section, we saw that the atoms in state $|a\rangle$ tend to form a bound pair for attractive interactions. However, the strength of attractive interactions is limited in our system by the maximum negative scattering length of approximately $-290a_0$ that can be reached below the scattering resonance⁶. As shown in Fig. 5.1(b), we can instead use state $|c\rangle$, which is the highest excited state of the ground-state multiplet, to investigate the emergence of pairing in our system. The occupation-statistics of state $|c\rangle$ clearly depict the crossover into a paired state for repulsive interactions and therefore allow us to reach the charge-density wave regime in our system.

The reason why pairing can be observed in state $|c\rangle$ despite repulsive interactions can be understood from the level structure of states $|a\rangle$ and $|c\rangle$ in Fig. 5.1(a). Both states are superpositions of the symmetric paired state $|\Psi_P^+\rangle$ and the symmetric state of single atoms in each well $|\Psi_S^+\rangle$, which are defined in Fig 5.1(a)⁷. For no coupling between the wells ($J^t = 0$), the energy of $|\Psi_P^+\rangle$ is given by U , while the energy of $|\Psi_S^+\rangle$ is always zero. This means that $|\Psi_P^+\rangle$ has a lower (higher) energy than $|\Psi_S^+\rangle$ for attractive (repulsive) interactions. Between the two regimes, the two states have a perfect crossing at $U = 0$. For finite values of J^t , the states $|\Psi_P^+\rangle$ and $|\Psi_S^+\rangle$ are coupled and an anti-crossing opens up around $U = 0$. This gives rise to the coupled eigenstates $|a\rangle$ and $|c\rangle$ of the Hubbard model. For strong

⁶Approximately three times stronger attractive interactions could be reached by using another combination of hyperfine states. Also, it is technically possible to prepare a ground-state system of two atoms above the scattering resonance and investigate the regime of strong attractive interactions.

⁷Note, that state $|\Psi_S^+\rangle$ is symmetric under the exchange of the two particles, while state $|\Psi_P^+\rangle$ is symmetric under the exchange of pairs and holes.

interactions ($|U|/J^t \gg 1$), the coupled states approach the bare states $|\Psi_S^+\rangle$ and $|\Psi_P^+\rangle$, which leads to identical occupation statistics in state $|a\rangle$ with attractive (repulsive) interactions and state $|c\rangle$ with repulsive (attractive) interactions.

5.4.4. Particle-hole symmetry

The connection between states $|a\rangle$ and $|c\rangle$ can also be used to define a particle-hole mapping between the states⁸. This mapping connects the wave functions of $|a\rangle$ and $|c\rangle$ for any value of U and can be defined as

$$\begin{aligned}
 |a\rangle &= \frac{1}{\sqrt{2}} \left(|\Psi_P^+\rangle + |\Psi_S^+\rangle \right) & |c\rangle &= \frac{1}{\sqrt{2}} \left(|\Psi_P^+\rangle - |\Psi_S^+\rangle \right) \\
 \hline
 |\Psi_S^+\rangle &= \frac{1}{\sqrt{2}} (|LR\rangle + |RL\rangle) & \longleftrightarrow & |\Psi_P^+\rangle = \frac{1}{\sqrt{2}} (|LL\rangle + |RR\rangle) \\
 |\Psi_P^+\rangle &= \frac{1}{\sqrt{2}} (|LL\rangle + |RR\rangle) & \longleftrightarrow & -|\Psi_S^+\rangle = -\frac{1}{\sqrt{2}} (|LR\rangle + |RL\rangle)
 \end{aligned}$$

In this mapping, pairs and empty sites in one state are transformed into spin-up and spin-down particles to generate the wave function of the other state. This mapping explains why the curves in Figs. 5.6(a) and (b) are identical except for exchanged probabilities of single-particle and pair occupancies. Furthermore, this mapping allows to transform a charge-density-wave state with alternating pairs and holes into a Mott-insulating state with alternating spin order and thereby reveals the equivalence of these states within the Hubbard model [Ho09]. In the following section, we will use this connection to measure the energy of superexchange processes in state $|c\rangle$, although they are typically attributed to the ground-state of the Hubbard model.

5.5. Second-order tunneling in the two-site Hubbard model

In this section, we use trap-modulation spectroscopy to measure the kinetic energy of state $|c\rangle$ as a function of the on-site interaction energy U . This allows us to identify the crossover from the regime of single-particle tunneling at weak interactions to correlated second-order tunneling at strong repulsive interactions. As discussed in Sect. 3.1, second-order tunneling leads to antiferromagnetic superexchange interactions in the Mott-insulating ground state of the Hubbard model

⁸Usually, a similar particle-hole transformation is defined between the attractive and repulsive regime of the ground-state Hubbard model [Ho09].

and thereby connects the Hubbard and the Heisenberg Hamiltonian [Aue94]. In the excited state $|c\rangle$, second-order tunneling describes the correlated tunneling of repulsively bound atom pairs [Win06, Föl07]. However, using the particle-hole mapping described in the previous section, we can map pairs and holes in state $|c\rangle$ onto spin-up and spin-down atoms and again explain the second-order tunneling as a superexchange process.

We will first discuss the effect of second-order tunneling on the energy of states $|a\rangle$ and $|c\rangle$ (Sect. 5.5.1). Then, we will introduce trap-modulation spectroscopy for double-well states (Sect. 5.5.2) and finally discuss the results of this measurement (Sect. 5.5.3). Although second-order tunneling has been observed previously [Föl07, Tro08], the experiments in this sections are the first direct measurement of the effect of second-order tunneling on the energy of eigenstates in a system of ultracold atoms.

5.5.1. Second-order tunneling in a double well

In the regime of strong repulsive on-site interactions ($U/J^t \gg 1$), the four states of the two-site Hubbard model with $\Delta = 0$ separate into two doublets that are set apart by U [Fig. 5.1(a)]. While the energetically lower doublet predominantly comprises the singly-occupied states $|LR\rangle$ and $|RL\rangle$, the eigenstates of the upper doublet are to good approximation superpositions of $|LL\rangle$ and $|RR\rangle$. Since single-particle tunneling, which connects the two doublets is far off-resonant for $U \gg J^t$, atoms can only tunnel in a correlated way (Sect. 5.2.4) [Win06, Föl07, Tro08].

For $|LR\rangle$ and $|RL\rangle$ this correlated tunneling can be seen as an exchange process during which the doubly-occupied states are virtually populated (Fig. 3.2). The coupling between $|LR\rangle$ and $|RL\rangle$ can then be calculated from second-order perturbation theory in J^t/U and is given by the superexchange energy

$$J^{ex} = \frac{4J^{t2}}{U}. \quad (5.4)$$

Since the atomic density in these Mott-insulating states is fixed to exactly one atom per site, we can attribute the spin of the atoms to the well they occupy and define a pure spin model (see Sect. 3.2.1 and App. A.1). The basis states of the spin model are given by $\{|\downarrow\uparrow\rangle, |\uparrow\downarrow\rangle\}$, where the first (second) entry in each basis state corresponds to the left (right) well. Within this effective spin basis, the energy splitting of different eigenstates is determined by the Heisenberg

5.5. Second-order tunneling in the two-site Hubbard model

Hamiltonian (Eq. 3.14) [Aue94], which for a two-site model can be written as

$$H = J^{ex} \left(\vec{S}_L \cdot \vec{S}_R - \frac{1}{4} n_L n_R \right) = \frac{1}{2} \begin{pmatrix} -J^{ex} & J^{ex} \\ J^{ex} & -J^{ex} \end{pmatrix}. \quad (5.5)$$

As discussed in Sect. 3.1.2, the eigenstates of this Hamiltonian in a system of one spin-up and one spin-down atom are the spin singlet

$$|\chi^{S=0}\rangle = \frac{1}{\sqrt{2}} (|\downarrow\uparrow\rangle - |\uparrow\downarrow\rangle). \quad (5.6)$$

and a spin-triplet state

$$|\chi^{S=1}\rangle = \frac{1}{\sqrt{2}} (|\downarrow\uparrow\rangle + |\uparrow\downarrow\rangle) \quad (5.7)$$

whose energy is separated by J^{ex} . The spatial wave functions of these two states are the symmetric and antisymmetric superpositions ($|\Psi_S^+\rangle$ and $|\Psi_S^-\rangle$) of the single-occupied basis states $|LR\rangle$ and $|RL\rangle$, respectively [Fig. 5.1(a)].

Also for the doubly-occupied states $|LL\rangle$ and $|RR\rangle$ a second-order tunneling process can be defined, which describes the simultaneous tunneling of both atoms. Here, singly-occupied states are virtually populated and the coupling constant is again given by the superexchange energy J^{ex} [Aue94, Föl107]. Using the particle-hole mapping discussed in the previous section, we can now map a pair of spins in one well onto the single-particle state $|\uparrow\rangle$ and an empty site onto $|\downarrow\rangle$ [Ho09]. The basis functions after this mapping are again given by $|\downarrow\uparrow\rangle$ and $|\uparrow\downarrow\rangle$ and also the upper doublet can be characterized by a Heisenberg spin Hamiltonian. The spatial eigenfunctions $|\Psi_P^+\rangle$ and $|\Psi_P^-\rangle$, which are the symmetric and antisymmetric superpositions of the double-occupied states $|LL\rangle$ and $|RR\rangle$, therefore have exactly the same meaning as $|\Psi_S^+\rangle$ and $|\Psi_S^-\rangle$ for the singly-occupied states.

For both the lower and the upper doublet, the energy of the symmetric states ($|\Psi_S^+\rangle$ and $|\Psi_P^+\rangle$) is affected by second-order tunneling, while any tunneling dynamics in the antisymmetric states ($|\Psi_S^-\rangle$ and $|\Psi_P^-\rangle$) is forbidden. In the Mott-insulating ground state, the sign of J^{ex} is positive, which reduces the energy of the antiferromagnetic spin singlet $|\Psi_S^+\rangle$ by J^{ex} compared to the spin-triplet state $|\Psi_S^-\rangle$ (see Sect. 3.1.2). For the upper doublet, the energy of the symmetric state is increased by $|J^{ex}|$, which can be explained by a ferromagnetic exchange coupling ($J^{ex} < 0$). The reason for this difference to the ground-state system is that state $|\Psi_P^+\rangle$ is coupled to an energetically lower state during the second-order tunneling process, which inverts the sign of the superexchange interactions.

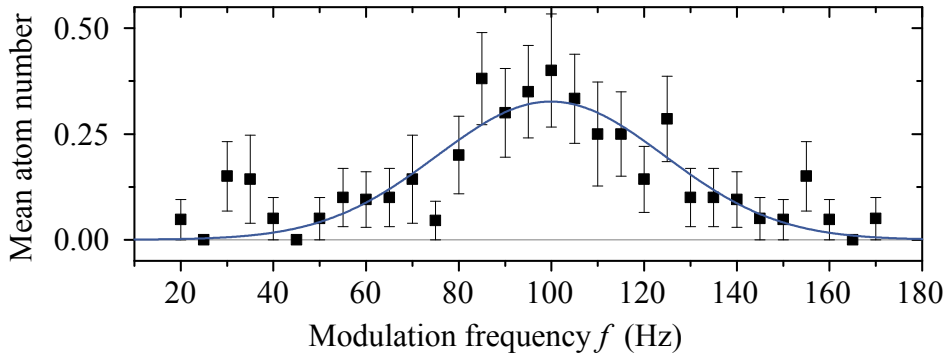


Figure 5.7.: Example of trap-modulation spectroscopy at $U/J^t = 5.9$ and $\Delta/h = -22$ Hz. Black data points depict the mean atom number in the right well as a function of the modulation frequency f . The system is initially prepared in state $|c\rangle$. The measured mean atom number in the right well is proportional to the population transferred to state $|b\rangle$ during 200 ms of trap-depth modulation. The central frequency of the resonance is extracted from a Gaussian fit (blue line) to the data.

Importantly, the exchange of individual atoms in the ground-state doublet is for the excited-state doublet replaced by the exchange of pairs and holes. Therefore, both $|\Psi_P^+\rangle$ and $|\Psi_P^-\rangle$, which are symmetric and antisymmetric with respect to the exchange of pairs and holes, respectively, have the same symmetry with respect to the exchange of individual atoms. This allows us to measure the energy difference between the two states by using trap-modulation spectroscopy as discussed in the next section.

5.5.2. Trap-modulation spectroscopy

To observe the effect of first and second-order tunneling on the energy of a double-well system, we measure the kinetic energy of state $|c\rangle$ as a function of the repulsive interaction strength. We do this by using trap-modulation spectroscopy to determine the energy difference between state $|c\rangle$ and state $|b\rangle$. State $|b\rangle$ has the same interaction energy as $|c\rangle$, but no energy contribution due to tunneling⁹.

We start by preparing the system in state $|c\rangle$ of a symmetric double well with a tunnel coupling of $J^t/h = 67.3$ Hz and ramp the interaction strength to values between $U/J^t = -1.3$ and $U/J^t = 10.1$ (Sect. 5.3). Then, we sinusoidally modulate

⁹We can not use trap-modulation spectroscopy to measure the energy difference between states $|a\rangle$ and $|d\rangle$, since this transition requires the coupling of spatial and spin degrees of freedom (see Sect. 5.6).

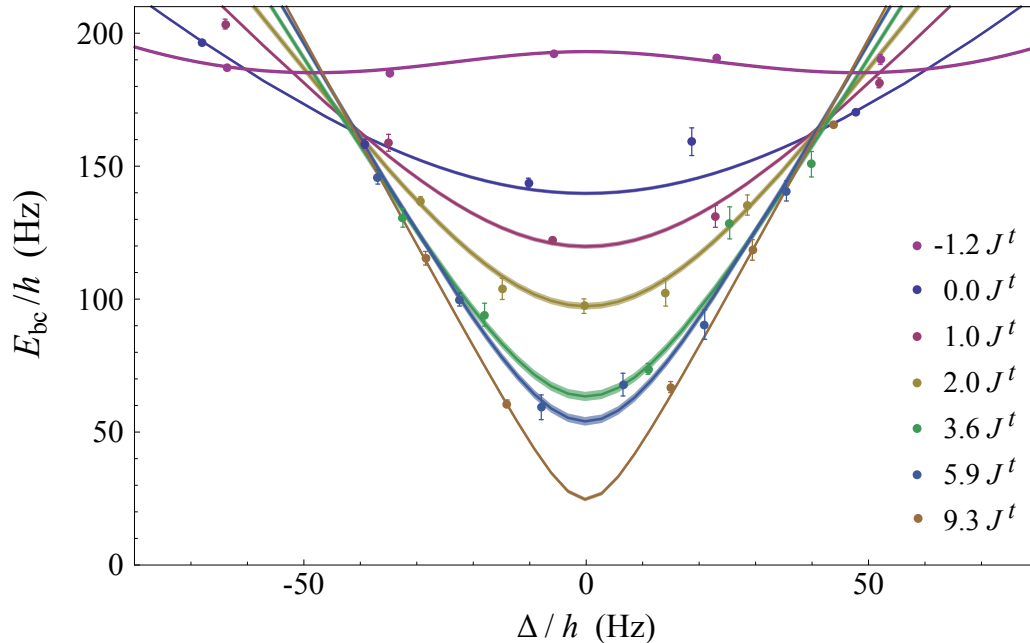


Figure 5.8.: Resonance frequency E_{bc}/h for transitions between states $|b\rangle$ and $|c\rangle$ as a function of Δ measured by trap-modulation spectroscopy. The different colors correspond to different on-site interaction energies. The corresponding lines show fits to the data using the Hubbard model with J^t as a free parameter. All data points and curves were centered around the fitted value of $\Delta = 0$.

the overall light power P_{tot} in the trapping beams for a duration of 200 ms with frequencies between $f = 30$ Hz and $f = 300$ Hz. The amplitude of these modulations is small enough to limit the change of the tunneling coupling to $0.11J^t$. If the frequency of the trap modulation matches the energy difference E_{bc} between states $|b\rangle$ and $|c\rangle$, population is resonantly transferred between the states.

To detect if population has been transferred from state $|c\rangle$ to state $|b\rangle$ during the trap modulation, we adiabatically switch off the interactions and tilt the potential to $\Delta \gg 0$. Then we measure the number of atoms in the right well. If the system is still in state $|c\rangle$, the adiabatic ramps simply reverse the preparation scheme presented in Sect. 5.3 and therefore transfer both atoms back into the left well [Fig. 5.1(b)]. However, if the trap modulation transferred the system into state $|b\rangle$, the final state at $\Delta \gg 0$ has one atom in the right well, which we can detect with high probability. For a fixed value of the interaction energy, we plot the mean atom number in the right well as a function of the modulation frequency f and extract the resonance frequency from a Gaussian fit to the data (Fig. 5.7).

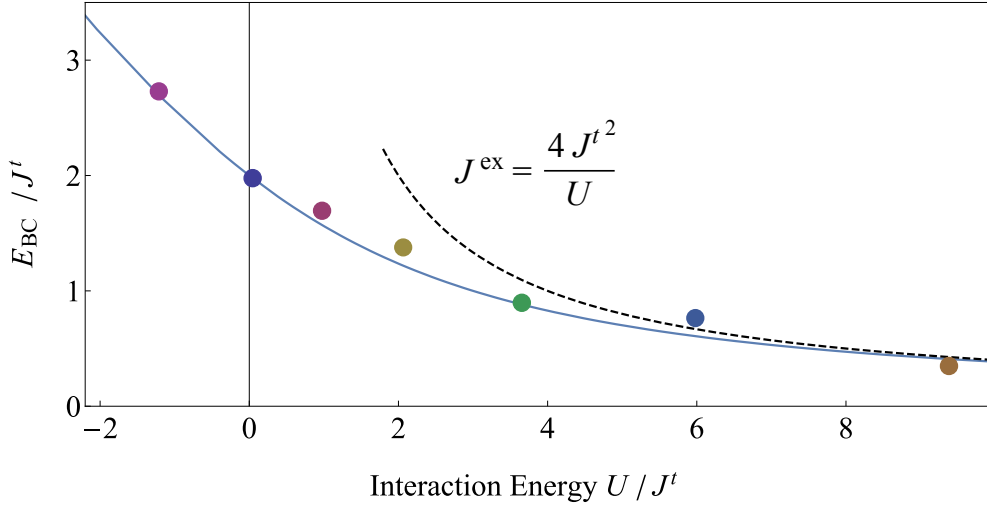


Figure 5.9.: Energy difference E_{bc} between states $|b\rangle$ and $|c\rangle$ measured by trap-modulation spectroscopy. The data points show the energy difference between the two states in a balanced double-well as a function of the on-site interaction energy. For each point, $E_{bc}(\Delta = 0)$ and J^t were extracted from the fits in Fig. 5.8. The coloring of the data points corresponds to the color code of Fig. 5.8. The blue line shows the prediction of the Hubbard model. In a noninteracting system ($U = 0$), the energy difference E_{bc} is given by $2J^t$ due to the uncorrelated single-particle tunneling of the two atoms. For strong interactions E_{bc} approaches the superexchange energy $4J^{t2}/U$ (dashed line), which emerges in the system due to correlated second-order tunneling.

For strong repulsive interactions, the energy difference between states $|b\rangle$ and $|c\rangle$ strongly depends on the tilt Δ between the wells. Therefore, the small residual drifts in the relative depth of the two wells that appear in our experiment over the course of several days (see Sect. 4.3.2), could strongly influence the outcome of this measurement. To solve this problem, we measure the resonance frequency E_{bc}/h as a function of the potential tilt for each value of the on-site interaction energy U . Then, we fit these frequencies with a Hubbard model that uses U as input and has the potential tilt Δ as the dependent variable. J^t is used as a free parameter in this fit, in order to account for variations of the tunneling frequency due to the trap modulation. Finally, the energy difference E_{bc} in a balanced double-well can be extracted from the fit value at $\Delta = 0$. Fig. 5.8 shows all data points and fit curves of the modulation spectroscopy measurement, which were centered around $\Delta = 0$.

5.5.3. Results of the trap-modulation spectroscopy

The extracted values for the energy difference E_{bc} between states $|b\rangle$ and $|c\rangle$ are shown in Fig. 5.9. For $U = 0$, the atoms are uncorrelated and independently delocalized between the two wells. In this limit, each atom raises the kinetic energy of the system by J^t . For increasing interactions, the motion of the atoms is suppressed and finally in the limit of $U \gg J^t$, the atoms only tunnel as pairs and the kinetic energy in the system approaches the superexchange energy of $4J^{t2}/U$. This measurement therefore confirms that state $|c\rangle$ at large repulsive interactions simulates the physics of a ferromagnetic two-site Heisenberg model.

5.6. Singlet-triplet oscillations

Until now, all experiments presented in this chapter were performed on atom pairs in a spin-singlet configuration. In this final chapter, we will lift this constraint and introduce oscillations between spin-singlet and spin-triplet states [Tro10, Gre13]. This change of the exchange symmetry of the spin wave function is only possible if simultaneously the symmetry of the spatial wave functions is adapted. This can be realized by separating the atoms in space and adding an additional term to the Hubbard Hamiltonian that depends on both the position and the spin of the atoms. In the following, we will separate the atoms by bringing them into the Mott-insulating regime and subsequently couple their position and spin with a magnetic field gradient.

5.6.1. Theory of singlet-triplet oscillations

The influence of a magnetic field gradient on our double-well system in the Mott-insulating regime can be included in the Heisenberg Hamiltonian of Eq. 5.5, which is then given by

$$H = \frac{1}{2} \begin{pmatrix} -J^{ex} + 2\Delta_m & J^{ex} \\ J^{ex} & -J^{ex} - 2\Delta_m \end{pmatrix}, \quad (5.8)$$

Here, $2\Delta_m$ describes an energy bias between state $|\uparrow\downarrow\rangle$ and $|\downarrow\uparrow\rangle$ that in our case is given by the differential Zeeman energy $2\Delta_m = (\mu_\uparrow - \mu_\downarrow)(B_L^z - B_R^z)$. In this equation, μ_\uparrow and μ_\downarrow are magnetic moments of spin-up and spin-down atoms (see Fig. A.2), which are predominantly aligned along the z direction by the offset magnetic field, and B_L^z and B_R^z are the z component of the magnetic field at the position of the left and the right well, respectively.

Without any magnetic field gradient ($\Delta_m = 0$), the eigenstates of Eq. 5.8 are given by the spin singlet and the spin triplet states (Eq. 5.6 and Eq. 5.7), which

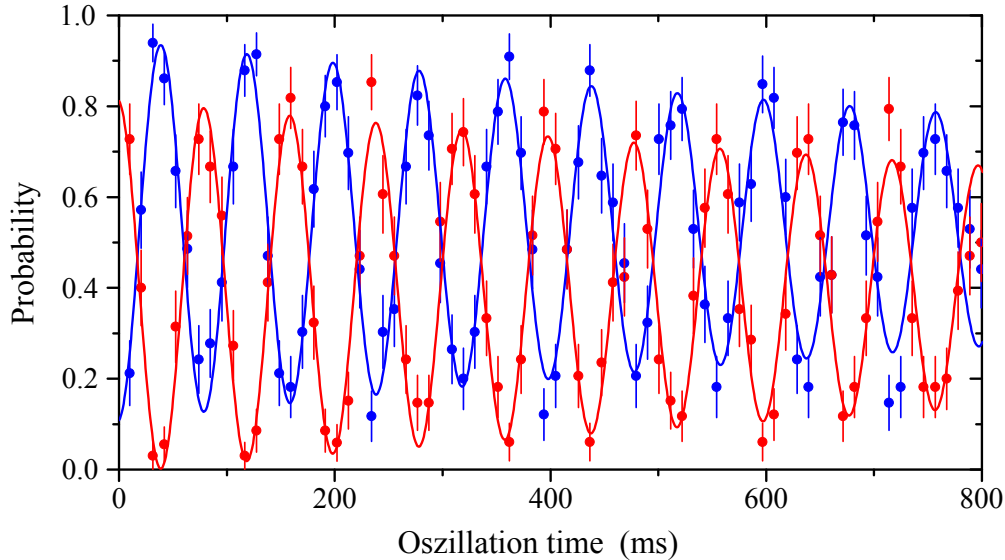


Figure 5.10.: Singlet-triplet oscillations in a double-well potential. The blue (red) data points show the probability of single-occupancy (double-occupancy) in the left well, which correspond to triplet (singlet) spin-correlations between the two atoms. The lines show sinusoidal fits to the data. The singlet-triplet oscillations were performed at a magnetic offset field of 25 G. From the fitted oscillation frequency of (12.53 ± 0.02) Hz and the differential magnetic moment of spin-up and spin-down atoms at 25 G, the magnetic gradient between the atoms can be calculated as (75.9 ± 0.1) mG/cm.

are separated by the superexchange energy J^{ex} (see Sect. 3.1.2). If in contrast, the Zeeman energy is much larger than the superexchange energy ($\Delta_m \gg J^{ex}$), the eigenstates are approximately given by the spin-ordered states $|\downarrow\uparrow\rangle$ and $|\uparrow\downarrow\rangle$. By quickly increasing Δ_m from zero to $\Delta_m \gg J^{ex}$, the singlet and triplet states are therefore projected onto the spin-ordered basis states and the phase between $|\downarrow\uparrow\rangle$ and $|\uparrow\downarrow\rangle$ coherently oscillates with a frequency of $\nu_{\text{STO}} = 2\Delta_m/h$ [Tro10]. In the next section, we will discuss the observation of these oscillations in our experiment.

5.6.2. Measurement of singlet-triplet oscillations

Unfortunately, strong repulsive interactions and a large differential Zeeman energy are hard to realize simultaneously with ${}^6\text{Li}$ atoms in the two lowest Zeeman sub-levels. Repulsive interactions can only be reached at magnetic offset fields above 527 G, where the atoms are far in the Paschen-Back regime and therefore their magnetic moments are nearly identical (Fig. A.3). We therefore perform the spatial

separation of the atoms and the singlet-triplet oscillations at different values of the magnetic field. First, we ramp the ground-state system to 740 G ($U/J^t \approx 10.1$), which is within the Mott-insulating regime, and completely separate the two wells by increasing the overall light power within 40 ms to $P_{\text{tot}} = 900 \mu\text{W}$. This separation is slow enough to ensure that no excitation to higher single-particle trap levels occurs. Then, we quickly (within 12 ms) ramp the magnetic offset field to values below 100 G and at the same time apply a magnetic field gradient^{10, 11}. Although the wells are still completely separated ($J^{ex} = 0$), the relative phase between $|\uparrow\downarrow\rangle$ and $|\downarrow\uparrow\rangle$ will now start to oscillate. To stop the oscillations, we quickly reverse the magnetic field ramps and bring the system back to 740 G.

To detect whether the system is in a spin-singlet or a spin-triplet configuration, we slowly couple the two wells with a tunnel coupling at high magnetic field and thereby return to the singlet and triplet basis states in the Mott-insulating regime. Then, we drive an adiabatic passage to zero interaction strength and subsequently tilt the potential to $\Delta \ll 0$. While this process transfers both atoms of a pure spin-singlet state into the single-particle ground state of the left well, the final wave function of a spin-triplet state has one atom in the ground state and one atom in the first excited state of the left well. Hence, by measuring the probability of double-occupancy and single-occupancy in the ground state of the left well, we can determine the probability of singlet and triplet spin configurations.

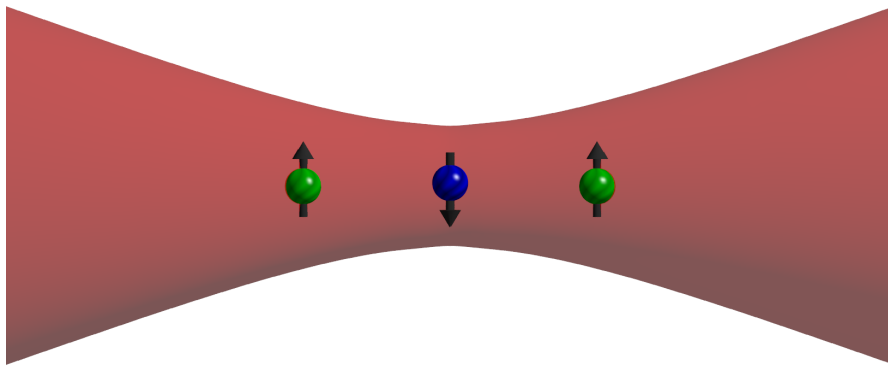
In Fig. 5.10 these probabilities are shown as a function of the oscillation time at a magnetic offset field of 25 G. The oscillations have a frequency of (12.53 ± 0.02) Hz, which allows us to precisely calibrate the gradient of the z component of the magnetic field between the wells to $\partial B^z / \partial r = (75.9 \pm 0.1)$ mG/cm.

It is interesting to note, that singlet-triplet oscillations in our experiment have a damping time of about 2000 ms, which is approximately one order of magnitude longer than the typical damping times of tunneling oscillations. This is due to the fact that the relative phase between the basis states $|\downarrow\uparrow\rangle$ and $|\uparrow\downarrow\rangle$ is not affected by drifts of the overall potential depth or the tilt between the wells, but only by fluctuations of the differential magnetic field between the left and the right well. In the field of quantum-information processing, such decoherence-free subspaces are of particular importance for the storage of information between different computational operations.

¹⁰This magnetic field gradient can either be applied with the Feshbach coils (Sect. 4.2.5), or with the MOT coils (Sect. 4.2.3).

¹¹The quadrupole magnetic field of the coils leads to a gradient of the z component of the magnetic field between the two wells ($|B_L^z - B_R^z| > 0$), since the double-well potential is not perfectly aligned with the symmetry axis of the magnetic field coils.

6. Heisenberg spin chains of few atoms



In this chapter, we describe the realization of antiferromagnetic Heisenberg spin chains using up to four fermionic atoms in two different hyperfine states in the fermionization regime (Sect. 3.4.2). In contrast to the simulation of quantum magnetism in the Mott-insulating state of the Hubbard model (Ch. 5) [Dua03, Gre13, Har15], this method does not rely on the localization of single-particle wave functions in an external periodic potential. Instead, a combination of the Pauli principle and infinitely strong repulsive interactions forces the atoms to form a chain along the axial direction of a strongly-elongated prolate optical dipole trap (Sect. 4.3). The eigenstates of this chain are fully characterized by their spin wave functions [Deu08, Mat08], which are governed by a Heisenberg Hamiltonian [Deu08, Mat08, Deu14, Vol14, Lev15]. The experiments presented in this chapter constitute the first observation of quantum magnetism beyond nearest-neighbor correlations in a system of ultracold fermionic atoms.

Outline

We start this chapter with an intuitive motivation of the theoretical concepts of quantum magnetism in the fermionization regime (Sect. 6.1), which were formally

introduced in Sect. 3.4.2. Afterwards, we discuss the spin-chain Hamiltonian for our few-particle systems using the example of two spin-up and one spin-down atoms. In Sect. 6.2, we describe the deterministic preparation of Heisenberg spin chains consisting of up to four atoms.

The following sections describe two detection methods to identify the specific state of the spin chains. First, in Sect. 6.3, we describe a tunneling technique that allows us to measure the spin orientation of the outermost particle in the trap. By comparing the results to a tunneling model for atoms in a spin chain, we uniquely identify the state of the system. Second, in Sect. 6.4, we probe the spatial wave function of the system by projecting one spin component on single-particle trap levels. The resulting populations on the single-particle trap levels reflect the symmetry of the spatial wave function and therefore, by measuring these populations, we can again distinguish between different spin-chain states. Both measurements reveal that we deterministically prepare the spin chains in their antiferromagnetic ground state. Finally, in Sect. 6.5, we discuss how we can use the tunneling of a single atoms to reach ferromagnetic spin-chain states.

Parts of this chapter have been published in Ref. [\[Mur15b\]](#).

6.1. Spin chains of ultracold atoms in the fermionization regime

To realize a spin model, all states of the system must be fully characterized by their spin wave function. In this section, we will motivate why this is true for fermionic spin-1/2 atoms in the fermionization regime of infinitely strong interactions (Sect. 6.1.2). We will see that for strong but finite interactions, the spin model is still a good approximation and the system is governed by a Heisenberg Hamiltonian. As an example, we will solve this Hamiltonian for two spin-up and one-spin down atom first in a harmonic trap and then for more general trap geometries (Sect. 6.1.2).

6.1.1. The spin-chain picture

Wave functions for infinitely strong interactions

For infinitely strong repulsive s-wave interactions, the relative spatial wave function between any two atoms in a system has to go to zero in order to ensure a finite interaction energy. In a 1D environment, the atoms are therefore impenetrable and their spatial ordering is fixed. As we have seen in Sect. 2.4, this is the regime of fermionization, where the absolute of the spatial wave function of strongly-

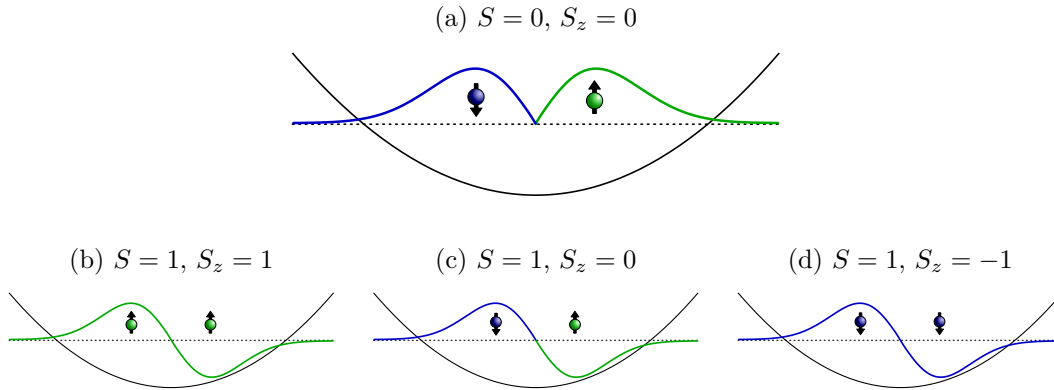


Figure 6.1.: Sketch of the spatial wave functions of two fermionic atoms in a harmonic trap in the fermionization limit. (a) For two atoms in a spin-singlet configuration, the relative spatial wave function between two atoms is symmetric. In the fermionization regime, the infinitely strong interactions cause a kink in the wave function and the atoms become impenetrable. (b-d) For two atoms in a spin-triplet configuration, the spatial wave function is always antisymmetric and therefore independent of the strength of the contact interactions. At fermionization the absolute of all two-particle wave function is identical and the state can fully be characterized by its spin wave function.

interacting atoms has to coincide with the absolute of the spatial wave function of identical fermions [Gir60, Gir10]. However, for a multi-component system of atoms, the internal structure of the atoms, i.e. their spin state, offers an additional degree of freedom and the ground state of the system is degenerate [Deu08, Mat08]. Different states within this ground-state multiplet can now be distinguished by their spin wave function. In Fig. 6.1 we demonstrate this fact for two atoms in a harmonic trap. Although spin-singlet and spin-triplet states have the same absolute spatial wave function, each of the four states has a different spin wave function. This concept can be extended to systems of more than two atoms and thereby allows to define a pure spin model (see Sect. 3.2.1 and App. A.1) [Deu08, Mat08, Deu14, Lev15].

Exchange couplings at finite interactions

For strong but finite interactions ($1 \ll |g_{1D}| < \infty$), the degeneracy in the ground-state multiplet is lifted. In this case, two neighboring atoms with a symmetric relative wave function are not completely impenetrable anymore and hence their ordering in the trap can change (Fig. 6.2). Under the assumption that the spin-chain picture is still valid, this can be described as an exchange process between

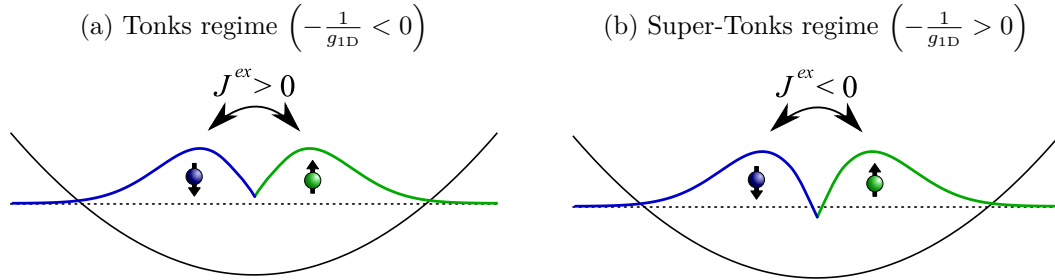


Figure 6.2.: Sketch of the spatial wave functions of two fermionic atoms in a spin-singlet configuration for large but finite interaction strengths. Close to the limit of fermionization, the atoms are not impenetrable anymore and can exchange their position in the trap. (a) In the Tonks regime ($-1/g_{1D} < 0$), this process lowers the energy of a spin singlet. In a spin model such an energy shift is expressed by a positive exchange coupling between the two spins. (b) In the super-Tonks regime ($-1/g_{1D} > 0$), the energy of two interacting atoms increases and can be described by a negative exchange coupling.

two neighboring spins in the spin chain. As discussed in Sect. 3.2.2, such exchange processes allow two spins in a singlet configuration to delocalize and thereby change the energy of the system. In contrast, neighboring atoms with an antisymmetric spatial wave function will always stay impenetrable and therefore spin triplets do not contribute to a change of the energy. Following this argument, we conclude that the state which has the largest energy shift for finite interactions must contain the highest amount of spin-singlet correlations and therefore has the smallest total spin ($S = |N_{\uparrow} - N_{\downarrow}|$) of all states¹. In the following, this state will be called the antiferromagnetic (AFM) state (see Sect. 3.2.3).

In the Tonks regime of strong repulsive interactions, the energy of two atoms in a spin singlet is smaller than in a spin triplet (see Fig. 2.8). The AFM state is therefore the ground state, which according to Lieb-Mattis theorem [Lie62] is the case for a positive exchange coupling ($J^{ex} > 0$). For strong attractive interactions, in the so-called super-Tonks regime, the interaction in a spin singlet raise the energy of the systems and the AFM state is the highest excited state in the multiplet. In this regime, the ground state is a ferromagnetic (FM) state with spin-triplet correlations between all neighboring spins and a maximum total spin of $S = (N_{\uparrow} + N_{\downarrow})/2$. The system can than be expressed as a spin-chain with negative exchange couplings ($J^t < 0$).

¹In general, the spin-singlet correlations in such a state are not localized to any two neighboring spins, but distributed over the whole system.

6.1.2. Eigenstates and energies of three fermionized atoms

Spin-chain Hamiltonian

Since in a two-component system of ultracold fermions with s-wave contact interactions, the SU(2)-symmetry of the individual atoms is conserved, the spin chains in the fermionization limit are governed by the SU(2) symmetric Heisenberg Hamiltonian (see Eq. 3.25) [Mat08, Deu14]. For the example of two spin-up and one spin-down atom this Hamiltonian can be written within the basis $\{|\uparrow\uparrow\downarrow\rangle, |\uparrow\downarrow\uparrow\rangle, |\downarrow\uparrow\uparrow\rangle\}$ of all distinct spin permutations and is given by

$$H_s^{(3)} = E_F^{(3)} \mathbb{1} + \begin{pmatrix} -J_2^{ex} & J_2^{ex} & 0 \\ J_2^{ex} & -J_1^{ex} - J_2^{ex} & J_1^{ex} \\ 0 & J_1^{ex} & -J_1^{ex} \end{pmatrix}. \quad (6.1)$$

Here, $E_F^{(3)}$ is the energy of three noninteracting identical fermions and J_1^{ex} (J_2^{ex}) is the exchange coupling between the left and the central (central and right) spin. Following Eq. 3.26, the exchange couplings

$$J_i^{ex} \propto \frac{n^3}{g_{1D}} \quad (6.2)$$

are proportional to the inverse 1D interaction strength and approximately proportional to the local density cubed. While the latter leads to a dependence of the J_i^{ex} on the trap geometry [Deu14, Vol14, Lev15], the proportionality to $1/g_{1D}$ ensures that $J_i^{ex} > 0$ ($J_i^{ex} < 0$) in the Tonks (super-Tonks) regime [Mat04a, Mat08, Deu14].

Eigenstates and energies in a harmonic trap

Diagonalizing the Hamiltonian in Eq. 6.1 leads to a multiplet of three states. Since the exchange coupling depend on the local density in the trap, the eigenstates differ for different trap geometries. We will first calculate the eigenstates in a harmonic trap, before turning to the case of a tilted potential, which is important for the tunneling measurements in Sect. 6.3.

In a harmonic trap, the density distribution is symmetric and hence, according to Eq. 6.2, the two exchange couplings are equal ($J_1^{ex} = J_2^{ex}$). In this case, the eigenstates are the antiferromagnetic (AFM), the intermediate (IM), and the

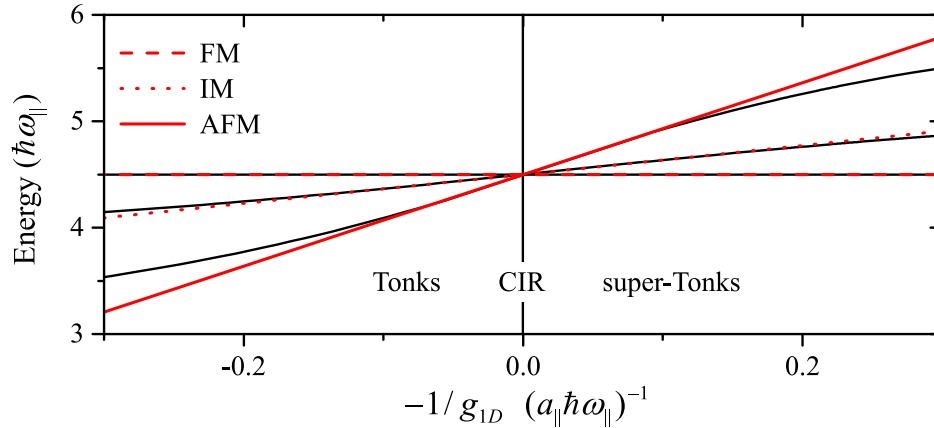


Figure 6.3.: Energies of two spin-up and one spin-down atom in the fermionization regime in a harmonic 1D trap. The red lines show the linear solutions of the Heisenberg spin-chain model, which are good approximations of the exact energies (black lines) for $|g_{1D}| \ll 1$ (see Fig. 2.9). In the Tonks regime below the CIR ($-1/g_{1D} < 0$), the antiferromagnetic (AFM) state ($S = |N_\uparrow - N_\downarrow| = 1/2$) has the lowest energy, while in the super-Tonks regime above the CIR ($-1/g_{1D} > 0$) it is the highest excited state of the multiplet. For any value of g_{1D} , the noninteracting ferromagnetic (FM) state ($S = (N_\uparrow + N_\downarrow)/2 = 3/2$) has the same energy ($E_F^{(3)} = N^2/2 = 4.5\hbar\omega_{||}$) as three identical fermions.

ferromagnetic (FM) state, which are given by

$$\begin{aligned}
 |AFM\rangle &= \frac{1}{\sqrt{6}} \left(|\uparrow\uparrow\downarrow\rangle - 2|\uparrow\downarrow\uparrow\rangle + |\downarrow\uparrow\uparrow\rangle \right) \\
 |IM\rangle &= \frac{1}{\sqrt{2}} \left(|\uparrow\uparrow\downarrow\rangle - |\downarrow\uparrow\uparrow\rangle \right) \\
 |FM\rangle &= \frac{1}{\sqrt{3}} \left(|\uparrow\uparrow\downarrow\rangle + |\uparrow\downarrow\uparrow\rangle + |\downarrow\uparrow\uparrow\rangle \right).
 \end{aligned} \tag{6.3}$$

The energies of these states are $E_F^{(3)} - 3J^{ex}$ for the AFM state, $E_F^{(3)} - J^{ex}$ for the IM state, and $E_F^{(3)}$ for the FM state as shown in Fig. 6.3. All three states of the multiplet are degenerate at $g_{1D} = \pm\infty$, where they have the same energy ($E_F^{(3)} = N^2/2 = 4.5\hbar\omega_{||}$) as three noninteracting identical fermions [Gir07]. Due to the proportionality of the exchange couplings to $1/g_{1D}$, all spin-chain states have linear energy shifts in $1/g_{1D}$, with slopes according to the Heisenberg model. As shown in Fig. 6.3, the solutions of Eq. 3.25 are good approximations of the exact

energies of the few-particle system if $1/g_{1D} \ll 1$ is fulfilled².

Eigenstates and energies in an asymmetric trap

In Sect. 6.3 we will use a tilted trap to probe the spin distribution in our system in a tunneling measurement. Since the density distribution in these measurements is asymmetric, the exchange couplings are no longer equal and the eigenstates and their energies are changed compared to the harmonic case. In the basis of eigenstates in a harmonic trap, which were defined in Eq. 6.3, the difference in the exchange couplings leads to a coherent mixing of the AFM and the IM state. The FM state is decoupled due to its different spin symmetry³. The eigenstates in an asymmetric trap can be written as [Mur15b]

$$\begin{aligned} |AFM'\rangle &= \cos(\alpha/2) |AFM\rangle - \sin(\alpha/2) |IM\rangle \\ |IM'\rangle &= \cos(\alpha/2) |IM\rangle + \sin(\alpha/2) |AFM\rangle \\ |FM'\rangle &= |FM\rangle, \end{aligned} \tag{6.4}$$

where the mixing angle α is given by

$$\alpha = \arctan\sqrt{3} \left(\frac{J_1^{ex} - J_2^{ex}}{J_1^{ex} + J_2^{ex}} \right). \tag{6.5}$$

For the tilted trap during our tunneling experiments, the exchange couplings J_1^{ex} and J_2^{ex} were calculated numerically by evaluating Eq. 3.26, leading to typical values of $\alpha \approx 20^\circ$.

Spin densities

Although in the fermionization regime, the total density is the same for all states of the system, the spin densities of the different states differ as shown in Fig. 6.4. These continuous spin densities of atoms in the fermionization regime can be mapped onto discrete probabilities of the individual spins in the spin chain to point up or downwards [Deu08, Deu14]. For any given spin state $|\chi\rangle$, the proba-

²For an arbitrary atom number N , the condition for the spin-chain regime is $\sqrt{N}/g_{1D} \ll 1$, which can be transformed into $\sqrt{N}J_i^{ex} \ll \omega_{ax}$ for all i , where ω_{ax} is the axial trapping frequency. The spin-chain regime therefore gets more narrow for growing atom numbers.

³The ferromagnetic state of the (2, 1) system has a total spin of $S = 3/2$ while the AFM and the IM state both have a total spin of $S = 1/2$.

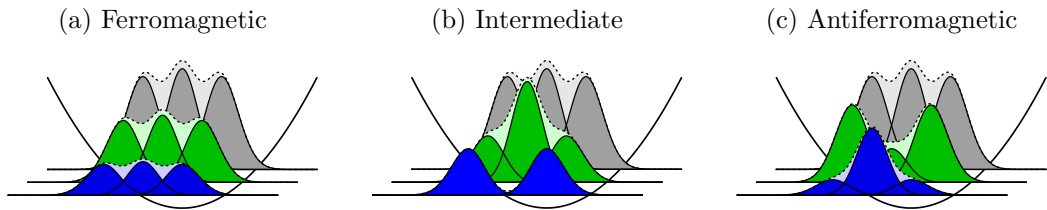


Figure 6.4.: Total density and spin densities of two spin-up and one spin-down atom in the fermionization regime in a harmonic trap. The dark gray areas depict the single-particle contributions to the total density (light gray). The dark green and dark blue areas depict the single particle contributions to the spin densities (light green for spin up and light blue for spin down). While the total density is equal for all states in the fermionization regime, their spin densities differ.

bility $\Pi_m^{(i)}$ for the i th spin to be in spin state m can be calculated as

$$\Pi_m^{(i)} = \sum_{m_1, \dots, m_N = \{\uparrow, \downarrow\}} \left| \langle m_1, \dots, m_N | \chi \rangle \right|^2 \delta_{m, m_i}. \quad (6.6)$$

These discrete probabilities of a spin chain in a harmonic trap are shown Fig. 6.5. By multiplying the spin probability of the i th site with the continuous density distribution of the i th of three noninteracting identical fermions in a harmonic trap, the continuous spin-densities as shown in Fig. 6.4 can be recovered [Deu08].

In Sect. 6.3 we will use a tunneling measurement to detect the probability $\Pi_{\downarrow}^{(N)}$ of the outermost spin in a tilted trap to point up or down. As we will see, this information is sufficient to distinguish between the different spin states of a (2, 1), a (3, 1), and a (2, 2) system.

6.2. Preparation of antiferromagnetic Heisenberg spin chains

To realize Heisenberg spin chains of N_{\uparrow} spin-up and N_{\downarrow} spin-down atoms, we start by preparing noninteracting ground-state systems of atoms in the two energetically lowest hyperfine states. We define spin-up atoms as $|\uparrow\rangle = |m_S = -1/2, m_I = 0\rangle$ and spin-down atoms as $|\downarrow\rangle = |m_S = -1/2, m_I = 1\rangle$ (see Fig. A.1). This preparation technique is explained in Sect. 4.4 and Ref. [Ser11b]. After the preparation of the noninteracting system at 527 G, we ramp the magnetic offset field with a constant rate to values close to the confinement-induced resonance at 780 G (see

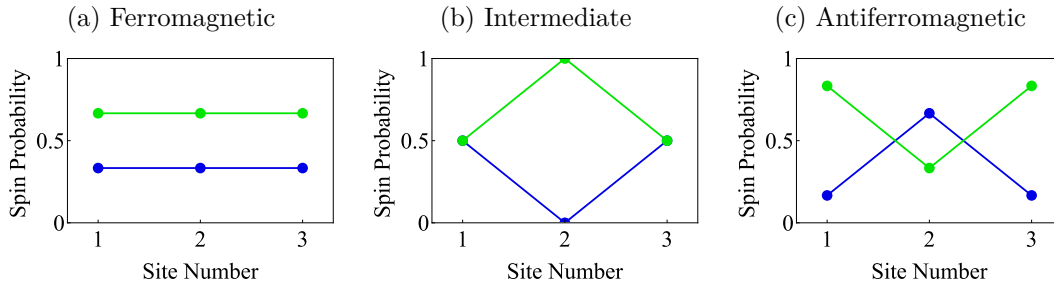


Figure 6.5.: Probabilities of the individual spins in a Heisenberg spin chain of two spin-up and one spin-down atoms in a harmonic trap to point up (green) or down (blue). Starting with the wave functions of the antiferromagnetic, the intermediate, and the ferromagnetic state (Eqs. 6.3), the spin probabilities can be calculated using Eq. 6.6.

Sect. 2.2.4 and Fig. 2.6) and thereby adiabatically increase the interaction strength in the system. As we will show in the next sections, the systems will occupy the respective AFM spin-chain state in the limit of strong repulsion and also stay in this state when crossing the CIR.

Below the CIR, in the Tonks regime of strong repulsive interactions the ground state of each multiplet is an AFM state of minimum total spin [Lie62]. The adiabatic connection between two-component ground-state systems of noninteracting fermions in a harmonic trap and the respective ground state in the limit of strong interactions has been shown in numerical calculations [Gha13, Sow13, Lin14] and by the investigation of the systems symmetries [Har14]. When crossing the CIR to the super-Tonks regime [Ast05, Hal09, Gua10, Zür12b] without the presence of an external symmetry breaking that couples the states, the system will stay in the AFM state [Cui14], which then is the highest excited state of its multiplet. This perfect crossing of the states at the position of the CIR can also be explained in the spin-chain picture. For $g_{1D} \rightarrow \infty$, all exchange couplings J_i^{ex} are zero, (see Eq. 6.2) and therefore the spin distribution in the system is frozen.

It is important to note that this preparation scheme only works because the initial noninteracting state already contains the necessary spin correlations. We will illustrate this fact, using the $(N_{\uparrow} = 2, N_{\downarrow} = 2)$ system.

The ground state of a four-site Heisenberg spin chain is a spin singlet of $S = 0$ [Lie62]. As we have seen in Sect. 3.2.3, this system can be created by adiabatically combining two independent two-site Heisenberg spin chains, which both have a spin of $S = 0$, respectively. A similar process happens when ramping the interaction strength from the noninteracting initial state to the limit of strong repulsion. In

the initial noninteracting state of the (2, 2) system, one spin-up and one spin-down atom occupy each of the two lowest single-particle trap levels. Independent of the trap level, the relative spatial wave function of two atoms on one level is symmetric and therefore their spin wave function has to be antisymmetric. The noninteracting ground state of the (2, 2) system can hence be seen as a state of two independent spin singlets, which necessarily makes the four-particle system a spin singlet, too. When ramping on the interaction strength, couplings between the atoms on different trap levels emerge and the spin-singlet correlations distribute between any two distinguishable atoms in the system. Still the total spin symmetry of $S = 0$ of the four-particle system is conserved for any process that does not contain an external symmetry breaking⁴.

In the next two sections, we will confirm these arguments by measuring the states of the system in the spin-chain regime.

6.3. Probing the spin distribution

6.3.1. Tunneling measurements

To probe the spin distribution of the spin chains and thereby identify their state, we measure the probability of the outermost particle in the trap to point up or down. To do this, we use a tunneling measurement that exploits the fact that in the fermionization regime the atoms are impenetrable. Hence, when we tilt the trapping potential along its axial direction, only the outermost atom can tunnel out of the trap at any time. The spin orientation of the atoms that remain in the trap can then be measured and compared to a tunneling model. In this section, we describe how this detection scheme allows us to determine the initial state of the spin-chain before the tunneling process.

The experimental realization of this tunneling measurement is closely related to the preparation scheme explained in Sect. 4.4. We apply a magnetic field gradient of $B' = 18.92$ G/cm along the longitudinal axis of the microtrap (see Eq. 4.6) and thereby tilt the trap as shown in Fig. 6.6. This creates a potential barrier between the in-trap states and the continuum of states outside of the trap. By lowering the light power in the trapping beam, we effectively lower the height of this potential barrier and thereby allow the outermost atoms to tunnel out of

⁴In the spin-chain regime, a differential magnetic field gradient between the two spin species would be such an external symmetry breaking [Cui14]. However, since close to the position of the confinement-induced resonance at about 780 G the ⁶Li atoms are deep in the Paschen-Back regime (Fig. A.2), their magnetic moments are nearly identical (Fig. A.3). The spin symmetry of the chains is therefore very robust.

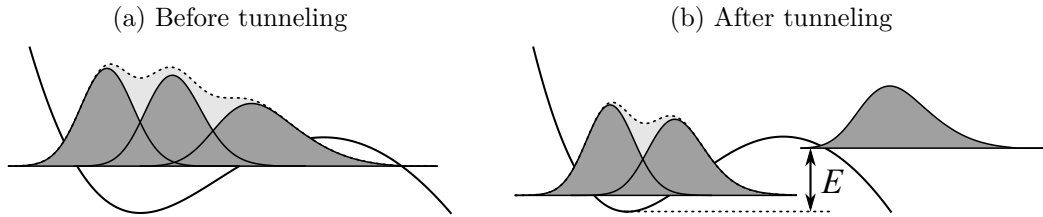


Figure 6.6.: Density distribution of three atoms in the fermionization regime before (a) and after (b) the tunneling of one atom with energy E . The dark gray areas show the single-particle contributions to the total density (light gray). In the fermionization regime, the atoms are impenetrable and only the leftmost atom can leave the trap in the tunneling process.

the trap. We carefully adjust the barrier height and the time until we stop the tunneling process to let exactly one atom (for an initial $(N_\uparrow = 2, N_\downarrow = 1)$ or $(3, 1)$ system) or two atoms (for an initial $(2, 2)$ system) tunnel out of the trap⁵. Finally, we measure the number of spin-up atoms that remain in the trap (see Sect. 4.5) to deduce the spin orientation of the tunneled atoms. We define spin-down tunneling as the process in which all spin-down atoms left the trap during the tunneling process and the final in-trap state is only consisting of spin-up atoms. By repeating this measurement at different values of the magnetic offset field, we measure the probability $P_\downarrow(-1/g_{1D})$ of spin-down tunneling as a function of the inverse interaction strength as shown by the blue data points in Fig. 6.7.

6.3.2. Tunneling model

In order to understand the results of our tunneling measurement and thereby identify the state of the spin-chain, we compare these results to a model for the tunneling of atoms in the regime of strong interactions. This model was developed in collaboration with Frank Deuretzbacher and Luis Santos in Ref. [Mur15b] and will be explained in this section using the example of a $(2, 1)$ system. We will first explain how P_\downarrow is calculated for tunneling at the position of the CIR and then discuss the case of large but finite 1D coupling constants. The comparison of the measured data and the tunneling model is the topic of Sect. 6.3.3.

The tunneling model assumes an initial N -particle state $|i\rangle$ and a final state $|f, t\rangle \equiv |f\rangle \otimes |t\rangle$ after the tunneling of one atom. Here, $|f\rangle$ is the final in-trap state of $N - 1$ spins and $|t\rangle$ is the spin-orientation of the tunneling atom. Both $|i\rangle$ and $|f\rangle$ are assumed to be eigenstates of the spin chain Hamiltonian defined

⁵A list of the trap parameters during this tunneling measurement can be found in App. A.5.

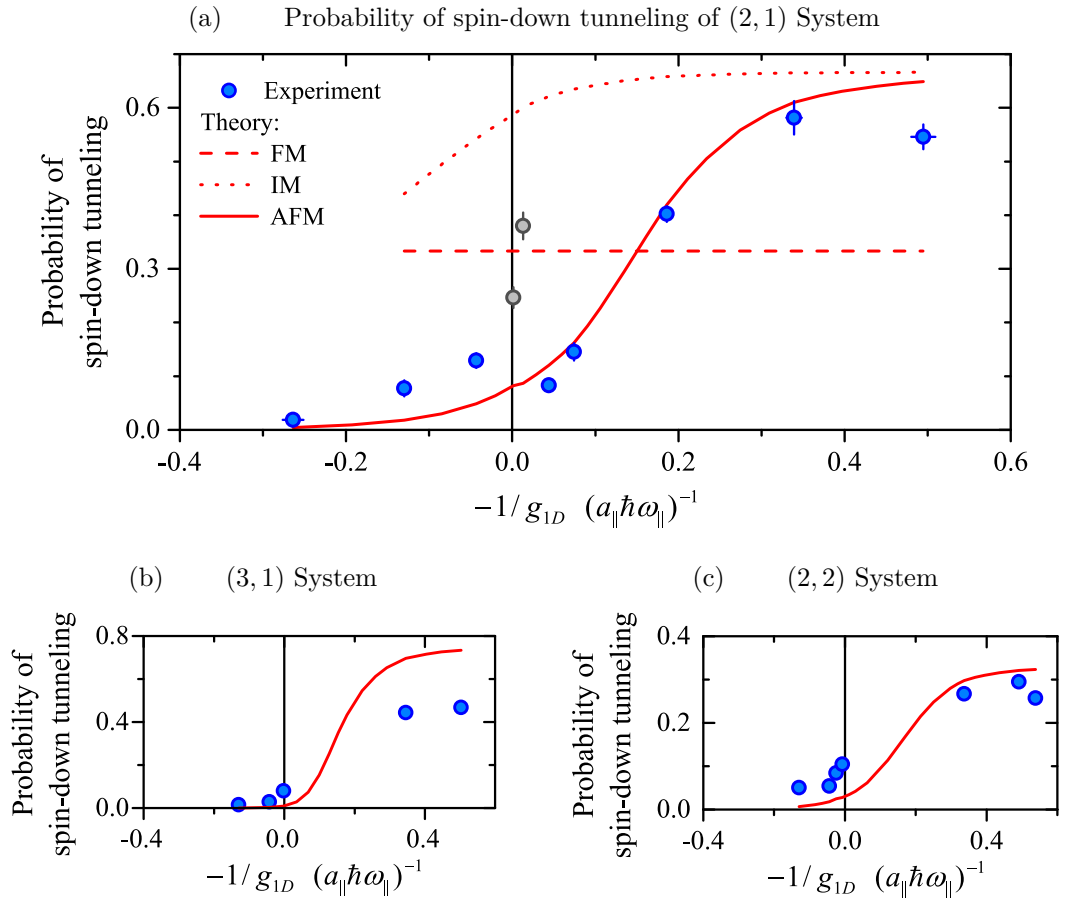


Figure 6.7.: Probability of spin-down tunneling for a ($N_{\uparrow} = 2, N_{\downarrow} = 1$), (3,1), and (2,2) system as a function of the inverse interaction strength. For (2,1) and (3,1) systems [(2,2) systems], we let a single atom [two atoms] tunnel from the trap and measure the probability that the spin of this atom [of both atoms] points down. The blue and gray points show the measured probabilities of spin-down tunneling. The red lines show the solutions of the tunneling model (see Sect. 6.3.2) for the antiferromagnetic state (solid), the intermediate state (dotted) and the ferromagnetic state (dashed). For the sake of clarity, only the theory of the AFM states has been plotted for the (3,1) and the (2,2) system. The gray points in the (2,1) system indicate a resonance effect between the different states at the position of the CIR. The experimental data has been corrected for three and four-body losses. The effect of this correction, which is on the order of few percent and does not significantly alter the presented data is shown in Fig. A.4.

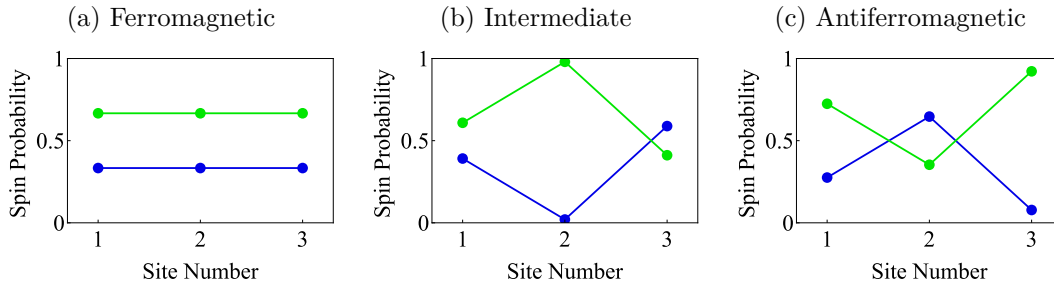


Figure 6.8.: Probabilities of the individual spins of a (2, 1) spin chain in a tilted trap to point up or down. The green (blue) points indicate the probability of the individual spins to point up (down). The asymmetry of the density distribution in the tilted trap of our tunneling measurements (Fig. 6.6) results in a difference of the two exchange couplings in the system ($J_1^{ex} > J_2^{ex}$). In contrast to the harmonic case in Fig. 6.5, this leads to a coherent coupling of the antiferromagnetic and intermediate state with a mixing angle of $\alpha \approx 20\%$.

in Eq. 3.25. In this notation, P_\downarrow is the probability to tunnel into the final state $|f, t\rangle = |\uparrow \cdots \uparrow, \downarrow\rangle$. In the following we will concentrate on the example of two spin-up and one spin-down atom in the initial state.

Tunneling at Fermionization

Directly at the position of the CIR, the expected value of spin-down tunneling $P_\downarrow(0)$ in a (2, 1) system coincides with the probability $\Pi_\downarrow^{(3)}$ of the outermost spin of the initial state to point down (see Eq. 6.6) [Deu14, Vol14, Lev15]. Since during the tunneling process the trap is tilted (Fig. 6.6), the total density is asymmetric and therefore the exchange couplings J_i^{ex} are unequal (Eq. 6.2). This asymmetry will influence the spin composition of any spin chain with more than two atoms and is therefore important for the initial (2, 1) system.

For a given trapping potential, the exchange couplings J_1^{ex} and J_2^{ex} can be numerically calculated using the exact equation in Eq. 3.26. For typical trap parameters during our tunneling measurement (see App. A.5), this results in a mixing angle α of approximately 20° between the AFM and IM state of a harmonic potential (Eq. 6.5). The resulting spin states have the spin probabilities shown in Fig. 6.8. The probability $\Pi_\downarrow^{(3)}$ of the third spin to point down is approximately 8 % for the AFM state, 59 % for the IM state, and 33 % for the FM state. We will compare these calculations to our measurement results in Sec. 6.3.3.

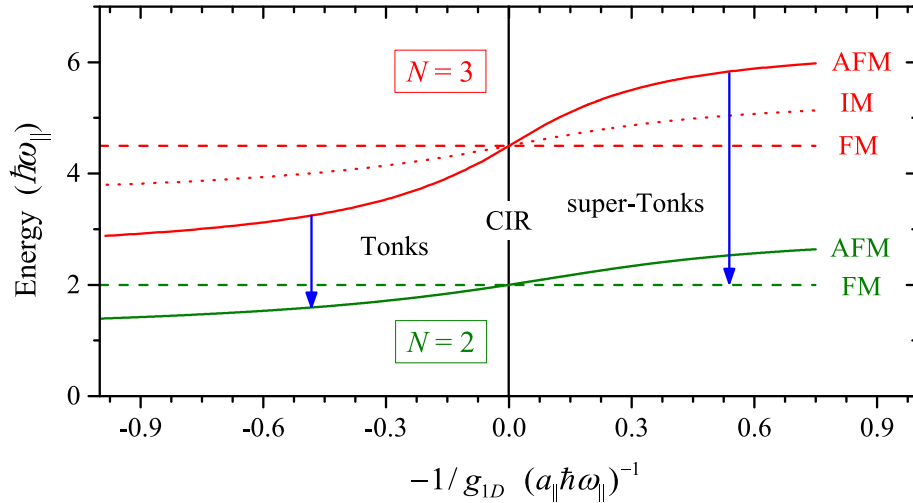


Figure 6.9.: Energies of two (green) or three (red) atoms in the limit of strong interactions. The (2, 1) system is initially prepared in the noninteracting ($-1/g_{1D} = -\infty$) ground state and afterwards ramped to strong interactions. Then, one atom is allowed to tunnel out of the trap. The blue arrows indicate the predominant tunneling channels in the Tonks (left) and the super-Tonks (right) regime for a (2, 1) systems in the antiferromagnetic state.

Tunneling at finite interaction strength

Away from the limit of fermionization, the probability of spin-down tunneling is not simply given by the orientation of the outermost spin anymore. This is due to the energy splitting of the final state multiplet for finite values of $-1/g_{1D}$. Tunneling into final states with lower energy is now favorable as shown by the blue arrows in Fig. 6.9. A change of the interaction strength therefore strongly influences the measured probability of spin-down tunneling although the spin orientations are approximately constant within the regime of strong interactions.

To include this fact in the tunneling model, the tunneling rates $T_{i,f}(-1/g_{1D})$ for specific tunneling channels $|i\rangle \rightarrow |f\rangle$ are calculated as a function of the interaction strength. $T_{i,f}(-1/g_{1D})$ strongly depends on the energy $E_{i,f}(-1/g_{1D})$ of the tunneling particle and can be written as

$$T_{i,f} \propto |\langle i|f, t \rangle|^2 E_{i,f} e^{-2\gamma(E_{i,f})}, \quad (6.7)$$

where the dependence of $T_{i,f}$ and $E_{i,f}$ on $-1/g_{1D}$ was omitted. The energy $E_{i,f}$ is given by the difference of the energies of the initial three-particle and the final two-particle state ($E_{i,f} = E_i - E_f$). E_i and E_f are calculated numerically by inter-

polating between spin-chain solutions at $-1/g_{1D} = 0$ and the weakly interacting limits at $g_{1D} \rightarrow \pm 0$. [Gha15]. The energy-dependent tunneling parameters γ were calculated by means of a WKB calculation [Mur15b].

Finally, the probability of tunneling from state $|i\rangle$ to state $|f, t\rangle$ is given by

$$P_{i,f} = \frac{T_{i,f}}{\left(\sum_{f'} T_{i,f'}\right)}, \quad (6.8)$$

where the sum in the denominator is over all possible final states. Using Eq. 6.8, the probability to tunnel into the spin-polarized in-trap state $|f\rangle = |\uparrow\uparrow\rangle$, which for the (2, 1) system is equivalent to spin-down tunneling, is calculated for an initial AFM, IM, or FM state. The results of these calculations are shown as red lines in Fig. 6.7(a).

Results of the tunneling model

We will shortly discuss the limiting values of the results of the tunneling model for very weak and very strong interactions.

At the position of the CIR, where the interaction strength is infinite, all final states are degenerate and the energy dependent terms drop out of equation Eq. 6.8. In this case the sum in the denominator of Eq. 6.8 amounts to one and the probability of spin-down tunneling is given by $P_{i,f} = |\langle i | \uparrow\uparrow, \downarrow \rangle|^2$. According to Eq. 6.6, this probability is equivalent to $\Pi_{\downarrow}^{(3)}$ and we retrieve the result that at the position of the CIR, the probability of spin-down tunneling is equal to the probability of the rightmost spin in the chain to point down.

Far above and far below the CIR, the energy dependent terms dominate the result of the rate equations in Eq. 6.7 and strongly favor tunneling into final states with lower energies. Below the CIR, the spin-singlet state $|1/\sqrt{2} (\uparrow\downarrow - \downarrow\uparrow)\rangle$ has the lowest energy of all two-particle states and therefore tunneling of spin-up atoms is enhanced. For both the AFM and the IM state of the (2, 1) system this leads to a limiting probability of $P_{\downarrow} = 0$ in the limit of weak repulsive interactions. For the initial FM state P_{\downarrow} stays finite since the spin-overlap to the final spin-singlet state is zero.

Above the CIR, the FM two-particle states $|1/\sqrt{2} (\uparrow\downarrow + \downarrow\uparrow)\rangle$ and $|\uparrow\uparrow\rangle$ have the lowest energy of their multiplet. The ratio between tunneling into these two final states is determined by their respective spin-overlaps to the initial state. For both the AFM and the IM state of the (2, 1) system, Eq. 6.8 predicts a probability of 66.6 % to tunnel into state $|\uparrow\uparrow\rangle$ far above the CIR.

6.3.3. Comparison of measurement and theory

The (2,1) system

To identify the state of the (2, 1) system as a function of the interaction strength, we compare the measured values of spin-down tunneling [blue and gray data points in Fig. 6.7(a)] with the theoretical predictions (red lines). The comparison clearly shows that the (2, 1) system is in the AFM state both below ($-1/g_{1D} < 0$) and above the CIR ($-1/g_{1D} < 0$). This confirms that the different spin-chain states have a crossing at the position of the CIR that allows us to nonadiabatically follow the AFM state. The trend of the blue data points, which crosses the CIR at approximately 10 % is also in good agreement with the calculated probability of about 8 % for the outermost spin in the AFM state to point downwards (Fig. 6.8).

However, the gray data points, which were taken at small positive values of $-1/g_{1D}$ are significantly above the trend of the blue data points. We suspect that this steep increase in the probability of spin-down tunneling close to the resonance is due to a weak coupling between the different states of the (2, 1) system during the tunneling process. Since at the magnetic field values that correspond to the gray points, three-body trap losses were significantly increased, we expect a coupling between the $|AFM'\rangle$ and the $|IM'\rangle$ state via an intermediate molecular state with center-of-mass excitation to be the dominant coupling process. Coupling to these molecular states close to the CIR is strongly enhanced in the anharmonic potential of our tilted trap [Sal13].

The (3,1) and (2,2) system

Also for the (3, 1) system in Fig. 6.7(b), the general trend of the data points agrees with the predictions of the tunneling model for the AFM state. However, above resonance the data points are significantly below the theory. We suspect that the reason for this discrepancy is that above the CIR the energy of the tunneling particle was above the potential barrier in these measurements. In this case, excited states of the final three-particle system would not be effectively suppressed by the energy-dependent terms in the rate equations (Eq. 6.7). In Sect. 6.5, we will see that for a larger barrier height during the tunneling process all excited state are suppressed and the final state is purely ferromagnetic.

For the (2, 2) system two atoms were allowed to tunnel from the trap and the probability of spin-down tunneling was defined as the probability of both spin-down atoms leaving the trap. In the tunneling model, consecutive single-particle tunneling was assumed. Again, the data points shown in Fig. 6.7(c) agree with the theoretical prediction for the antiferromagnetic initial state.

6.4. Probing the spatial wave function of the spin chains

To independently confirm the results of the previous tunneling measurement, we identify the state of strongly-interacting $(2, 1)$ and $(3, 1)$ systems by probing their spatial wave functions. Specifically, we measure the projection of the spin-down atom in an interacting system on single-particle trap levels. The resulting occupation-number distribution on single-particle trap levels strongly depends on the symmetry of the spatial wave function and therefore allows for the identification of the state.

Projecting on single-particle trap levels

The relative spatial wave function of two distinguishable atoms at $g_{1D} \rightarrow +\infty$ is either symmetric with a cusp between the atoms or antisymmetric with a smooth zero crossing (Fig. 6.1). Although both configurations result in the same energy, the expansion of these wave functions in single-particle trap levels leads to very different results. While the smooth zero crossing can be expressed by only considering the two lowest states in the trap, a sharp cusp can only be realized by including highly excited trap levels. Since for any number of atoms the wave function of the ferromagnetic state has only smooth zero crossings between neighboring atoms, and all other states can be generated by successively adding cusps⁶, the expansion of the spatial wave function in single-particle trap levels is a distinct measure for the state of the system.

To probe the occupations on single-particle trap levels, we project the wave function of the spin-down atom in a strongly-interacting $(2, 1)$ or $(3, 1)$ system on single-particle trap levels. To do this, we first prepare the respective noninteracting systems and ramp them into the regime of strong interactions. Then, we remove the spin-up atoms with a short pulse of light. The light is σ^+ -polarized and resonant to the D2 transition of the spin-up atoms ($|\uparrow\rangle = |j = 1/2, m_j = -1/2; I = 1, m_I = 0\rangle$ to $|j = 3/2, m_j = -3/2; I = 1, m_I = 0\rangle$). We confirm that within our experimental fidelity all spin-up atoms are removed from the trap by the light pulse, while only 3 % of the population of spin-down atoms is lost. With 15 μs , the pulse is much shorter than the inverse trap frequency along the axial direction of approximately 1 ms, which sets the timescale of redistribution in the trap.

⁶States with different numbers of cusps are not necessarily orthogonal and have to be diagonalized to construct an orthogonal basis.

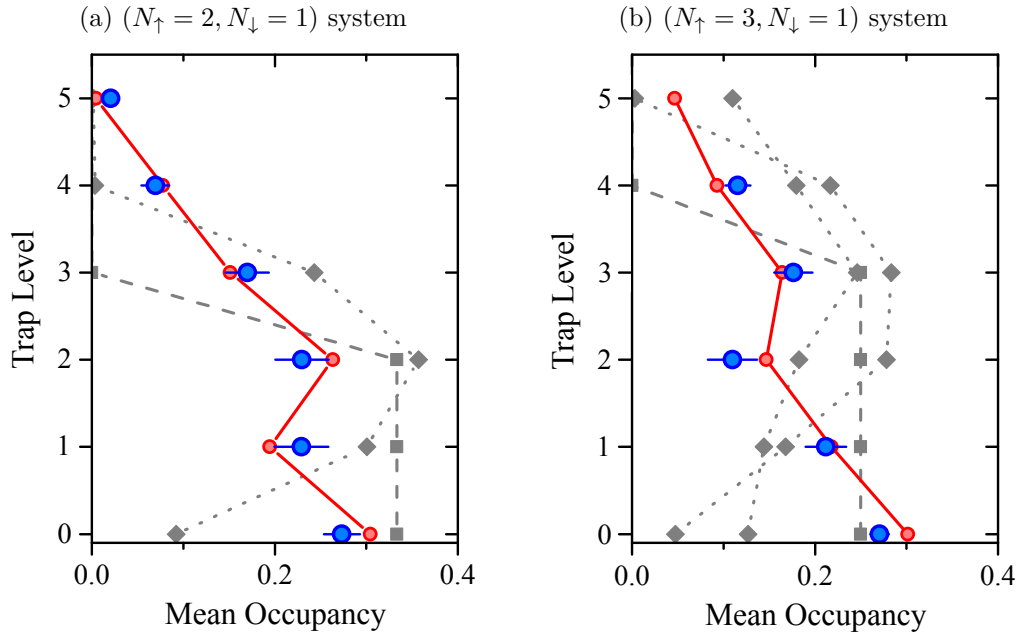


Figure 6.10.: Occupation-number distribution of the spin-down atom in strongly interacting $(2, 1)$ or $(3, 1)$ systems. The wave function of the spin-down atom is projected on single-particle trap levels by a short pulse of light. Blue circles denote the measured population on different trap levels. Red and gray symbols show the theoretical predictions for the AFM state (red circles), the FM state (gray squares) and the intermediate states (gray diamonds). Both measurements were taken in the super-Tonks regime above the CIR ($-1/g_{1D} = 0.586 \pm 0.014$ for the $(2, 1)$ system and $-1/g_{1D} = 0.536 \pm 0.013$ for the $(3, 1)$ system).

Measuring the occupancies on single-particle trap levels

We measure the resulting occupation numbers on single-particle trap levels by using the spilling technique that was introduced in Sect. 4.4. We spill all population above a certain trap level i and measure the number of atoms that remain in the trap (Sect. 4.5). Since we perform this measurement on the spin-down atom in a $(2, 1)$ or $(3, 1)$ system, the measured atom number can either be zero or one. By repeating this measurement several hundred times for each of the few lowest trap levels, we detect the mean atom number N_i on trap levels 0 to i . While N_0 directly reveals the mean occupancy on the ground state, we subtract N_{i-1} from N_i to obtain the mean occupancy on trap level i .

We correct the measured mean atom numbers N_i of spin-down atoms for the finite fidelity of our experiment. To do this, we measure the mean atom number

N_{all} in a trap that still contains many trap levels. Ideally, N_{all} should be one, but due to the finite fidelity of the preparation of the initial state and the detection of the final atom number, we measure typical values of $N_{\text{all}} \approx 0.9$. We correct each N_i by dividing it by N_{all} . A comparison of corrected and uncorrected occupation-number distributions can be found in App. A.5.

Comparison of experiments and theory

We compare the results of the occupation-number measurement (blue points in Fig. 6.10) to theoretical predictions for the different states (red and gray symbols). These predictions were obtained by numerical diagonalizations of the interacting systems [Sow13, Deu14, Lin14] performed by Johannes Bjerlin and Stephanie Reimann [Mur15b]. For both the (2, 1) and the (3, 1) system, the occupation-number distributions clearly agree with the predictions for the respective AFM state. Since the measurements were taken above the CIR ($-1/g_{1D} = 0.586 \pm 0.014$ for the (2, 1) system and $-1/g_{1D} = 0.536 \pm 0.013$ for the (3, 1) system), we conclude that both systems follow the antiferromagnetic state throughout the whole fermionization regime.

6.5. Tunneling into ferromagnetic spin states

So far, we only discussed the preparation and identification of AFM states. In this section, we will describe how we can use the tunneling of a single atom to generate two and three-particle ferromagnetic states. To detect the FM states, we will use the fact that in a system with only contact interactions, FM states are always noninteracting.

The tunneling model described in Sect. 6.3.2 predicts that for the tunneling of atoms out of the trap, final in-trap states with lower energies are favored. In the super-Tonks regime of ($-1/g_{1D} > 0$), the FM states have the lowest energy in each few-particle system (Fig. 6.9). Far above the CIR, the tunneling channels leading to FM final states therefore dominate all other tunneling channels. When starting from a N -particle initial state, the tunneling of a single atom can therefore be used to create a FM $(N - 1)$ -particle state, if the spin overlap of the initial state and the final FM state is nonzero. Specifically, an initial $(N_{\uparrow} = 2, N_{\downarrow} = 1)$ [(3, 1)] system in the AFM state will tunnel into a FM two-particle [three-particle] in-trap state for tunneling far above resonance.

For both the (2, 1) and the (3, 1) system, different FM final states are reached by the tunneling of a single atom. The ratio between these final states only depends on the respective spin overlaps as specified by Eq. 6.7 and Eq. 6.8. Here, the

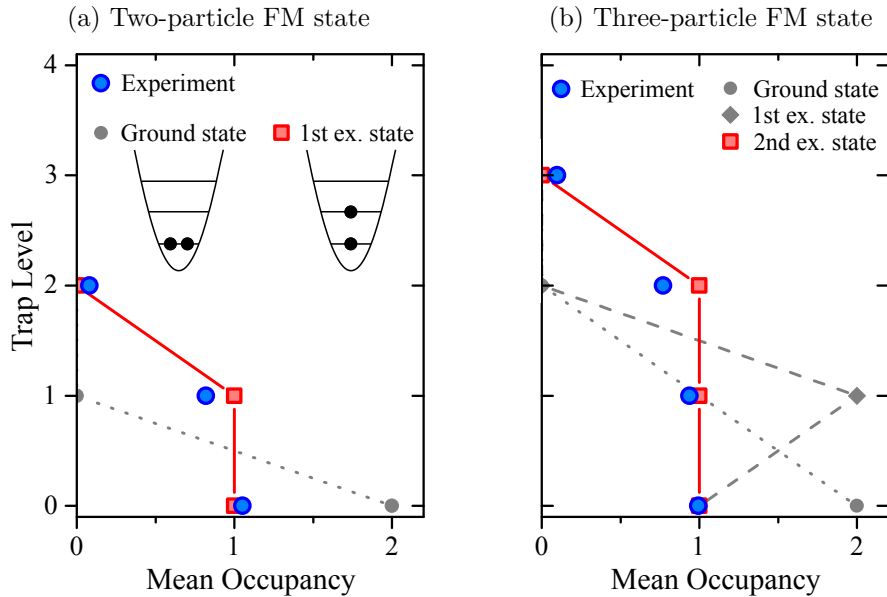


Figure 6.11.: Ferromagnetic states. Measurement of the mean atom number per trap level (blue circles) and expectations for the states of the ground-state multiplet (red and gray symbols). (a) Final two-particle state of an initial $(2, 1)$ system after the tunneling of a single atoms at $-1/g_{1D} = 0.553 \pm 0.015$. (b) Final three-particle state of an initial $(3, 1)$ system after the tunneling of a single atoms at $-1/g_{1D} = 0.553 \pm 0.015$. In both cases the mean atom number per trap level was measured after ramping the coupling constant back through the fermionization regime to $g_{1D} = 0$.

probability of tunneling into the spin-polarized final state ($|\uparrow\uparrow\rangle$ for the final two-particle system and $|\uparrow\uparrow\uparrow\rangle$ for the final three-particle system) is identical to the probability of spin-down tunneling. Therefore, the probability of an initial $(2, 1)$ [$(3, 1)$] system in the AFM state far in the super-Tonks regime to tunnel into the spin-polarized final state is 66.6 % [75 %] (see Fig. 6.7). In the remaining 33.3 % [25 %] of cases, the systems tunnel into the FM state that still contains one spin-down atom [$1/\sqrt{2} (|\uparrow\downarrow\rangle + |\downarrow\uparrow\rangle)$ for the final two-particle state and $1/\sqrt{3} (|\uparrow\uparrow\downarrow\rangle + |\uparrow\downarrow\uparrow\rangle + |\downarrow\uparrow\uparrow\rangle)$ for the final three-particle state].

As for the previous experiments, we prepare noninteracting $(2, 1)$ and $(3, 1)$ systems at a magnetic field of 527 G (Sect. 4.4). Afterwards, we ramp the magnetic field to values above 1200 G, and thereby bring the systems into the super-Tonks regime. As confirmed in the last sections, this ramp connects the noninteracting few-atom systems to the respective AFM states in the spin-chain regime. We

tilt the trapping potential of the $(2, 1)$ [$(3, 1)$] system at an interaction strength of $-1/g_{1D} = 0.553 \pm 0.015$ [$-1/g_{1D} = 0.495 \pm 0.015$] and thereby allow exactly one atom to leave the trap. The trap parameter during this tunnel process is $p = 0.846 \pm 0.025$ for the $(2, 1)$ system and $p = 0.759 \pm 0.023$ of the $(3, 1)$ system.⁷ After the tunneling process, we ramp the final $(N - 1)$ particle systems back through the fermionization regime and to 527 G. Then, we measure the mean atom numbers on the few lowest trap levels (Sect. 4.5).

The results of this measurement are shown in Fig. 6.11. For both the initial $(2, 1)$ and $(3, 1)$ system, the final $(N - 1)$ -particle states have approximately one atom on each of the $(N - 1)$ energetically lowest trap levels. By comparing this result to the gray and red symbols, which show the expected level occupancies for the noninteracting states of the ground-state multiplet (see Fig. 2.8 and Fig. 2.9), we conclude that both systems predominantly occupy the highest excited states of their respective multiplet. In both cases, this highest excited state is connected to the noninteracting ferromagnetic state. By letting a single atoms tunnel from the trap, we have therefore prepared ferromagnetic states of two or three atoms.

⁷Importantly, the height of the tunneling barrier during the measurement of the $(3, 1)$ system is significantly higher than for the measurements on the $(3, 1)$ system in Sect. 6.3. Tunneling into the intermediate three-particle final states, which caused the deviation of the experimental and theoretical values in Fig. 6.7(b), should therefore be strongly suppressed in this measurement.

7. Conclusion and Outlook

In this thesis, we reported on two separate experiments demonstrating the deterministic preparation of magnetically ordered states in systems of few fermionic atoms. Both experiments open up compelling possibilities of assembling quantum many-body systems from individually prepared building blocks. They are therefore part of a novel bottom-up approach to the simulation of quantum many-body systems with quantum gas experiments.

In the first experiment, we simulated the two-site Hubbard model by trapping two fermionic atoms in a double-well potential (Ch. 5) [Mur15a]. To realize this potential, a setup for the generation of arrays of optical microtraps was implemented during the course of this thesis. Using tunneling measurements, we calibrated all parameters of the two-site Hubbard model, which allowed us to fully predict dynamic and static properties of the system. Furthermore, we demonstrated the deterministic preparation of ground-state Hubbard systems consisting of two atoms in a spin-singlet configuration with a fidelity exceeding 90 %. Using a magnetic Feshbach resonance, we introduced repulsive (attractive) interactions between the atoms and observed the crossover into a two-particle Mott-insulating (charge-density wave) state. In the regime of strong repulsion, where single-particle tunneling is suppressed, we directly measured the influence of superexchange interactions on the energy of the system. We thereby demonstrated the applicability of the Heisenberg Hamiltonian, which emerges as an effective Hamiltonian in the Mott-insulating regime of the Hubbard model.

In the second experiment, we realized a novel approach for the simulation of antiferromagnetic Heisenberg spin chains with ultracold atoms (Ch. 6) [Mur15b]. In this approach, spin chains are created by introducing repulsive interactions between atoms in a strongly-elongated trapping potential [Deu14, Vol14]. In the fermionization limit of infinitely strong repulsion, the atoms self align in the potential [Gir60, Deu08, Mat08], comparable to electrons in a one-dimensional Wigner crystal [Mat04a]. The spin distribution of the atoms and the energy splitting of different eigenstates is then determined by a Heisenberg Hamiltonian. Following these predictions, we deterministically prepared Heisenberg spin chains of up to four atoms. We introduced two independent measurement techniques to test the spin distribution or the spatial wave function of the atoms and concluded that the spin chains form antiferromagnetic states. These measurements constitute

the first observation of quantum magnetism with ultracold fermions that exceeds nearest-neighbor correlations.

Since in the two experiments of this thesis, different systems were used to simulate the Heisenberg model, their combination reveals general properties of quantum magnetism that are independent of its specific realization.

In both experiments, magnetism was observed in the limit of strong repulsive interactions in atomic systems that were prepared in their motional ground state. The repulsion lead to the separation of single-particle wave functions and thereby to the formation of either a Mott-insulating or a fermionized state. In both cases, the energy scale of spin excitations, which depends on the wave function overlap of neighboring atoms vanished, while the energy scale of density excitations stayed finite. This lead to a complete separation of spin and density degrees of freedom, which allowed us to fully describe the atomic samples as pure spin systems. By interpreting exchange processes between neighboring atoms as effective magnetic interactions, we used the energy splitting between different states to simulate the Heisenberg Hamiltonian. In both experiments, the specific properties of the systems that were used in this simulation only entered the Heisenberg Hamiltonian by influencing the strength of the superexchange interactions.

Assembly of many-body Hubbard system

The experiments in this thesis reveal the compelling possibility of assembling atomic quantum many-body systems from individually prepared building blocks. Thereby, the double-well system of Ch. 5 can be seen as the fundamental building block of ground-state Hubbard or Heisenberg systems [Sac08]. By separately preparing several of these double-well systems and adiabatically combining them into a single lattice, low-entropy Hubbard systems of finite size could be realized. Similar techniques could also be applied to optical-lattice experiments, in order to generate even larger systems [Föl07, Lub11, Gre13].

In these ideas, the initial preparation of two atoms in the ground-state of a single potential well [Ser11b], which was the starting point for all our double-well experiments, plays a crucial role. For one, the atoms are directly prepared in a spin-singlet configuration, without the need for any entanglement operations. This is of great importance for the assembly of ground-state spin-1/2 systems, since it ensures the existence of an adiabatic connection between the separated building blocks and the combined system (see Sect. 3.3) [Lie62, Mat01, Lub11]. Furthermore, due to the dimple trick applied in the preparation scheme (see Sect. 4.4), we selected only the lowest-entropy fragment of the atomic sample. This could be an important key in circumventing the temperature limitations of current lattice experiments with fermionic atoms [McK11].

Plaquette states

A first application of this approach in our experiment could be the generation of eigenstates on a quadratic plaquette of four wells. For two spin-up and two spin-down atoms in the system, the ground state on such a plaquette is the minimum example of a s-wave resonating valence bond (RVB) state and given by

$$|\chi_L^0\rangle \otimes |\chi_R^0\rangle + |\chi_T^0\rangle \otimes |\chi_B^0\rangle, \quad (7.1)$$

where $|\chi_i^0\rangle$ are two-particle spin-singlet states and L , R , T , and B represent the left, right, top, and bottom pair of wells. This s-wave RVB state is not the only four-particle spin singlet on a plaquette. By exchanging only two atoms along one of the four sides of the plaquette, the ground state could be transformed into the d-wave RVB state

$$|\chi_L^0\rangle \otimes |\chi_R^0\rangle - |\chi_T^0\rangle \otimes |\chi_B^0\rangle. \quad (7.2)$$

Such RVB states, in which the singlet pairs fluctuate between different configurations, have attracted great attention in recent years due to their proposed connection to high-temperature superconductivity [And87].

Although RVB states could already be prepared with ultracold bosonic atoms in an optical-lattice experiment [Nas12], their realization in our experiment is still a tantalizing goal. While for bosonic atoms, the s-wave RVB state is the highest excited plaquette state and can only be generated by a series of state-manipulation processes [Nas12], it would for fermionic atoms automatically emerge from the combination of two ground-state double-well systems. This makes fermionic RVB systems scalable in size. Additionally, our ability to deterministically prepare a specific atom number would allow us to introduce a controlled amount of doping in the system. Combining these two advantages, d-wave pairing of holes in a system of six atoms on two coupled plaquettes could be observed [Tre06]. This is of particular interest, since the condensation of d-wave pairs in slightly underdoped antiferromagnetic materials is by many believed to be the fundamental mechanism behind high-temperature superconductivity [And02].

Spin ladders

The spin-chain experiments of Ch. 6 present a second route for the assembly of finite-size spin systems. Here, two or more spin chains of equal atom number could be transversally connected with a tunnel coupling in order to simulate spin ladders [Dag96, Gia04]. For weak enough couplings, the atoms still form spin chains within the individual traps, but their state would be influenced by additional superexchange interactions between neighboring chains. For a two-legged spin

ladder consisting of only two coupled spin chains, the necessary potential for this experiment is already given by the two overlapping microtraps used to generate the double-well potential in Ch. 5.

Such spin ladders are intensively studied in solid-state physics, due to their peculiar structure in between one and two-dimensional spin systems [Dag96, Gia04]. Remarkably, spin ladders consisting of either odd or even numbers of coupled spin chains show fundamental differences. In odd-legged spin ladders of infinite length, spin correlations along the individual chains only decay slowly with a power-law dependence on the distance. In contrast, even-legged ladders show a much faster, exponential decay of spin correlations. As a first experiment, two spin chains could be adiabatically coupled and then quickly separated in order to project the eigenfunction of the ladder system on spin-chain states. Using the identification of individual spin-chain states demonstrated in Ch. 6 should then allow us to observe the loss of correlations along the individual spin chains dependent on the transversal coupling strength in the spin ladder.

A. Appendix

A.1. Basic definitions of a two-component spin model

In this section, we compile the basic definitions of a spin model consisting of spin-1/2 particles.

A.1.1. Spin operators for single spins

The Hamiltonian of a spin model is built from the spin operator $\vec{S} = \{S^x, S^y, S^z\}$ that acts on the spin of the particle on one specific lattice site. Spin operators for a spin-1/2 system can be defined from the creation and annihilation operators c_s^\dagger and c_s for a fermionic particle in spin state $s = \{\uparrow, \downarrow\}$ as

$$\vec{S} = \frac{1}{2} \sum_{s,s'=\{\uparrow,\downarrow\}} c_s^\dagger \vec{\sigma}_{ss'} c_{s'}. \quad (\text{A.1})$$

Here,

$$\vec{\sigma} = \{\sigma^x, \sigma^y, \sigma^z\} = \left\{ \begin{pmatrix} 0 & 1 \\ 1 & 0 \end{pmatrix}, \begin{pmatrix} 0 & -i \\ i & 0 \end{pmatrix}, \begin{pmatrix} 1 & 0 \\ 0 & -1 \end{pmatrix} \right\} \quad (\text{A.2})$$

are the Pauli matrices. The spin operator and its components follow the permutation relations of angular momenta

$$[\vec{S}^2, S^\alpha] = 0 \quad \forall \alpha \quad \text{and} \quad [S^\alpha, S^\beta] = \epsilon_{\alpha\beta\gamma} i\hbar S^\gamma, \quad (\text{A.3})$$

where $\epsilon_{\alpha\beta\gamma}$ is the totally antisymmetric tensor. Due to these commutation relations it is always possible to find common eigenvectors of \vec{S}^2 and one of the spin components S^α . We, choose the z direction as the quantization axis and denote the eigenstates of \vec{S}^2 and S^z as $|s, m\rangle$. The quantum numbers s and m are related to the eigenvalues of state $|s, m\rangle$ as

$$\vec{S}^2 |s, m\rangle = \hbar^2 s(s+1) |s, m\rangle \quad \text{and} \quad S^z |s, m\rangle = \hbar m |s, m_s\rangle. \quad (\text{A.4})$$

For a spin-1/2 system, there are two eigenstates for each spin, which are denoted up ($|\frac{1}{2}, \frac{1}{2}\rangle = |\uparrow\rangle$) and down ($|\frac{1}{2}, -\frac{1}{2}\rangle = |\downarrow\rangle$). Additionally, raising (S^+) and lowering (S^-) operators can be defined as

$$S^\pm = (S^x \pm iS^y), \quad (\text{A.5})$$

which connect the two basis states according to

$$\begin{aligned} S^+ |\downarrow\rangle &= \hbar |\uparrow\rangle & S^- |\uparrow\rangle &= \hbar |\downarrow\rangle \\ S^- |\downarrow\rangle &= 0 & S^+ |\uparrow\rangle &= 0. \end{aligned} \quad (\text{A.6})$$

A.1.2. Spin operators for multi-spin systems

Merging single spins into a multi-spin system follows the general rules for the addition of angular momenta (i.e. [Sak85]). Thereby, the Hilbert spaces of the individual spins (i.e. V_m and V_n for the spins on site m and n) are combined with a tensor product ($V_m \otimes V_n$). For a spin state $|\chi\rangle$ of the combined Hilbert space, we define the abbreviated notation

$$|\chi\rangle = |m\rangle \otimes |n\rangle \equiv |m n\rangle, \quad (\text{A.7})$$

where $|m\rangle$ and $|n\rangle$ are states of V_m and V_n , respectively. For each individual spin in the system, a single-particle spin operator can be defined that only effects this spin. Spin operators acting on different sites always commute.

For the whole multi-spin system, the total spin operator $\vec{\mathbf{S}}$, acting on the combined Hilbert space, is obtained by summing up the individual spin operators

$$\vec{\mathbf{S}} = \{\mathbf{S}^x, \mathbf{S}^y, \mathbf{S}^z\} = \sum_n \{S_n^x, S_n^y, S_n^z\}. \quad (\text{A.8})$$

In the same way, raising and lowering operators \mathbf{S}^+ and \mathbf{S}^- can be defined that act on the z component of the total spin.

A.2. Properties of ${}^6\text{Li}$

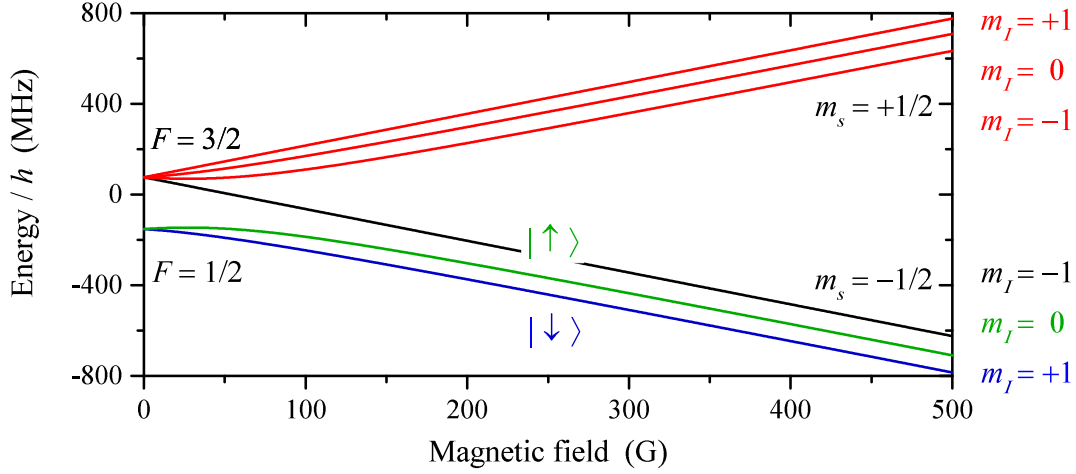


Figure A.1.: Zeeman splitting and hyperfine splitting in the $2S_{1/2}$ ground state of ${}^6\text{Li}$ as a function of the magnetic field. At low magnetic field, the electronic spin of $S = 1/2$ and the nuclear spin of $I = 1$ are coupled to either $F = 1/2$ or $F = 3/2$. Above ~ 50 G, the system enters the Paschen-Back regime and S and I decouple. In the Paschen-Back regime, the hyperfine splitting between different states with $m_S = -1/2$ has a value of ≈ 80 MHz. The two energetically lowest states are denoted up ($|\uparrow\rangle = |m_S = -1/2, m_I = 0\rangle$) and down ($|\downarrow\rangle = |m_S = -1/2, m_I = 1\rangle$) and are used throughout this thesis to realize a two-component Fermi system.

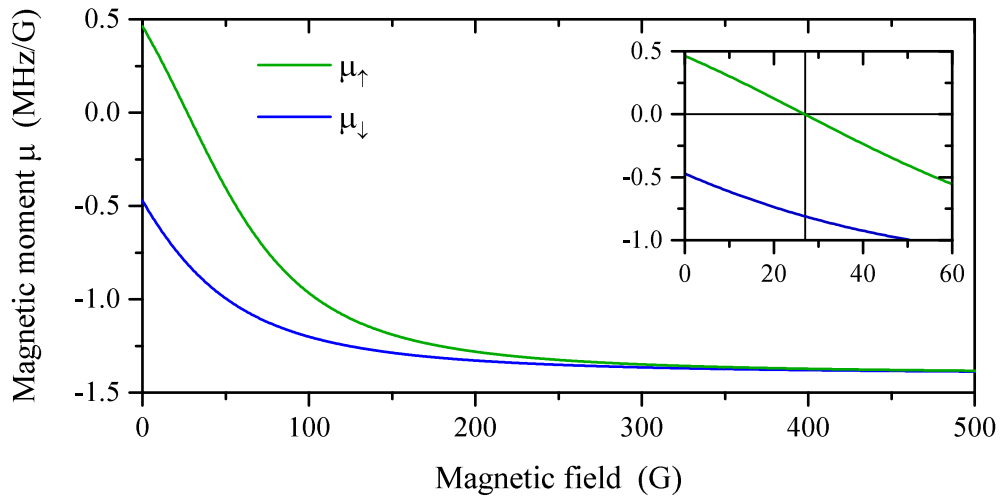


Figure A.2.: Magnetic moment of spin-up atoms μ_{\uparrow} and spin-down atoms μ_{\downarrow} as a function of the magnetic field. For zero magnetic field the magnetic moments of μ_{\uparrow} and μ_{\downarrow} are $\pm\mu_B/3$ respectively, where $\mu_B/h \approx 1.40$ MHz/G is the Bohr magneton. For large magnetic fields both μ_{\uparrow} and μ_{\downarrow} approach $-\mu_B$. (Inset) At about 27 G the magnetic moment of spin-up atoms crosses zero.

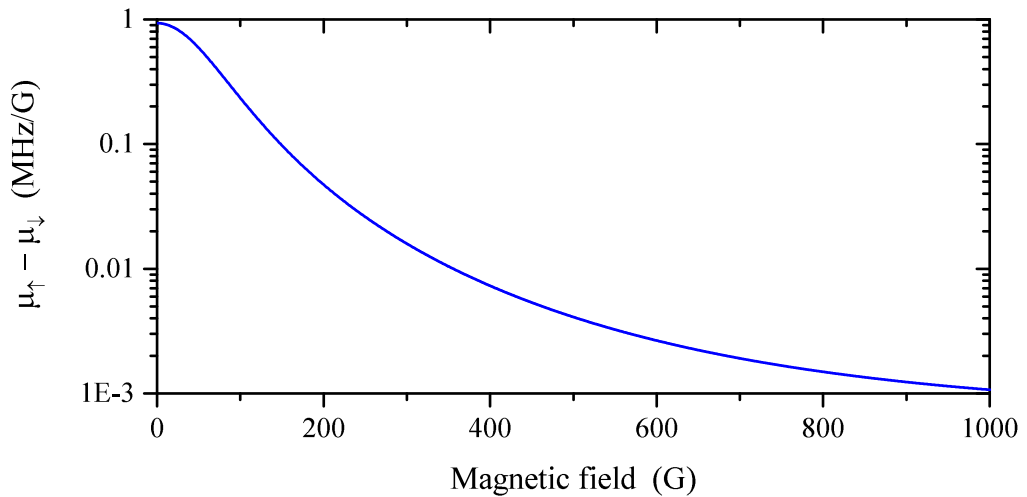


Figure A.3.: Difference between the magnetic moments of spin-up and spin-down atoms as a function of the magnetic field.

A.3. Calibration of the on-site interaction energy

List of all measurements for the calibration of the on-site interactions energy U in the Hubbard model (Sect. 5.2).

B (G)	a_{3D} (a_0)	$-1/g_{1D}$ ($\hbar\omega_{ }a_{ }$)	U ($\hbar\omega_{ }$)	U (J^t)
300	-288.1	6.23 ± 0.16	-0.08 ± 0.01	-1.41 ± 0.25
560	131.8	-12.98 ± 0.33	0.04 ± 0.01	0.67 ± 0.18
600	359.9	-4.62 ± 0.11	0.08 ± 0.01	1.37 ± 0.21
640	699.9	-2.28 ± 0.05	0.18 ± 0.01	3.31 ± 0.11
700	1637.1	-0.86 ± 0.02	0.35 ± 0.01	6.32 ± 0.09
740	2973.9	-0.38 ± 0.01	0.56 ± 0.01	10.26 ± 0.10

Table A.1.: Calibration of the on-site interaction energy in a double-well system. Total light power $P_{\text{tot}} = 1.5$ V. Tunneling matrix element $J^t/h = (67.3 \pm 0.5)$ Hz.

B (G)	a_{3D} (a_0)	$-1/g_{1D}$ ($\hbar\omega_{ }a_{ }$)	U ($\hbar\omega_{ }$)	U (J^t)
300	-288.1	6.87 ± 0.17	-0.03 ± 0.02	-0.20 ± 0.21
620	512.0	-3.55 ± 0.01	0.10 ± 0.04	0.71 ± 0.33
700	1637.1	-0.97 ± 0.02	0.33 ± 0.03	2.31 ± 0.21
740	2973.9	-0.44 ± 0.01	0.49 ± 0.03	3.46 ± 0.22

Table A.2.: Calibration of the on-site interaction energy in a double-well system. Total light power $P_{\text{tot}} = 1$ V. Tunneling matrix element $J^t/h = (142.0 \pm 0.5)$ Hz.

A.4. The optical microtrap

	<i>old</i> microtrap	<i>new</i> microtrap
axial trap frequency	40.7 mm	20.3 mm
field of view (diameter)	200 μm	200 μm
max. diffraction limited NA	0.44	0.6
entrance aperture at max. NA	36 mm	24.4 mm
resolution	1.4 μm	1.08 μm
waist of focus	0.9 μm	0.72 μm

Table A.3.: Design parameters of the *old* and the *new* objective. The *old* (*new*) objective was used to perform the experiments described in Ch. 6 (Ch. 5). The focal waist was calculated for a homogeneous intensity distribution on the entrance aperture. All parameters were taken from Ref [Ser11b].

	<i>old</i> microtrap	<i>new</i> microtrap
measured light power	$(265 \pm 27) \mu\text{W}$	$(390 \pm 39) \mu\text{W}$
axial trap frequency ω_{\parallel}	$2\pi \times (1.234 \pm 0.012) \text{ kHz}$	$\approx 2\pi \times 2.5 \text{ kHz}$
radial trap frequency ω_{\perp}	$2\pi \times (11.88 \pm 0.22) \text{ kHz}$	$\approx 2\pi \times 16.5 \text{ kHz}$
aspect ratio	≈ 10	≈ 7
calculated waist w_0	1.838 μm	1.58 μm
calculated Rayleigh range z_R	9.97 μm	7.37 μm
calculated trap depth V_0	$k_B \times 3.326 \mu\text{K}$	$k_B \times 4.85 \mu\text{K}$
calculated light power	291.5 μW	314.3 μW

Table A.4.: Measured and calculated trap parameters of the microtrap. The *old* (*new*) microtrap was created with the *old* (*new*) objective and used to perform the experiments described in Ch. 6 (Ch. 5). All parameters of the *old* microtrap were taken from the supplemental material of Ref. [Zür12b]. Waist and trap depth of the *new* microtrap have been calculated in a harmonic approximation using the relations $w_0 = \lambda\eta/\sqrt{2\pi}$ and $V_0 = mw_0^2\omega_{\perp}^2/4$. The calculated power in the microtrap was determined using Eq. 4.4.

A.5. Trap parameters

List of the parameters for the tunneling measurement on spin chains presented in Sect. 6.3 and Fig. 6.7. The magnetic field gradient for all measurements is $B' = 18.92$ G/cm (see Sect. 4.4.2). To initiate the tunneling process, we ramp down the intensity of the trapping light within a time t_{ramp} and thereby lower the trap depth parameter p (see Sect. 4.4.2) from its initial value p_{initial} to a final value p_{final} . After a time t_{spill} , during which atoms can tunnel out of the trap, we ramp the power back to its original value to stop the tunneling process.

(2,1) System

#	Magnetic field [G]	p_{initial}	p_{final}	t_{ramp} [ms]	t_{spill} [ms]	$-1/g_{1D} [a_{\parallel} \hbar \omega_{\parallel}]^{-1}$
1	725.96 ± 0.5	0.829 ± 0.025	0.694 ± 0.021	4	200	-0.264 ± 0.013
2	751.01 ± 0.5	0.829 ± 0.025	0.708 ± 0.021	4	200	-0.130 ± 0.008
3	771.05 ± 0.5	0.829 ± 0.025	0.716 ± 0.021	4	200	-0.043 ± 0.004
4	783.08 ± 0.5	0.829 ± 0.025	0.719 ± 0.022	4	200	0.001 ± 0.003
5	786.58 ± 0.5	0.829 ± 0.025	0.711 ± 0.021	4	40	0.013 ± 0.003
6	796.10 ± 0.5	0.829 ± 0.025	0.711 ± 0.021	4	40	0.044 ± 0.002
7	806.12 ± 0.5	0.829 ± 0.025	0.711 ± 0.021	4	40	0.074 ± 0.002
8	851.21 ± 0.5	0.829 ± 0.025	0.729 ± 0.022	4	40	0.186 ± 0.004
9	951.42 ± 0.5	1.371 ± 0.041	0.749 ± 0.022	10	25	0.339 ± 0.010
10	1201.92 ± 0.5	0.871 ± 0.026	0.759 ± 0.023	4	40	0.495 ± 0.015

(3,1) System

#	Magnetic field [G]	p_{initial}	p_{final}	t_{ramp} [ms]	t_{spill} [ms]	$-1/g_{1D} [a_{\parallel} \hbar \omega_{\parallel}]^{-1}$
1	751.01 ± 0.5	0.871 ± 0.026	0.746 ± 0.022	4	200	-0.130 ± 0.007
2	771.05 ± 0.5	0.871 ± 0.026	0.746 ± 0.022	4	80	-0.043 ± 0.004
3	781.57 ± 0.5	0.871 ± 0.026	0.750 ± 0.023	4	40	-0.003 ± 0.003
4	951.42 ± 0.5	1.371 ± 0.041	0.801 ± 0.024	5	25	0.346 ± 0.009
5	1201.92 ± 0.5	1.371 ± 0.041	0.816 ± 0.024	5	25	0.502 ± 0.014

(2,2) System

#	Magnetic field [G]	p_{initial}	p_{final}	t_{ramp} [ms]	t_{spill} [ms]	$-1/g_{1D} [a_{\parallel} \hbar \omega_{\parallel}]^{-1}$
1	751.01 ± 0.5	0.996 ± 0.030	0.689 ± 0.021	5	25	-0.129 ± 0.008
2	771.05 ± 0.5	0.996 ± 0.030	0.694 ± 0.021	5	25	-0.044 ± 0.005
3	776.06 ± 0.5	0.996 ± 0.030	0.700 ± 0.021	5	25	-0.025 ± 0.004
4	781.07 ± 0.5	0.996 ± 0.030	0.696 ± 0.021	5	25	-0.007 ± 0.003
5	951.42 ± 0.5	1.371 ± 0.041	0.734 ± 0.022	5	25	0.337 ± 0.010
6	1201.92 ± 0.5	1.371 ± 0.041	0.741 ± 0.022	5	25	0.491 ± 0.015
7	1402.33 ± 0.5	1.371 ± 0.041	0.741 ± 0.022	5	25	0.539 ± 0.016

A.6. Correction of spin-down tunneling

We correct the probability for spin-down tunneling in spin chains (Sect. 6.3) for three and four-body losses during the tunneling process or during the ramp of the magnetic field. We identify the probability of these loss processes by measuring the probability of finding zero atoms in the trap after the tunneling process. As shown in Fig. A.4, the probability of spin-down tunneling is for all measurements only slightly affected by this correction. A more detailed discussion of this correction can be found in the supplemental material of Ref. [Mur15b].

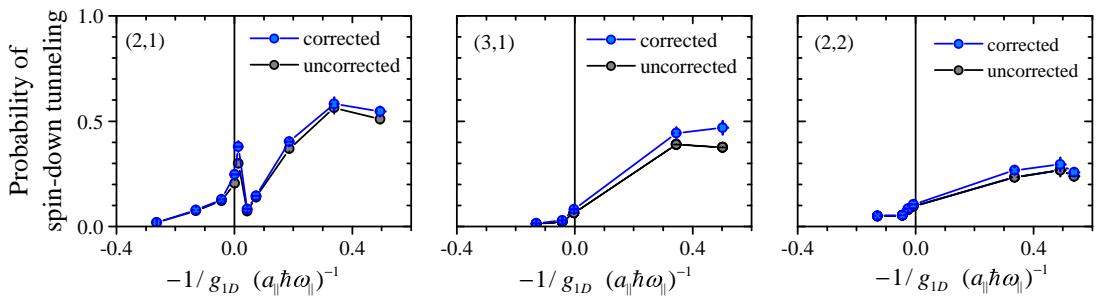


Figure A.4.: Corrected (blue) and uncorrected (black) values of the measurement of spin-down tunneling in Sect. 6.3. The corrected data is shown in Fig. 6.7.

A.7. Correction of occupation-number measurements

Corrected and uncorrected results of the occupation-number measurement in Sect. 6.4. The data was corrected for the finite preparation and detection fidelity of the experiments as explained in Sect. 6.4. The corrected data (blue) is shown as blue data points in Fig. 6.10.

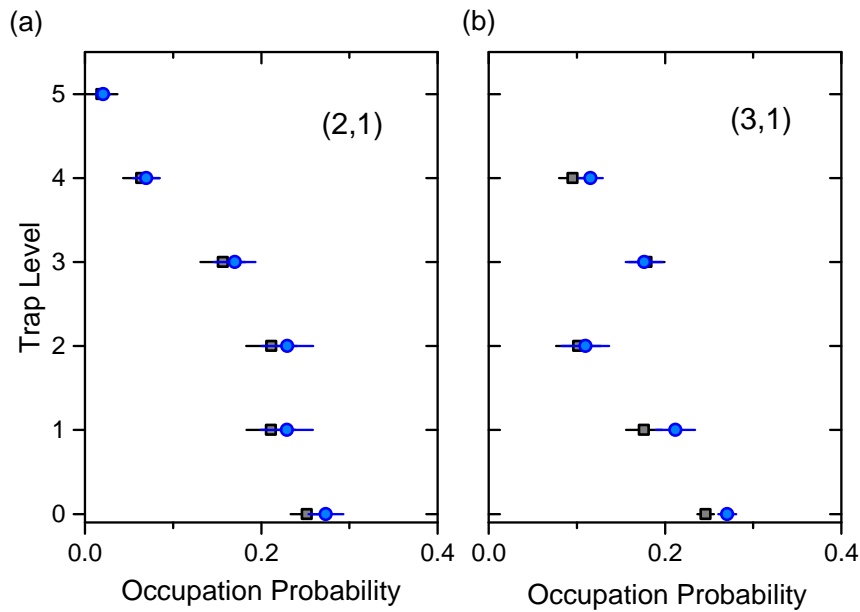


Figure A.5.: Corrected (blue) and uncorrected (black) values of the occupation-number measurement in Sect. 6.4.

Bibliography

- [And87] P. W. Anderson, The resonating valence bond state in La₂CuO₄ and superconductivity, *Science* **235**, 1196 (1987).
- [And95] M. H. Anderson, J. R. Ensher, M. R. Matthews, C. E. Wieman, E. A. Cornell, Observation of Bose-Einstein condensation in a dilute atomic vapor, *Science* **269**, 198 (1995).
- [And02] P. W. Anderson, Superconductivity in high T_c Cuprates: The cause is no longer a mystery, *Phys. Scr. (T102)* (2002).
- [Ash76] N. Ashcroft, N. Mermin, *Solid State Physics* (Saunders College, Philadelphia, 1976).
- [Ast04] G. E. Astrakharchik, D. Blume, S. Giorgini, L. P. Pitaevskii, Interacting Fermions in Highly Elongated Harmonic Traps, *Phys. Rev. Lett.* **93**, 050402 (2004).
- [Ast05] G. E. Astrakharchik, J. Boronat, J. Casulleras, S. Giorgini, Beyond the Tonks-Girardeau Gas: Strongly Correlated Regime in Quasi-One-Dimensional Bose Gases, *Phys. Rev. Lett.* **95**, 190407 (2005).
- [Aue94] A. Auerbach, *Interacting Electrons and Quantum Magnetism* (Springer, New York, 1994).
- [Bak09] W. S. Bakr, J. I. Gillen, A. Peng, S. Fölling, M. Greiner, A quantum gas microscope for detecting single atoms in a Hubbard-regime optical lattice, *Nature* **462**, 74 (2009).
- [Bed86] J. G. Bednorz, K. A. Müller, Possible high T_c superconductivity in the Ba-La-Cu-O system, *Zeitschrift für Physik B* **64**, 189 (1986).
- [Ber03] T. Bergeman, M. G. Moore, M. Olshanii, Atom-Atom Scattering under Cylindrical Harmonic Confinement: Numerical and Analytic Studies of the Confinement Induced Resonance, *Phys. Rev. Lett.* **91**, 163201 (2003).
- [Ber13] A. Bergschneider, *Ultracold few-fermion systems in multiwell potentials*, Masters Thesis, Universität Heidelberg (2013).
- [Blo08a] I. Bloch, Quantum coherence and entanglement with ultracold atoms in optical lattices, *Nature* **453**, 1016 (2008).

- [Blo08b] I. Bloch, J. Dalibard, W. Zwerger, *Many-body physics with ultracold gases*, *Rev. Mod. Phys.* **80**, 885 (2008).
- [Bro13] I. Brouzos, P. Schmelcher, *Two-component few-fermion mixtures in a one-dimensional trap: Numerical versus analytical approach*, *Phys. Rev. A* **87**, 023605 (2013).
- [Bug13] P. Bugnion, G. Conduit, *Ferromagnetic spin correlations in a few-fermion system*, *Phys. Rev. A* **87**, 060502 (2013).
- [Bus98] T. Busch, B.-G. Englert, K. Rzazewski, M. Wilkens, *Two cold atoms in a harmonic trap*, *Found. Phys.* **28**, 549 (1998).
- [Chi10] C. Chin, R. Grimm, P. Julienne, E. Tiesinga, *Feshbach resonances in ultracold gases*, *Rev. Mod. Phys.* **82**, 1225 (2010).
- [Cui14] X. Cui, T.-L. Ho, *Ground-state ferromagnetic transition in strongly repulsive one-dimensional Fermi gases*, *Phys. Rev. A* **89**, 023611 (2014).
- [D'A14] P. D'Amico, M. Rontani, *Three interacting atoms in a one-dimensional trap: a benchmark system for computational approaches*, *J. Phys. B* **47**, 65303 (2014).
- [Dag96] E. Dagotto, T. M. Rice, *Surprises on the Way from One- to Two-Dimensional Quantum Magnets: The Ladder Materials*, *Science* **271**, 618 (1996).
- [Dav95] K. B. Davis, M.-O. Mewes, M. R. Andrews, N. Van Druten, D. Durfee, D. Kurn, W. Ketterle, *Bose-Einstein condensation in a gas of sodium atoms*, *Phys. Rev. Lett.* **75**, 3969 (1995).
- [DeM99] B. DeMarco, D. S. Jin, *Onset of Fermi degeneracy in a trapped atomic gas*, *Science* **285**, 1703 (1999).
- [Deu08] F. Deuretzbacher, K. Fredenhagen, D. Becker, K. Bongs, K. Sengstock, D. Pfannkuche, *Exact Solution of Strongly Interacting Quasi-One-Dimensional Spinor Bose Gases*, *Phys. Rev. Lett.* **100**, 160405 (2008).
- [Deu14] F. Deuretzbacher, D. Becker, J. Bjerlin, S. M. Reimann, L. Santos, *Quantum magnetism without lattices in strongly interacting one-dimensional spinor gases*, *Phys. Rev. A* **90**, 013611 (2014).
- [Dua03] L.-M. Duan, E. Demler, M. Lukin, *Controlling spin exchange interactions of ultracold atoms in optical lattices*, *Phys. Rev. Lett.* **91**, 090402 (2003).
- [Ess10] T. Esslinger, *Fermi-Hubbard Physics with Atoms in an Optical Lattice*, *Annu. Rev. Condens. Matter Phys.* **1**, 129 (2010).

-
- [FA03] S. Franke-Arnold, S. Barnett, G. Huyet, C. Sailliot, Coherence properties of two trapped particles, *Eur. Phys. J. D* **22**, 373 (2003).
- [Fey82] R. P. Feynman, Simulating physics with computers, *Int. J. Theor. Phys.* **21**, 467 (1982).
- [Fli05] T. Fließbach, *Quantenmechanik. Lehrbuch zur Theoretischen Physik III* (Spektrum Akademischer Verlag, 2005).
- [Föl07] S. Fölling, S. Trotzky, P. Cheinet, M. Feld, R. Saers, A. Widera, T. Müller, I. Bloch, Direct observation of second-order atom tunnelling, *Nature* **448**, 1029 (2007).
- [Foo11] C. Foot, M. Shotton, Double well potentials and quantum gates, *Am J Phys* **79**, 762 (2011).
- [Fuk13a] T. Fukuhara, A. Kantian, M. Endres, M. Cheneau, P. Schauß, S. Hild, D. Bellem, U. Schollwöck, T. Giamarchi, C. Gross, et al., Quantum dynamics of a mobile spin impurity, *Nat. Phys.* **9**, 235 (2013).
- [Fuk13b] T. Fukuhara, P. Schauß, M. Endres, S. Hild, M. Cheneau, I. Bloch, C. Gross, Microscopic observation of magnon bound states and their dynamics, *Nature* **502**, 76 (2013).
- [Gha12] S. E. Gharashi, K. M. Daily, D. Blume, Three s-wave-interacting fermions under anisotropic harmonic confinement: Dimensional crossover of energetics and virial coefficients, *Phys. Rev. A* **86**, 042702 (2012).
- [Gha13] S. E. Gharashi, D. Blume, Correlations of the upper branch of 1D harmonically trapped two-component Fermi gases, *Phys. Rev. Lett.* **111**, 045302 (2013).
- [Gha14] S. E. Gharashi, X. Y. Yin, D. Blume, Molecular branch of a small highly elongated Fermi gas with an impurity: Full three-dimensional versus effective one-dimensional description, *Phys. Rev. A* **89**, 023603 (2014).
- [Gha15] S. E. Gharashi, X. Y. Yin, Y. Yan, D. Blume, One-dimensional Fermi gas with a single impurity in a harmonic trap: Perturbative description of the upper branch, *Phys. Rev. A* **91**, 013620 (2015).
- [Gia04] T. Giamarchi, *Quantum Physics in One Dimension* (Oxford University Press, New York, 2004).
- [Gir60] M. Girardeau, Relationship between systems of impenetrable bosons and fermions in one dimension, *J. Math. Phys.* **1**, 516 (1960).

- [Gir07] M. D. Girardeau, A. Minguzzi, Soluble Models of Strongly Interacting Ultracold Gas Mixtures in Tight Waveguides, *Phys. Rev. Lett.* **99**, 230402 (2007).
- [Gir10] M. D. Girardeau, Two super-Tonks-Girardeau states of a trapped one-dimensional spinor Fermi gas, *Phys. Rev. A* **82**, 011607 (2010).
- [Gre02] M. Greiner, O. Mandel, T. Esslinger, T. W. Hänsch, I. Bloch, Quantum phase transition from a superfluid to a Mott insulator in a gas of ultracold atoms, *Nature* **415**, 44 (2002).
- [Gre13] D. Greif, T. Uehlinger, G. Jotzu, L. Tarruell, T. Esslinger, Short-range quantum magnetism of ultracold fermions in an optical lattice, *Science* **340**, 1307 (2013).
- [Gri00] R. Grimm, M. Weidemüller, Y. B. Ovchinnikov, Optical Dipole Traps for Neutral Atoms, *Adv. At. Mol. Opt. Phys.* **42**, 95 (2000).
- [Gri15] T. Grining, M. Tomza, M. Lesiuk, M. Przybytek, R. Moszynski, M. Lewenstein, P. Massignan, Crossover between few and many fermions in a harmonic trap, arXiv:1507.03174 (2015).
- [Gua09] L. Guan, S. Chen, Y. Wang, Z.-Q. Ma, Exact Solution for Infinitely Strongly Interacting Fermi Gases in Tight Waveguides, *Phys. Rev. Lett.* **102**, 160402 (2009).
- [Gua10] L. Guan, S. Chen, Super-Tonks-Girardeau Gas of Spin-1/2 Interacting Fermions, *Phys. Rev. Lett.* **105**, 175301 (2010).
- [Hal09] E. Haller, M. Gustavsson, M. J. Mark, J. G. Danzl, R. Hart, G. Pupillo, H.-C. Nägerl, Realization of an Excited, Strongly Correlated Quantum Gas Phase, *Science* **325**, 1224 (2009).
- [Har14] N. L. Harshman, Spectroscopy for a few atoms harmonically trapped in one dimension, *Phys. Rev. A* **89**, 033633 (2014).
- [Har15] R. A. Hart, P. M. Duarte, T.-L. Yang, X. Liu, T. Paiva, E. Khatami, R. T. Scalettar, N. Trivedi, D. A. Huse, R. G. Hulet, Observation of antiferromagnetic correlations in the Hubbard model with ultracold atoms, *Nature* **519**, 211 (2015).
- [Hei27] W. Heitler, F. London, Wechselwirkung neutraler Atome und homöopolare Bindung nach der Quantenmechanik, *Zeitschrift für Physik* **44**, 455 (1927).
- [Hei28] W. Heisenberg, Zur Theorie des Ferromagnetismus, *Zeitschrift für Physik* **49**, 619 (1928).

-
- [Ho08] T.-L. Ho, *The intrinsic difficulties of constructing strongly correlated states of lattice quantum gases by connecting up pre-engineered isolated atomic clusters*, arXiv:0808.2677 (2008).
- [Ho09] A. Ho, M. Cazalilla, T. Giamarchi, *Quantum simulation of the Hubbard model: The attractive route*, Phys. Rev. A **79**, 033620 (2009).
- [Hol00] M. J. Holland, B. DeMarco, D. S. Jin, *Evaporative cooling of a two-component degenerate Fermi gas*, Phys. Rev. A **61**, 053610 (2000).
- [Hu94] Z. Hu, H. Kimble, *Observation of a single atom in a magneto-optical trap*, Opt. Lett. **19**, 1888 (1994).
- [Hub63] J. Hubbard, *Electron correlations in narrow energy bands*, in Proc. R. Soc. A, Vol. 276, 238, The Royal Society (1963).
- [Hum13] D. B. Hume, I. Stroescu, M. Joos, W. Muessel, H. Strobel, M. K. Oberthaler, *Accurate Atom Counting in Mesoscopic Ensembles*, Phys. Rev. Lett. **111**, 253001 (2013).
- [Idz06] Z. Idziaszek, T. Calarco, *Analytical solutions for the dynamics of two trapped interacting ultracold atoms*, Phys. Rev. A **74**, 022712 (2006).
- [Isi25] E. Ising, *Beitrag zur Theorie des Ferromagnetismus*, Zeitschrift für Physik **31**, 253 (1925).
- [Jak98] D. Jaksch, C. Bruder, J. I. Cirac, C. W. Gardiner, P. Zoller, *Cold Bosonic Atoms in Optical Lattices*, Phys. Rev. Lett. **81**, 3108 (1998).
- [Jak05] D. Jaksch, P. Zoller, *The cold atom Hubbard toolbox*, Ann. Phys. **315**, 52 (2005).
- [Joc03] S. Jochim, M. Bartenstein, A. Altmeyer, G. Hendl, C. Chin, J. H. Denschlag, R. Grimm, *Pure Gas of Optically Trapped Molecules Created from Fermionic Atoms*, Phys. Rev. Lett. **91**, 240402 (2003).
- [Joc04] S. Jochim, *Bose-Einstein Condensation of Molecules*, Dissertation, Leopold-Franzens-Universität Innsbruck (2004).
- [Jör08] R. Jördens, N. Strohmaier, K. Günter, H. Moritz, T. Esslinger, *A Mott insulator of fermionic atoms in an optical lattice*, Nature **455**, 204 (2008).
- [Kau14] A. Kaufman, B. Lester, C. Reynolds, M. Wall, M. Foss-Feig, K. Hazzard, A. Rey, C. Regal, *Two-particle quantum interference in tunnel-coupled optical tweezers*, Science **345**, 306 (2014).
- [Ket99] W. Ketterle, D. Durfee, D. Stamper-Kurn, *Making, probing and understanding Bose-Einstein condensates*, arXiv:9904034 (1999).

- [Ket08] W. Ketterle, M. W. Zwierlein, *Making, probing and understanding ultracold Fermi gases*, arXiv:0801.2500 (2008).
- [Kin04] T. Kinoshita, T. Wenger, D. S. Weiss, *Observation of a one-dimensional Tonks-Girardeau gas*, *Science* **305**, 1125 (2004).
- [Kin05] T. Kinoshita, T. Wenger, D. S. Weiss, *Local pair correlations in one-dimensional Bose gases*, *Phys. Rev. Lett.* **95**, 190406 (2005).
- [Kli12] V. M. Klinkhamer, *An apparatus for few-fermion systems in multiple well potentials*, Masters Thesis, Universität Heidelberg (2012).
- [Les15] B. J. Lester, N. Luick, A. M. Kaufman, C. M. Reynolds, C. A. Regal, *Rapid Production of Uniformly Filled Arrays of Neutral Atoms*, *Phys. Rev. Lett.* **115**, 073003 (2015).
- [Lev15] J. Levinsen, P. Massignan, G. M. Bruun, M. M. Parish, *Strong-coupling ansatz for the one-dimensional Fermi gas in a harmonic potential*, *Sci. Adv.* **1** (2015).
- [Lie62] E. Lieb, D. Mattis, *Ordering energy levels of interacting spin systems*, *J. Math. Phys.* **3**, 749 (1962).
- [Lie89] E. H. Lieb, *Two theorems on the Hubbard model*, *Phys. Rev. Lett.* **62**, 1201 (1989).
- [Lin14] E. Lindgren, J. Rotureau, C. Forssén, A. Volosniev, N. T. Zinner, *Fermionization of two-component few-fermion systems in a one-dimensional harmonic trap*, *New J. Phys.* **16**, 063003 (2014).
- [Lom08] T. Lompe, *An apparatus for the production of molecular Bose-Einstein condensates*, Diploma thesis, Universität Heidelberg (2008).
- [Lom11] T. Lompe, *Efimov Physics in a three-component Fermi gas*, Dissertation, Universität Heidelberg (2011).
- [Lub11] M. Lubasch, V. Murg, U. Schneider, J. I. Cirac, M.-C. Bañuls, *Adiabatic Preparation of a Heisenberg Antiferromagnet Using an Optical Superlattice*, *Phys. Rev. Lett.* **107**, 165301 (2011).
- [Mar15] O. Marchukov, E. Eriksen, J. Midtgaard, A. Kalaei, D. Fedorov, A. Jensen, N. Zinner, *Computation of local exchange coefficients in strongly interacting one-dimensional few-body systems: local density approximation and exact results*, arXiv:1508.07164 (2015).
- [Mat01] M. Matsumoto, C. Yasuda, S. Todo, H. Takayama, *Ground-state phase diagram of quantum Heisenberg antiferromagnets on the anisotropic dimerized square lattice*, *Phys. Rev. B* **65**, 014407 (2001).

-
- [Mat04a] K. Matveev, Conductance of a quantum wire in the Wigner-crystal regime, *Phys. Rev. Lett.* **92**, 106801 (2004).
- [Mat04b] K. A. Matveev, Conductance of a quantum wire at low electron density, *Phys. Rev. B* **70**, 245319 (2004).
- [Mat08] K. Matveev, A. Furusaki, Spectral Functions of Strongly Interacting Isospin-1/2 Bosons in One Dimension, *Phys. Rev. Lett.* **101**, 170403 (2008).
- [McK11] D. McKay, B. DeMarco, Cooling in strongly correlated optical lattices: prospects and challenges, *Rep. Prog. Phys.* **74**, 054401 (2011).
- [Mer66] N. D. Mermin, H. Wagner, Absence of Ferromagnetism or Antiferromagnetism in One- or Two-Dimensional Isotropic Heisenberg Models, *Phys. Rev. Lett.* **17**, 1133 (1966).
- [Mes15] M. Messer, R. Desbuquois, T. Uehlinger, G. Jotzu, S. Huber, D. Greif, T. Esslinger, Exploring competing density order in the ionic Hubbard model with ultracold fermions, arXiv:1503.05549 (2015).
- [Met99] H. J. Metcalf, P. Van der Straten, *Laser Cooling and Trapping* (Springer, New York, 1999).
- [Mor05a] C. Mora, A. Komnik, R. Egger, A. O. Gogolin, Four-Body Problem and BEC-BCS Crossover in a Quasi-One-Dimensional Cold Fermion Gas, *Phys. Rev. Lett.* **95**, 080403 (2005).
- [Mor05b] H. Moritz, T. Stöferle, K. Günter, M. Köhl, T. Esslinger, Confinement Induced Molecules in a 1D Fermi Gas, *Phys. Rev. Lett.* **94**, 210401 (2005).
- [Mur15a] S. Murmann, A. Bergschneider, V. M. Klinkhamer, G. Zürn, T. Lompe, S. Jochim, Two Fermions in a double well: Exploring a fundamental building block of the Hubbard model, *Phys. Rev. Lett.* **114**, 080402 (2015).
- [Mur15b] S. Murmann, F. Deuretzbacher, G. Zürn, J. Bjerlin, S. M. Reimann, L. Santos, T. Lompe, S. Jochim, Antiferromagnetic Heisenberg spin chain of few cold atoms in a one-dimensional trap, arXiv:1507.01117 (2015).
- [Nas12] S. Nascimbène, Y.-A. Chen, M. Atala, M. Aidelsburger, S. Trotzky, B. Paredes, I. Bloch, Experimental realization of plaquette resonating valence-bond states with ultracold atoms in optical superlattices, *Phys. Rev. Lett.* **108**, 205301 (2012).
- [Nei13] M. Neidig, A realization of a two-dimensional Fermi gas in a standing wave trap, Masters Thesis, Universität Heidelberg (2013).

- [Nor11] M. R. Norman, *The challenge of unconventional superconductivity*, *Science* **332**, 196 (2011).
- [Ols98] M. Olshanii, *Atomic scattering in the presence of an external confinement and a gas of impenetrable bosons*, *Phys. Rev. Lett.* **81**, 938 (1998).
- [Ott10] T. Ottenstein, *Few-body physics in ultracold Fermi gases*, Dissertation, Universität Heidelberg (2010).
- [Par10] J. B. Parkinson, D. J. Farnell, *An Introduction to Quantum Spin Systems* (Springer, 2010).
- [Pet00] D. Petrov, G. Shlyapnikov, J. Walraven, *Regimes of quantum degeneracy in trapped 1D gases*, *Phys. Rev. Lett.* **85**, 3745 (2000).
- [Sac08] S. Sachdev, *Quantum magnetism and criticality*, *Nat. Phys.* **4**, 173 (2008).
- [Sak85] J. J. Sakurai, *Modern Quantum Mechanics* (Benjamin/Cummings, Menlo Park CA, 1985).
- [Sal13] S. Sala, G. Zürn, T. Lompe, A. N. Wenz, S. Murmann, F. Serwane, S. Jochim, A. Saenz, *Coherent Molecule Formation in Anharmonic Potentials Near Confinement-Induced Resonances*, *Phys. Rev. Lett.* **110**, 203202 (2013).
- [Sch08] U. Schneider, L. Hackermüller, S. Will, T. Best, I. Bloch, T. Costi, R. Helmes, D. Rasch, A. Rosch, *Metallic and insulating phases of repulsively interacting fermions in a 3D optical lattice*, *Science* **322**, 1520 (2008).
- [Ser07] F. Serwane, *The setup of a Magneto Optical Trap for the preparation of a mesoscopic degenerate Fermi gas*, Diploma thesis, Universität Heidelberg (2007).
- [Ser11a] F. Serwane, *Deterministic preparation of a tunable few-fermion system*, Dissertation, Universität Heidelberg (2011).
- [Ser11b] F. Serwane, G. Zürn, T. Lompe, T. Ottenstein, A. Wenz, S. Jochim, *Deterministic preparation of a tunable few-fermion system*, *Science* **332**, 336 (2011).
- [Sim11] J. Simon, W. S. Bakr, R. Ma, M. E. Tai, P. M. Preiss, M. Greiner, *Quantum simulation of antiferromagnetic spin chains in an optical lattice*, *Nature* **472**, 307 (2011).
- [SK98] D. M. Stamper-Kurn, H.-J. Miesner, A. P. Chikkatur, S. Inouye, J. Stenger, W. Ketterle, *Reversible Formation of a Bose-Einstein Condensate*, *Phys. Rev. Lett.* **81**, 2194 (1998).

-
- [Sow13] T. Sowiński, T. Grass, O. Dutta, M. Lewenstein, *Few interacting fermions in a one-dimensional harmonic trap*, Phys. Rev. A **88**, 033607 (2013).
- [Spi07] I. Spielman, W. Phillips, J. Porto, *Mott-insulator transition in a two-dimensional atomic Bose gas*, Phys. Rev. Lett. **98**, 080404 (2007).
- [Stö04] T. Stöferle, H. Moritz, C. Schori, M. Köhl, T. Esslinger, *Transition from a strongly interacting 1D superfluid to a Mott insulator*, Phys. Rev. Lett. **92**, 130403 (2004).
- [Tre06] S. Trebst, U. Schollwöck, M. Troyer, P. Zoller, *d-Wave resonating valence bond states of fermionic atoms in optical lattices*, Phys. Rev. Lett. **96**, 250402 (2006).
- [Tro08] S. Trotzky, P. Cheinet, S. Fölling, M. Feld, U. Schnorrberger, A. M. Rey, A. Polkovnikov, E. Demler, M. Lukin, I. Bloch, *Time-resolved observation and control of superexchange interactions with ultracold atoms in optical lattices*, Science **319**, 295 (2008).
- [Tro10] S. Trotzky, Y.-A. Chen, U. Schnorrberger, P. Cheinet, I. Bloch, *Controlling and detecting spin correlations of ultracold atoms in optical lattices*, Phys. Rev. Lett. **105**, 265303 (2010).
- [Vol14] A. Volosniev, D. V. Fedorov, A. S. Jensen, M. Valiente, N. T. Zinner, *Strongly interacting confined quantum systems in one dimension*, Nat. Commun. **5** (2014).
- [Wen13a] A. Wenz, *From Few to Many: Ultracold Atoms in Reduced Dimensions*, Dissertation, Universität Heidelberg (2013).
- [Wen13b] A. Wenz, G. Zürn, S. Murmann, I. Brouzos, T. Lompe, S. Jochim, *From few to many: observing the formation of a Fermi sea one atom at a time*, Science **342**, 457 (2013).
- [Win06] K. Winkler, G. Thalhammer, F. Lang, R. Grimm, J. H. Denschlag, A. Daley, A. Kantian, H. Büchler, P. Zoller, *Repulsively bound atom pairs in an optical lattice*, Nature **441**, 853 (2006).
- [Zim11] B. Zimmermann, T. Mueller, J. Meineke, T. Esslinger, H. Moritz, *High-resolution imaging of ultracold fermions in microscopically tailored optical potentials*, New J. Phys. **13**, 043007 (2011).
- [Zür12a] G. Zürn, *Few-fermion systems in one dimension*, Dissertation, Universität Heidelberg (2012).

- [Zür12b] G. Zürn, F. Serwane, T. Lompe, A. N. Wenz, M. G. Ries, J. E. Bohn, S. Jochim, *Fermionization of Two Distinguishable Fermions*, *Phys. Rev. Lett.* **108**, 075303 (2012).
- [Zür13a] G. Zürn, T. Lompe, A. N. Wenz, S. Jochim, P. S. Julienne, J. M. Hutson, *Precise Characterization of ^6Li Feshbach Resonances Using Trap-Sideband-Resolved RF Spectroscopy of Weakly Bound Molecules*, *Phys. Rev. Lett.* **110**, 135301 (2013).
- [Zür13b] G. Zürn, A. Wenz, S. Murmann, A. Bergschneider, T. Lompe, S. Jochim, *Pairing in few-fermion systems with attractive interactions*, *Phys. Rev. Lett.* **111**, 175302 (2013).

Danksagung

Hiermit möchte ich allen danken, die mir in den letzten Jahren geholfen und damit zum Gelingen dieser Arbeit beigetragen haben. Ohne Euch wäre vieles von dem, was in dieser Arbeit steht, nicht möglich gewesen.

Insbesondere danke ich:

- Selim, dafür dass Du mich in den letzten drei Jahren mit unendlich viel Enthusiasmus und Freundlichkeit betreut hast. Immer wieder hast Du mich mit Deiner Neugierde dazu gebracht Dinge zu hinterfragen und sie dadurch wirklich zu verstehen.
- Allen am alten Experiment: Andrea, Vincent, Jan-Hendrik, Thomas und Gerhard. Vielen Dank für die vielen tollen Stunden innerhalb und außerhalb des Labors. Mit Euch kam bei aller Arbeit der Spaß nie zu kurz und auch wenn mal wieder etwas kaputt gegangen ist, haben wir es immer gemeinsam repariert. Danke auch an Friedhelm Serwane und Timo Ottenstein, die vor meiner Zeit Doktoranden am Experiment waren und es in einem tollen Zustand übergeben haben.
- Allen am neuen Experiment: Puneet, Martin, Andre, Mathias, Luca, Dhruv, Sebastian und allen anderen. Danke für wichtige Diskussionen, das Korrekturlesen der Arbeit, spannende Kicker-Schlachten und schöne gemeinsame Abende.

Danke Euch allen für Eure Hilfe und Freundschaft.

- Markus Oberthaler für das Lesen und Begutachten dieser Arbeit und für die Betreuung während meiner Diplomarbeit, die mein Interesse an den Quantengasen geweckt hat.
- Tilman Enss und Peter Bachert für die Bereitschaft, Teil meiner Prüfungskommission zu sein.

-
- Frank Deuretzbacher, Luis Santos, Stephanie Reimann, Johannes Bjerlin, Ioannis Brouzos, Simon Sala, Dörte Blume, Pietro Massignan, Jesper Levinsen und Meera Parish für viele interessante Diskussionen über die Physik von wenigen Atomen. Insbesondere Frank, dafür dass Du uns mit so viel Leidenschaft die Spinketten-Theorie erklärt hast.
 - Allen Mitarbeitern des PI, des MPI und der HGSFP – besonders Claudia Krämer – für die freundliche Hilfe bei allen größeren und kleineren Problemen.
 - Den Werkstätten am MPI und PI für das Planen und Erstellen von elektronischen und mechanischen Bauteilen und für das großzügige Verleihen von technischem Equipment. Insbesondere auch vielen Dank für die Hilfe beim Umzug des Experiments.
 - Meinen Freunden und meiner Familie. Besonders meinen Eltern, Irene und Werner, und meinen Brüdern, Lukas und Martin, die mir alles mit auf den Weg gegeben haben und immer für mich da sind.
 - Simona, für Deine Unterstützung und Deine Liebe. Und dafür, dass Du morgens mit mir aufwachst, abends mit mir einschläfst und mich dazwischen jeden Tag zum Lachen bringst.